IN-SITU SPECTROELECTROCHEMICAL SURFACE STUDIES OF FUNDAMENTAL FUEL CELL CATALYSIS

BY

ROBERT BRIEN KUTZ

DISSERTATION

Submitted in partial fulfillment of the requirements
for the degree of Doctor of Philosophy in Chemistry
in the Graduate College of the
University of Illinois at Urbana-Champaign, 2012

Urbana, Illinois

Doctoral Committee:

Professor Andrzej Wieckowski, Chair
Professor Dana D. Dlott
Professor Martin Gruebele
Professor Paul Kenis

ABSTRACT

Electrochemical analysis and broadband sum frequency generation (BB-SFG) vibrational spectroscopy have been applied to a variety of fuel cell relevant systems. Primarily, ethanol oxidation was studied due to the potential of ethanol as an easily-transported and manufactured fuel with a higher molecular energy density of 12 electrons per molecule. Additionally, the reaction intermediate carbon monoxide was studied in-depth to better understand its spectroscopic behavior, and investigations were made into the characterization of a cobalt octaethylporphyrin complex by SFG spectroscopy.

Ethanol electrooxidation as studied in acidic electrolytes yields certain key insights. The results include the first observation of adsorbed acetate and co-adsorbed sulfuric acid anions with SFG spectroscopy. Surface-adsorbed intermediates such as CO on Pt atop sites and acetate are observed in both H_2SO_4 and $HClO_4$, but only H_2SO_4 shows evidence of adsorbed (bi)sulfate species or adsorption of CO to bridge sites. Studies performed with isotopically-labeled ethanol ($^{12}CH_3{}^{13}CH_2OH$) demonstrate evidence of a methyl fragment ($-^{12}CH_x$) that is difficult to oxidize further to CO.

Studied in alkaline electrolytes, the differences in the ethanol oxidation mechanism become more fully apparent. C–C bond cleavage and CO formation occur as early as 0.05 V vs. RHE. Furthrmore, CO is oxidized at ~0.45 V, which is 0.2 V lower than in acidic media. Isotopically-labeled ethanol ($^{12}CH_3{}^{13}CH_2OH$) is once again used to study the formation of CO and other single-carbon intermediates. Surface-adsorbed ^{12}CO and ^{13}CO are observed in entirely different applied potential domains. ^{13}CO molecules

formed from the alpha carbon on the ethanol molecule, show the behavior expected from studies of CO-saturated alkaline media. ^{12}CO is formed from the beta carbon of the ethanol molecule and is observed at unusually high potentials. The strongly adsorbed – CH_x intermediate that is formed from the beta carbon after carbon-carbon bond cleavage is not oxidized from the Pt surface until the electrode potential is swept past 0.65 V.

Further studies were also applied to methanol, acetaldehyde, and formic acid. The former two molecules were studied in an attempt to better understand the ethanol oxidation mechanism in alkaline media. Methanol oxidation in alkaline electrolytes produced a sustained CO signal and these results required clarification with the use of fast-scan cyclic voltammetry. Acetaldehyde oxidation in alkaline electrolytes shows unique CO behavior that is not observed in ethanol oxidation in the same electrolyte, adding further evidence that acetaldehyde is not a long-lived intermediate in ethanol oxidation in NaOH. Formic acid studies show the adsorbed formate radical appear on Pt(111) surfaces as soon as the CO molecule is oxidatively removed.

Studies of spectroscopic behavior of CO were conducted to better construct an experimental framework for modeling CO adsorption. Here it is shown that both pH and CO coverage have different effects on the frequency of the CO vibrational band.

Characterization of the Co-OEP macrocycle was conducted using Raman and BB-SFG spectroscopy. BB-SFG is shown to be a useful tool for in-situ observation of key molecular vibrations.

ACKNOWLEDGEMENTS

Thank you, Dr. Andrzej Wieckowski, for the opportunity to work in your laboratory and for your unflagging assistance of my graduate studies. It is with your guidance and support that I have been able to develop and grow as scientist.

Thank you, Dr. Dana Dlott, for your patient and profitable collaboration and for your sense of humor. I owe much of my research to the unique capabilities of the BB-SFG instrument that you have provided and maintained.

I also thank the other members of my graduate committee – Dr Martin Gruebele and Dr. Paul Kenis for their time and service. And I thank Dr. James Lisy, who served previously on my graduate committee before moving to the National Science Foundation in Washington, D.C.

I sincerely thank the following colleagues. Dr. Rachel Behrens has been a mentor and friend since I first joined the Wieckowski lab, and has offered advice even for the writing of this dissertation. She also bought me the best coffee mug I have ever had, and I promptly broke it. Dr. Björn Braunschweig taught me how to use the SFG instrument independently, provided enormous assistance for my first publication, and brought me beer all the way from Germany. Dr. Prabuddha Mukherjee is a friend and collaborator with whom I have consistently discussed our research and with whom I have often consulted when the SFG instrument stopped working properly. Dr. Niancai Cheng and Jose Martinez were welcome company in the lab and assisted with the Co-OEP preparation. Drs. Hung Duong, Matt Rigsby, and Daniela Marques dos Anjos provided a

wonderful collegiate atmosphere and strong motivation during their time here. Dr Stephanie Goubert-Renaudin has been a good friend and confidante, although she would probably prefer a word with a more strictly English etymology.

And there are many other scientists and friends I need to thank as well – Dr. Alexei Lagutchev, Dr. Xiuling Zhu, Chris Corcoran, Hadi Tavassol, Benjamin Lew, Theodore Papadopoulos. Arbelah – thank you for your attendance.

Thank you to Allison McGillivray and Samuel Yergler, whose graceful and generous love and companionship has been a pillar to which I have often held fast. And thank you to Michael Rosana, whose loyal friendship and odd notions about microwaves have provided brightness to even the gloomiest of days.

And yes, thank you Jenna. Too much, and not enough.

Thank you, Meghan; Thank you Mom; Thank you Dad. You have always been there for me, even when I have not.

Finally, thank you to the cats, dogs, and fish that I have known. You have understood little and accepted everything.

TABLE OF CONTENTS

CHAPTER 1

INTRODUCTION

1.1 Fuel Cells

Although the fundamental scientific principles behind fuel cell technology were first demonstrated more than 170 years ago by Sir William Grove,[1] the advancement of fuel cell technology since then has been severely limited by an incomplete understanding of the fundamental catalytic processes. Modern fuel cells have evolved considerably, from Francis Thomas Bacon's development of a 5 kW hydrogen fuel cell in 1959[2] to the development of the first hydrogen fuel cell vehicle in 1991, but their promise as a clean and efficient alternative energy source has yet to be fully realized.[3-7]

The unique promise of fuel cells lies in their very high energy efficiency as well as their potential environmental, political, and economic impact.[8-11] In the simplest formulation, a fuel cell is composed of an anode, electrolyte, cathode, and fuel. Two complementary reactions take place during the operation of the fuel cell. On the anode, oxidation of the fuel takes place, producing electrons, protons, and potentially some side-products. These protons from the anode-side reaction then travel to the cathode, where they are reduced in a reaction with oxygen to produce water. Electrons generated at the anode travel to the cathode via an external circuit, and this flow of electricity can be used to power attached devices.

The most immediate advantage of such a construction is that it generates power while bypassing the Carnot cycle.[8] This makes fuel cell technology potentially far more

thermodynamically efficient than even the most well-designed heat engines powered by, for example, coal or oil. Indeed, the available fuels of interest to fuel cell development are also far cleaner, cheaper, and often more domestically available than oil.[10, 12-21] Such fuels include hydrogen, formic acid, and small alcohols. The environmental advantage of a hydrogen fuel cell is enormous, as the only byproduct is water,[9] but even carbon-based fuels would ideally oxidize to form only carbon dioxide in a fuel cell, and in such a way as to render the carbon dioxide more easily controlled and managed. Finally, the political and economic implications of reducing national dependence on the importation of foreign oil are so plainly dramatic as to practically demand the implementation of fuel cell technology. However, such implementation is troubled.

Perhaps the greatest problem facing modern fuel cells lies in providing a fuel oxidation scheme that is inexpensive, efficient, and viable in the long term for a wide variety of applications.[7-9] Hydrogen fuel cells might seem the most attractive general choice, but the creation of a broad hydrogen economy is probably impractical.[9, 22] Inexpensive generation of molecular hydrogen can produce a number of greenhouse gases,[13] and molecular hydrogen's volatile gaseous nature makes storage and transportation more difficult than for liquid fuels.[9] Thus a liquid fuel such as ethanol, which is relatively abundant, cheap, and easily produced, seems to be an enticing alternative.[4, 20, 23-25]

However, the catalytic oxidation of liquid fuels at low temperatures is beset by difficulties, the foremost of which is the generation of catalyst-poisoning intermediate

species that impede complete oxidation of the fuel.[26-31] Ethanol is potentially a very energy-dense fuel, producing 12 electrons and 2 molecules of carbon dioxide per completely-oxidized ethanol molecule. However, incomplete oxidation prevails even on the most active catalysts such as platinum, producing carbon monoxide that poisons the catalyst surface at low operating potentials. Even worse, the likely formation of acetic acid in acidic electrolytes represents the generation only four electrons per ethanol molecule, and acetic acid cannot be further oxidized at fuel cell relevant potentials. This is represented in Scheme 1.1. Clearly, if ethanol and other liquid fuels are to be practically implemented in low-temperature fuel cells, then the necessary conditions must be met to optimize their oxidation.

While improving the complete oxidation of liquid fuels via catalysis may seem obvious, the complex mechanisms of that catalysis are anything but. A full understanding of the processes relevant to fuel cell catalysis requires fundamental molecular-level studies of how catalyst composition, catalyst morphology, electrolyte composition, pH, and applied electric potential affect the mechanisms of fuel oxidation and the adsorption of chemical species. Without this complete molecular-level understanding, rational catalyst design cannot intelligently progress.

1.2 Electrochemical Methods

Fortunately, electrochemical science provides an indispensable foundation from which to construct the study of fuel cell catalyst interfaces. The first and perhaps simplest model of a metal surface in electrolytic media was provided by Hermann von

Helmholtz.[32] Here, the electrical double layer was treated as a simple capacitor in which a single layer of ions adsorb to a charged metal surface. This model was later expanded upon by the work of Louis Georges Gouy and David Chapman, who introduced a diffuse model of the electrical double layer.[33, 34] This modification helped with modeling the weakening of potential-driven interactions between ions and the charged metal surface itself. Stern then further improved upon this work by essentially combining the Helmholtz and Gouy-Chapman models to provide for an internal layer of ionic interactions (called the Stern layer) and, past that, a diffuse region.[35] This model (called the Gouy-Chapman-Stern model) is still arguably the most commonly used, but it is still a rudimentary model that is limited in several ways, including its use of point charges and inability account for non-Coulombic interactions. A depiction of this model is presented in Figure 1.1.

Ionic interactions with the metal surface are indeed relevant and will be discussed in greater detail in Chapter 2. However, they do not go very far in helping us to understand how organic molecules participate in phenomena such as adsorption and desorption or undergo oxidation/reduction reactions on the metal surface. Studies of the adsorption of molecular species such as CO onto a metal surface have shown significant dependence of this adsorption on primarily electronic and structural effects.[36-39] As mentioned previously, CO is a common intermediate of organic fuel electrooxidation and frequently acts as a catalyst-poisoning adsorbate at lower electric potentials. Electronically, it is now thought that adsorption of CO onto a metal surface occurs via the donation of electrons from the CO 5σ orbital to unoccupied metal orbitals

along with concomitant back-donation of electrons from metal d orbitals to unoccupied 2π orbitals of the CO molecule.[40, 41]

However, if the production of CO can be considered a logically necessary step toward the formation of CO_2, then we need not be as concerned with the stopping adsorption of CO as with hastening the molecule's desorption. In removing CO from the metal surface, electronic interactions between the metal and molecule are still worth considering, but several other factors, including surface morphology and the ambient electronic and molecular environment, come significantly into play. Ultimately, desorption of the poisoning CO intermediate can best be achieved by tuning conditions to promote oxidation of CO to CO_2 at lower applied potentials, and doing so requires a more complete model of adsorbate reactivity. The following should provide an outline of some of the basic techniques and models used to elucidate complex reaction mechanisms on electrode surfaces.

The basics of oxidation and reduction reaction have been known for some time; of course, every redox reaction involves the transfer of electrons from the oxidized species to the reduced species. Most such reactions ideally occur spontaneously at their respective standard potentials, E^0. It is useful to be able to calculate the equilibrium potential of an electrochemical cell from such standard potentials, as well as to calculate the amount of current produced and the rate of the given reaction. The cell equilibrium potential can be calculated from the Nernst equation:[42]

$$E = E^0 + \frac{RT}{nF} \ln \frac{[O]^*}{[R]^*} \tag{1.1}$$

Where E is the cell equilibrium potential, R is the ideal gas constant, T is the temperature, n is the number of electrons exchanged, F is the Faraday constant, and O and R represent the equilibrium concentrations of the oxidizing and reducing species, respectively. Furthermore, the current *i* can be calculated by using the Butler Volmer equation:[42]

$$i = i_0 \left[e^{-\alpha f \eta} - e^{(1-\alpha) f \eta} \right] \tag{1.2}$$

Where i_0 is the exchange current, α is the transfer coefficient, and η is the overpotential, defined below.

Experimentally, reactions such as the oxidation of carbon monoxide do not occur at their standard potential. Thus, oxidizing CO from a platinum surface generally requires raising the applied potential to the point at which the desired reaction actually occurs. The difference between the standard potential and applied potential is known as the overpotential, as shown below.[42]

$$\eta = E - E^0 \tag{1.3}$$

Reducing the value of this overpotential is a primary goal that the improvement of electrocatalysis hopes to achieve. Electroanalysis offers the possibility of using these equations in tandem to deconvolute the mechanism of a complex reaction mechanism. For instance, kinetic analyses can be conducted by analyzing the current produced versus the overpotential, according the following relationship:[42]

$$\eta = a + b\log(i) \tag{1.4}$$

From which a Tafel plot can be created, where the exchange of each electron is expected to increase the slope of the resultant line by 120 mV/decade.

The last electrochemical model worth presenting here concerns the understanding of current-response phenomena when the potential applied to a metal surface is swept from one value to another at a fixed rate. It is from the application of this technique that we obtain linear and cyclic voltammograms. Generally a cyclic voltammogram is conceptually separated into 'anodic' and 'cathodic' sweeps; the anodic sweep begins at more negative potentials and sweeps to higher potentials, and the cathodic sweep moves in the opposite direction. The current responses that are generated from these potential sweeps can provide information about chemical processes taking place on the electrode surface. These include oxidation and reduction reactions which are sometimes highly reversible. The specific adsorption of anions such as the sulfuric acid anion, for instance, is so highly reversible on a Pt(111) crystal that it produces a current response waveform that is symmetric about the axis of zero

current.[43] This current response from the adsorption and desorption of anions can produce information leading to further studies that seek to better understand the nature of this adsorption and its effect on other processes and surface-active moieties.

Provided in Figure 1.2 is a standard cyclic voltammogram for a polycrystalline platinum electrode immersed in a solution of 0.1 M H_2SO_4. The anodic sweep is labeled with two regions, the hydrogen underpotential deposition region (H UPD) and the oxide formation region. The H UPD region seen at more cathodic potentials is uniquely defined in sulfuric acid as opposed to perchloric acid electrolytes. The cathodic sweep is notable for a long narrow negative current feature which represents the reduction of surface oxides. This redox adsorption and desorption of surface oxides will occur every time on several sequential cyclic voltammograms without any change to the onset potential of oxide formation or reduction. When oxides have covered the surface, we frequently find that the surface is blocked to reactants such as ethanol, and that the respective oxidation reactions of such fuels do not proceed as efficiently, if at all.[44, 45] However, as chapters 2, 3, and 4 will show, oxidation reactions do often occur within this region.

Very highly-reversible current-generating processes also occur during cyclic voltammetry, as can be seen in the CV of Pt(111) in 0.1 M H_2SO_4 shown in Fig 1.3. Here, the 'butterfly peak' seen at approximately 0.2 V corresponds to a rearrangement of (bi)sulfate anions on the surface, as shown by Braunschweig et al.[43] Note that the reversibility of this process is such that the positive and negative current peaks are nearly symmetric about the line of zero current. However, the mechanisms associated

with this process were not as fully understood prior to the referenced study of this system using broadband sum-frequency generation vibrational spectroscopy.

Finally, it is worth taking note of one of the mechanisms that have been proposed for surface reactions. The Langmuir-Hinshelwood[46] mechanism is arguably most relevant for fuel cell applications, as it is thought to describe the oxidation of CO to CO_2.[47] In this model, two reacting species – CO and O_2 – both adsorb to the catalyst surface and then react with one another. The implication of this is that binding sites must be available for both molecular species, and that these binding sites must be close enough for reaction between the two species to take place. Thus, merely satisfying the thermodynamic requirements for achieving lower overpotentials is not sufficient if the catalyst morphology impedes mutual adsorption of the reactants.

The models discussed above are applied with the use of several electroanalytical techniques. The techniques discussed in this dissertation – cyclic voltammetry and amperometry – are accomplished with the use of a potentiostat and standard three-electrode cell.

The three-electrode cell as employed here is a glass cell in which three electrodes – the working electrode, the reference electrode, and the auxiliary electrode – are separated by a shared electrolytic medium. The working electrode is that electrode at which anode reactions occur. The potential applied to that electrode by the potentiostat is applied with reference to the reference electrode, which is an electrode of stable and fixed potential. This stability is commonly achieved by using a highly reversible redox couple with constant reactant quantities, such as with the Ag/AgCl

electrode. A flow of current to the reference electrode is frequently undesirable as it can alter this reference potential, so an auxiliary electrode is implemented in order to collect current from the working electrode. A simplified image of the three-electrode cell used in these studies is shown in Figure 1.4. The gas inlet allows one to saturate the electrolyte solution itself or the atmosphere over that solution with a gas of choice. Typically, argon gas is used to purge the solution and atmosphere of oxygen, which would otherwise heavily distort the electrochemical measurements.

It has become clear from the last several decades of study, however, that electrochemical analysis, while providing a strong foundation for understanding electrocatalytic processes relevant to fuel cells, is not sufficient for a complete molecular-level understanding of what is occurring on catalyst surfaces.[48-51] Electrochemical analyses provide a very broad map of these processes, as seen in this work, but they provide a map that is at times too broad and conflated by many variables to be precisely interpretable. A more acute identification of adsorbate species and their adsorption behavior is crucial. This is where spectroscopy comes into play.

1.3 Spectroscopy and BB-SFG

Linear spectroscopic techniques – that is, techniques in which the observed phenomena are governed by the first-order polarization response of the studied system to an applied electric field – have been indispensable to the study of fuel cell systems. They include variants of Raman and IR spectroscopy, and have aided in the identification of reaction intermediates in a variety of fuel cell systems as well as the potential-

dependence of those intermediates. When used in-situ, such techniques can probe the behavior of intermediate species in an environment that better approximates actual fuel cell conditions. However, linear spectroscopic techniques are troubled by an inability to sufficiently disambiguate chemical species adsorbed to the surface of the electrode from those diffused in the bulk electrolyte.[26, 30, 52] Even novel variants on these techniques that emphasize the region closest to the electrode surface, such as ATR-SEIRAS (Attenuated Total Reflection Surface Enhanced Infrared Absorption Spectroscopy), lack the sensitivity and selectivity desired for clearly identifying what species are specifically adsorbed to a catalyst surface and at what applied potentials.[26]

The use of BB-SFG (Broadband Sum-Frequency Generation) vibrational spectroscopy achieves these goals.[47] It is a 2nd order non-linear technique, means that it is a phenomenon described by the 2nd order term in the polarization series expansion shown in equation 1.5.[53]

$$\vec{P}(\vec{r},t) = \vec{P}^{(1)}(\vec{r},t) + \vec{P}^{(2)}(\vec{r},t) + ... + \vec{P}^{(n)}(\vec{r},t) \quad (1.5)$$

Terms other than the first order-term are typically not observable without the application of electromagnetic fields that are at least as intense as the fields felt by electrons in a molecule.[54] Electromagnetic fields of such strength can be achieved with the use of pulsed lasers. The second order polarization term is detailed below:

$$\vec{P}^{(2)}(\vec{r},t) = \varepsilon_0 \chi^{(2)} E_1 E_2 \quad (1.6)$$

Where ε_0 is the vacuum permittivity, E_1 and E_2 are electric fields applied, in our setup, by separate infrared and visible laser pulses, and $\chi^{(2)}$ is the second-order nonlinear susceptibility tensor of the medium, which can be separated into 'resonant' and 'non-resonant' components. The resonant component $\chi^{(2)}_R$ corresponds to the resonant response of some observed chemical moiety; the non-resonant component $\chi^{(2)}_{NR}$ originates mainly from electronic excitations in the metal surface. $\chi^{(2)} = 0$ in centrosymmetric media and only takes on non-zero values at breaks in this centrosymmetry. Thus, 2nd order non-linear phenomena are only permissible at such breaks in centrosymmetry, such as the interface of a metal catalyst in liquid electrolyte. This satisfies the selectivity requirement; because 2nd order phenomena (such as SFG) are only observable at such places as the catalyst surface, no spectroscopic signals will be generated in the bulk electrolyte.[55]

In SFG spectroscopy, two coherent beams are overlapped spatially and temporally on the catalyst surface. The second-order behavior described above manifests in the generation of photons at the catalyst surface whose frequency is the sum of the frequencies of the two impinging photon beams. This is tidily summarized in equation 1.7:

$$\omega_{SFG} = \omega_{IR} + \omega_{vis} \tag{1.7}$$

Here ω represents the frequency of each photon. Functionally, SFG spectroscopy is very similar to infrared spectroscopy, although SFG-active species must be both Raman and IR-active.[38, 56] When the frequency of the impinging infrared pulse is resonant with a vibrational mode belonging to a surface-adsorbed molecular species, there is a resonant enhancement of the output SFG intensity. This is the essential phenomenon contained within the resonant portion of the 2nd order nonlinear susceptibility, $\chi^{(2)}_R$.

The two laser beams used in the following studies are a visible beam and a broadband infrared beam. The broadband IR beam is approximately 150 cm^{-1} FWHM, allowing for the acquisition of a relatively broad spectral range with one laser shot – hence the suffix 'BB' in 'BB-SFG.' Its frequency is tunable with the use of an OPA. The visible beam is fixed at 800 nm and has a bandwidth of 10-15 cm^{-1}, which limits the resolution of the acquired SFG signals.

The non-resonant response, particularly on a metal surface, is frequently sufficiently strong as to overwhelm and distort the resonant response. Therefore a method must be employed to suppress this non-resonant response in preference to the resonant signal. To accomplish this goal, the studies in this dissertation make use of a non-resonant suppression technique that employs a Fabry-Perot étalon and a mechanical delay stage.[57]

Briefly, a Fabry-Perot etalon is positioned in the path of the 800 nm source beam in order to compress it into a picosecond pulse with a 10-15 cm^{-1} bandwidth. This also causes the visible pulse to be asymmetric in the time domain. When the femtosecond

infrared pulse strikes the surface, it produces two responses. The first is a non-resonant response whose lifetime can be considered to be as long as the infrared pulse itself. The second is a resonant response that has a significantly longer lifetime. By manipulating the mechanical delay stage, the onset of the visible pulse can be shifted in the time domain so that it arrives just after the decay of the non-resonant response. Thus, the visible pulse will ideally interact only with the remaining resonant component of the IR response. The effect of this non-resonant suppression scheme is dramatic, and essentially permits the observation of vibrational bands that otherwise would be too strongly obscured by the non-resonant contribution of the metal surface.

A diagram of the cell itself is provided in Fig 1.6. A unique feature of the spectroelectrochemical cell used for the studies in this dissertation is the inclusion of a Teflon spacer with a fixed 25 micron thickness. This spacer is placed between the optical window and electrode, allowing for applied potential sweep rates of up to 5 mV/s without the detriment of ohmic drop effects that are associated with thin-layer electrochemistry. An example diagram is shown in Figure 1.7. Thus, cyclic voltammograms are obtained simultaneously with multiple acquisitions of SFG spectra. Both the spectral acquisition time and voltammetric sweep rate can be modified.

1.4 Dissertation Goals

This dissertation seeks to demonstrate the indispensable utility of broadband sum-frequency generation vibrational spectroscopy by showing evidence of its versatility across a wide range of systems and its unique insights into chemical

mechanisms relevant to the fundamental study of fuel cell catalysis. By correlating this mode of spectroscopy with electrochemical analysis, novel findings have been drawn about the behavior of adsorbed intermediates formed during the oxidation of ethanol fuels. Analyses of other liquid fuel oxidations have are also presented, and their study will lend further insight into how pH, catalyst morphology, and electrolyte composition affect fuel cell surface science. The in-situ nature of the technique brings these studies closer to an understanding of how these systems behave in an actual fuel cell environment.

Chapter 2 will explore the mechanism of ethanol oxidation in acidic electrolytes – this is a mechanism that has been explored for decades, but the following BB-SFG studies have brought a more precise understanding about a number of components of this mechanism. Specifically, the effect of electrolyte anion will be considered, the adsorption behavior of acetate and (bi)sulfate anions will be shown, and there will be investigations into the mechanism of C-C bond cleavage and CO intermediate formation. Chapter 3 will investigate this same fuel, but in alkaline electrolytes. Here, the acquired spectra reveal new information about the way that CO is formed in a high-pH environment as well as the role that surface morphology can play in manipulating the CO oxidation mechanism. Chapter 4 will include many further studies of methanol oxidation, acetaldehyde oxidation, and formic acid oxidation in an attempt to further elucidate small organic liquid reaction mechanisms on different platinum surfaces and in different electrolytes. Chapter 5 will feature a deeper investigation into the behavior of ethanol oxidation and adsorbed CO on an ordered Pt(111) surface as part of an attempt

to more precisely model CO's electronic and spectroscopic properties as a function of coverage and pH. Finally, chapter 6 will bring BB-SFG spectroscopy to a very different system and show its potential for studying even very complicated molecules; in particular, cobalt porphyrins adsorbed onto a gold surface.

1.5 References

1. W. R. Grove, *Journal of Science*, 1839, **XIV**, 127.
2. F. T. Bacon, *BEAMA Journal*, 1959, **61**, 6.
3. S. Rousseau, C. Coutanceau, C. Lamy and J.-M. Leger, *Journal of Power Sources*, 2006, **158**, 18.
4. C. Lamy, A. Lima, V. LeRhun, F. Delime, C. Coutanceau and J.-M. Léger, *J. Power Sources*, 2002, **105**, 283.
5. R. Parsons and T. Vandernoot, *Journal of Electroanalytical Chemistry*, 1988, **257**, 9.
6. S. S. Zhang, X. Z. Yuan, J. N. C. Hin, H. J. Wang, K. A. Friedrich and M. Schulze, *Journal of Power Sources*, 2009, **194**, 588.
7. A. Hayashi, T. Kosugi and H. Yoshida, *International Journal of Hydrogen Energy*, 2005, **30**, 931.
8. B. C. H. Steele and A. Heinzel, *Nature*, 2001, **414**, 345.
9. L. Schlapback and A. Zuttel, *Nature*, 2001, **414**, 353.
10. A. K. Shukla, M. K. Ravikumar and K. S. Gandhi, *J. Solid State Electrochem.*, 1998, **2**, 117.
11. J. R. Varcoe and R. C. T. Slade, *Fuel Cells*, 2005, **5**, 187.
12. N. V. Rees and R. G. Compton, *J. Solid State Electrochem.*, **15**, 2095.
13. A. L. Dicks, *Journal of Power Sources*, 1996, **61**, 113.
14. N. B. Petkova and D. Dobrev, *Oxid. Commun.*, 2009, **32**, 425.
15. L. Barelli, G. Bidini, F. Gallorini and S. Servili, *Energy*, 2008, **33**, 554.
16. V. Neburchilov, J. Martin, H. J. Wang and J. J. Zhang, *Journal of Power Sources*, 2007, **169**, 221.
17. N. T. Nguyen and S. H. Chan, *J. Micromech. Microeng.*, 2006, **16**, R1.
18. X. W. Yu and P. G. Pickup, *Journal of Power Sources*, 2008, **182**, 124.
19. W. M. Qian, D. P. Wilkinson, J. Shen, H. J. Wang and J. J. Zhang, *Journal of Power Sources*, 2006, **154**, 202.
20. T. W. Patzek, *Crit. Rev. Plant Sci.*, 2004, **23**, 519.
21. H. L. Maclean, *Int. J. Veh. Des.*, 2004, **35**, 27.
22. I. Cumalioglu, A. Ertas, Y. Ma and T. Maxwell, *J. Fuel Cell Sci. Technol.*, 2008, **5**, 10.
23. F. Vigier, C. Coutanceau, A. Perrard, E. M. Belgsir and C. Lamy, *J. Appl. Electrochem.*, 2004, **34**, 439.
24. H. Wang, Z. Jusys and R. J. Behm, *Journal of Physical Chemistry B*, 2004, **108**, 19413.
25. W. J. Zhou, S. Q. Song, W. Z. Li, G. Q. Sun, Q. Xin, S. Kontou, K. Poulianitis and P. Tsiakaras, *Solid State Ionics*, 2004, **175**, 797.
26. M. Heinen, Z. Jusys and R. J. Behm, *J. Phys. Chem. C*, 2010, **114**, 9850.
27. M. J. Giz and G. A. Camara, *J. Electroanal. Chem.*, 2009, **625**, 117.
28. S. C. S. Lai and M. T. M. Koper, *Faraday Discuss.*, 2008, **140**, 399.

29. R. S. Ferreira, V. R. Oliveira, R. Reis, G. Maia and G. A. Camara, *J. Power Sources*, 2008, **185**, 853.
30. J. F. Gomes, B. Busson, A. Tadjeddine and G. Tremiliosi-Filho, *Electrochim. Acta*, 2008, **53**, 6899.
31. M. T. M. Koper and S. C. S. Lai, *Physical Chemistry Chemical Physics*, 2009, **11**, 10446.
32. H. Helmholtz, *Pogg.ann.*, 1853, **LXXXIX**, 211.
33. G. Guoy, *Comt. Rend.*, 1909, **149**, 654.
34. D. L. Chapman, *Phil. Mag.*, 1913, **6**, 475.
35. O. Stern, *Z. Electrochem.*, 1924, **30**, 508.
36. W. Akemann, K. A. Friedrich and U. Stimming, *J. Chem. Phys.*, 2000, **113**, 6864.
37. M. Cho, C. Hess and M. Bonn, *Physical Review B*, 2002, **65**, 205423.
38. A. Lagutchev, G. Q. Lu, T. Takeshita, D. D. Dlott and A. Wieckowski, *J. Chem. Phys.*, 2006, **125**, 10.
39. G. Garcìì a, P. Rodrìì guez, V. Rosca and M. T. M. Koper, *Langmuir*, 2009, **25**, 13661.
40. G. J. Blyholder, *J. Phys. Chem*, 1964, **68**, 2772.
41. S. Ishi, Y. Ohno and B. Viswanathan, *Surf. Sci.*, 1985, **161**, 349.
42. A. J. Bard and L. R. Faulkner, *Electrochemical Methods: fundamentals and applications*, Wiley, New York, 2001.
43. B. Braunschweig, P. Mukherjee, D. D. Dlott and A. Wieckowski, *J. Am. Chem. Soc.*, 2010, **132**, 14036.
44. R. B. Kutz, B. Braunschweig, P. Mukherjee, D. D. Dlott and A. Wieckowski, *J. Phys. Chem. Lett.*, 2011, **2**, 2236.
45. R. B. Kutz, B. Braunschweig, P. Mukherjee, R. L. Behrens, D. D. Dlott and A. Wieckowski, *Journal of Catalysis*, 2010, **278**, 181.
46. K. V. Kumar, K. Porkodi and F. Rocha, *Catal. Commun.*, 2008, **9**, 82.
47. G. Q. Lu, A. Lagutchev, D. D. Dlott and A. Wieckowski, *Surf. Sci.*, 2005, **585**, 3.
48. J. P. I. de Souza, S. L. Queiroz, K. Bergamaski, E. R. Gonzalez and F. C. Nart, *Journal of Physical Chemistry B*, 2002, **106**, 9825.
49. F. Vigier, C. Coutanceau, F. Hahn, E. M. Belgsir and C. Lamy, *J. Electroanal. Chem.*, 2004, **563**, 81.
50. M. K. Rajumon, R. S. Roberts, F. Wang and P. B. Wells, *J. Chem. Soc.-Faraday Trans.*, 1998, **94**, 3699.
51. X. H. Xia, H.-D. Liess and T. Iwasita, *J. Electroanal. Chem.*, 1997, **437**, 233.
52. G. A. Camara, R. B. de Lima and T. Iwasita, *J. Electroanal. Chem.*, 2005, **585**, 128.
53. A. G. Lambert, P. B. Davies and D. J. Neivandt, *Appl. Spec. Rev.*, 2005, **40**, 103.
54. A. G. Lambert and P. B. Davies, *Appl. Spec. Rev.*, 2005, **40**, 103.
55. A. Lagutchev, A. Lozano, P. Mukherjee, S. A. Hambir and D. D. Dlott, *Spectrochim. Acta A*, 2010, **75**, 1289.
56. A. Perry, C. Niepert, B. Space and P. B. Moore, *Chem. Rev.*, 2006, **106**, 1234.
57. H. S. Lagutchev A, Dlott D, *J. Phys. Chem. C*, 2007, **111**, 3.

1.6 Figures

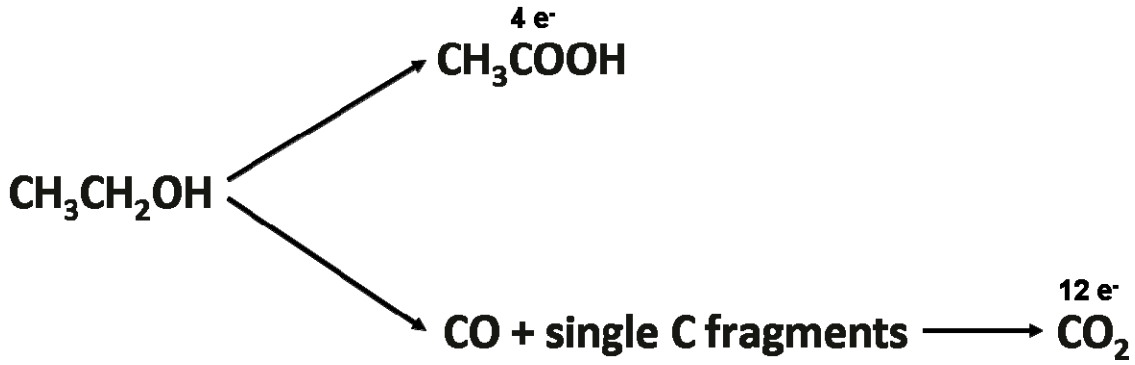

Scheme 1.1. A general outlay of the ethanol oxidation reaction, which will be explored in further detail in Chapters 2 and 3.

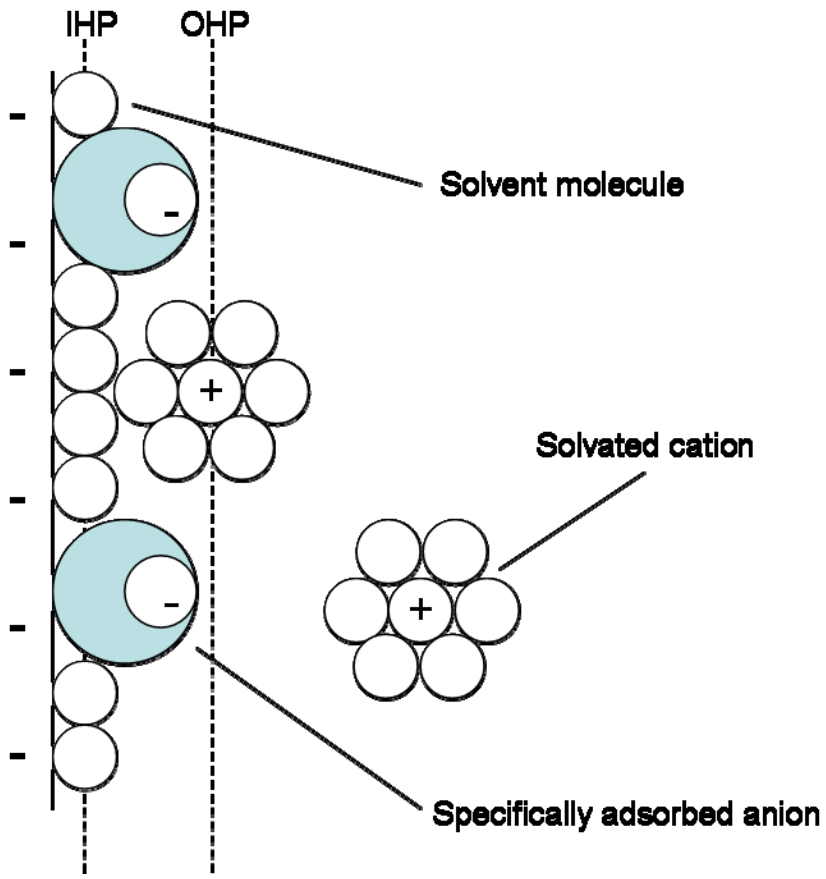

Figure 1.1. An illustrated depiction of the Gouy-Chapman-Stern model, based on Figure 1.2.3 from reference.

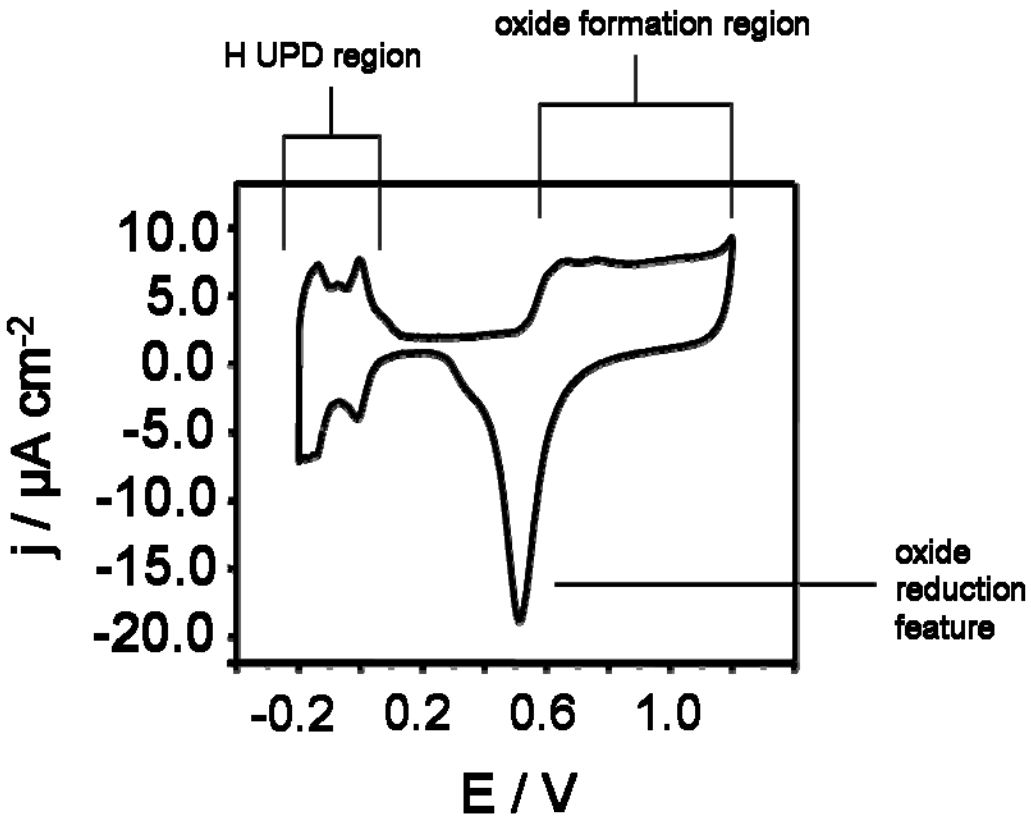

Figure 1.2. A diagram of a typical CV of polycrystalline platinum in a solution of H_2SO_4.

The potential values are given with respect to Ag/AgCl electrode.

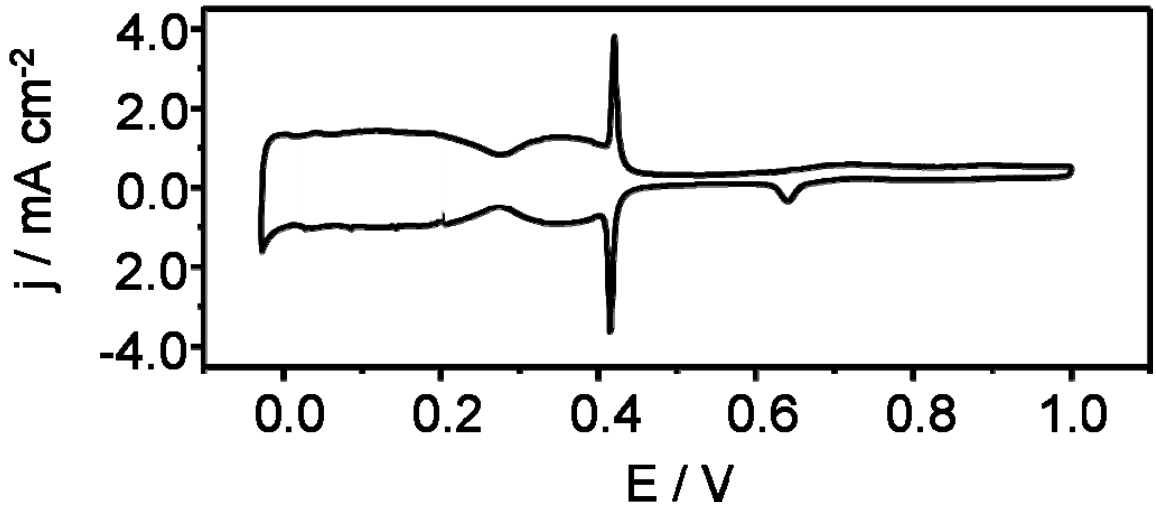

Figure 1.3. Cyclic voltammogram of Pt(111), showing the 'butterfly' peaks corresponding to the highly-reversible rearrangement of (bi)sulfate anions. Potentials are shown with respect to the RHE.

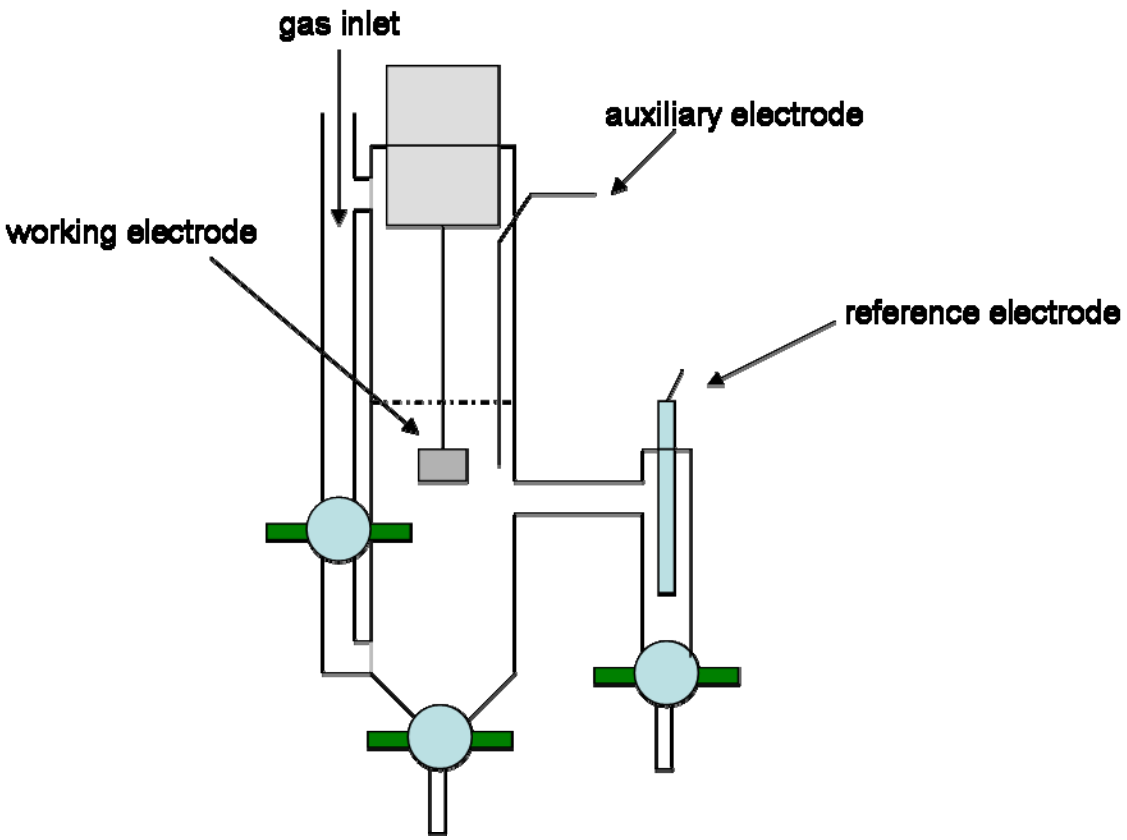

Figure 1.4. A diagram of the three-electrode cell used for the electroanalytical studies in this dissertation.

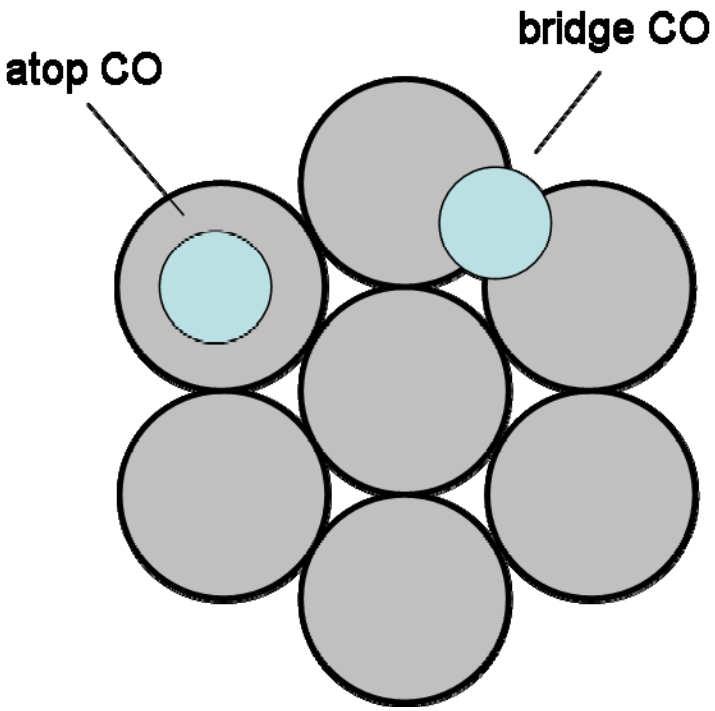

Figure 1.5. A diagram of the binding sites for CO that are observed in this work, provided here over a depicted crystal of (111) orientation.

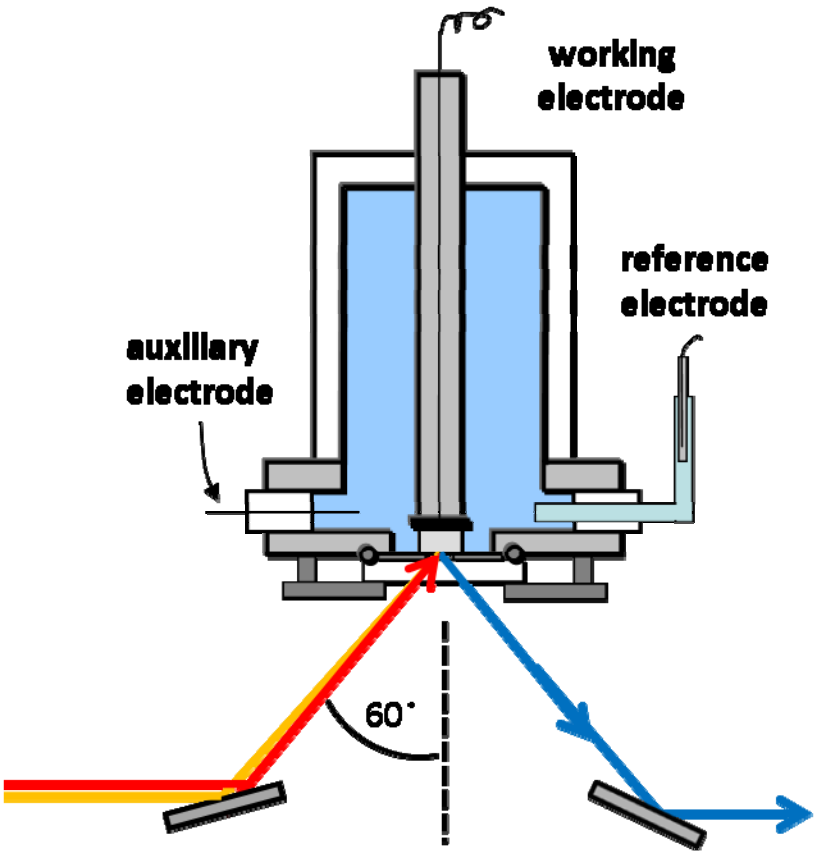

Figure 1.6. A depiction of the spectroelectrochemical cell used in these studies.

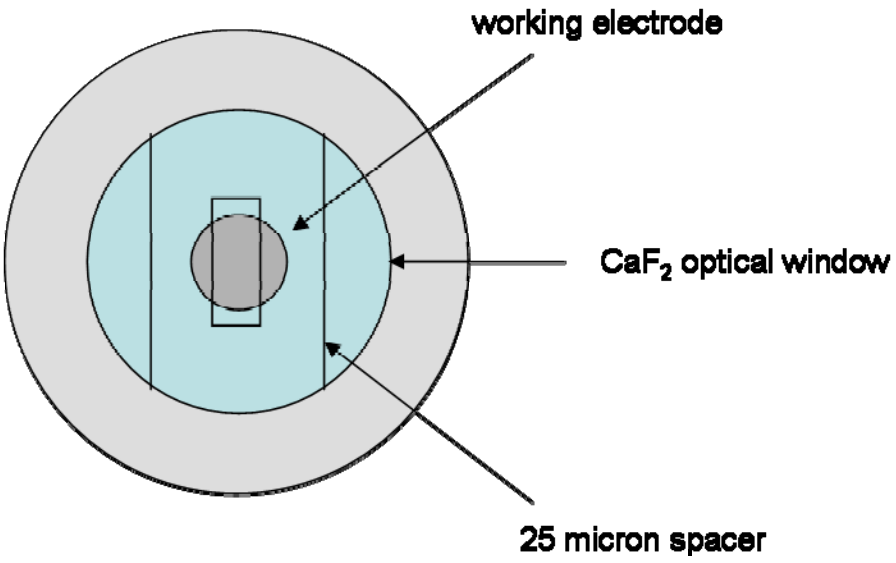

Figure 1.7. A depiction of the 25 micron Teflon spacer used to create a fixed electrolyte gap between the optical window and working electrode, allowing for sweep rates of up to 5 mV/s without ohmic drop effects.

CHAPTER 2

ETHANOL OXIDATION ON PLATINUM CATALYSTS IN ACIDIC ELECTROLYTES

2.1 Notes and Acknowledgements

This chapter is adapted from a manuscript that I authored called "Reaction Pathways of Ethanol Electrooxidation on Polycrystalline Platinum Catalysts in Acidic Electrolytes.[a]" It was published in the Journal of Catalysis in 2010 and is reproduced here with permission. It's a strong example of the versatility and power of BB-SFG when paired with electrochemistry, providing not just new insights into the formation of CO intermediates, but also into the adsorption behavior of less easily-observed chemical moieties such as acetate and (bi)sulfate.

I'd like to acknowledge several people for their assistance with this manuscript, including Drs. Rachel Behrens, Björn Braunschweig, Prabuddha Mukherjee, Dana D. Dlott, and Andrzej Wieckowski. Their patience and instruction were indispensable to my education in this field and my training as a scientist, and their assistance with this work is deeply appreciated. Research described in this study was supported by the US Army Research Office under award W911NF-08-10309 as well as from the US Air Force Office of Scientific Research under award: FA9550-09-1-0163.

[a] Kutz, R. B.; Braunschweig, B.; Mukherjee, P.; Behrens, R. L.; Dlott, D. D.; Wieckowski, A. "Reaction Pathways of Ethanol Electrooxidation on Polycrystalline Platinum Catalysts in Acidic Electrolytes." J. Catal. 2010. 278, 181.

2.2 Introduction

Ethanol is one of the most promising fuels [1-3] for alcohol-based fuel cells since it can be easily produced in large quantities from plant matter, is renewable, and its complete oxidation to CO_2 provides a comparably high yield of 12 electrons per molecule. Pt model catalysts are well known as highly active but inefficient catalysts for the oxidation of small alcohols [1, 2, 4]. Although ethanol oxidation on Pt-based catalysts has been studied for many years, the precise reaction pathways and effects of the supporting electrolyte have yet to be fully elucidated [4, 5]. Based on the observation of ethanol intermediates, very simple but incomplete models of possible reaction pathways were deduced in previous studies of ethanol electrooxidation [4, 6, 7]: multiple ethanol oxidation pathways occur simultaneously and often yield undesirable products and long-lived intermediates such as CO, acetaldehyde, and acetic acid. While CO and acetaldehyde can be further oxidized to CO_2 at fuel cell relevant potentials, acetic acid cannot, and therefore constitutes a 'dead end' for the reaction. Nevertheless, the persistence of adsorbed intermediates is indicative of an incomplete ethanol oxidation and their presence significantly reduces the efficiency of ethanol-based fuel cells. In order to design more efficient fuel cells that suppress the formation of undesired intermediates such as CO and increase the selectivity of oxidations pathways towards CO_2 formation, a molecular-level understanding of the ethanol oxidation reaction (EOR) as it occurs on the catalyst surface and the effect of the supporting electrolyte is vital. For that reason EOR has been studied previously with infrared [5, 8, 9], Raman [10, 11], and vibrational sum-frequency generation (SFG) spectroscopy [9, 12]. However, Raman and IR

studies can suffer from background issues and often struggle to disambiguate surface-adsorbed molecules from those diffused in the bulk solution [4, 13, 14]. Additionally, SFG studies of EOR have been limited so far to investigations of CO vibrational bands [9, 12, 15]. As a result, observations of acetaldehyde [5, 8, 13] adsorbed acetyl [4, 13] and acetic acid or acetate [5, 8, 13] have, until now, been limited to linear spectroscopic techniques.

In this article we have applied surface specific and background-free (Section 2.3, below) SFG experiments to study ethanol oxidation reactions. We report the first SFG spectra of adsorbed acetate and co-adsorbed sulfuric acid anions during ethanol oxidation, while first SFG studies with isotopically-labeled ethanol reveal significant new information on C–C bond cleavage and the behavior of adsorbed single-carbon fragments from ethanol oxidation on polycrystalline Pt.

2.3 Experimental Methods and SFG Modeling

Sum-frequency generation (SFG) has been developed into a powerful vibrational spectroscopic technique for studies of surfaces and interfaces [16]. The sum-frequency ω_{SF} originates from a second-order nonlinear process and is generated by overlapping a tunable infrared and a fixed visible laser beam in time and space at the interface of interest. The SFG intensity is proportional to the square of the second-order susceptibility $\chi^{(2)}$ [17], which vanishes within the dipole approximation in the bulk of centrosymmetric materials such as platinum and aqueous electrolytes. Surfaces and interfaces, however, necessarily break the prevailing bulk symmetry and give rise to

non-vanishing $\chi^{(2)}$ contributions from the interface. The following equation describes the model used for the intensity $I(\omega_{SF})$ of the SFG signals and its dependent parameters:

$$I(\omega_{SF}) \propto \left| \chi_{NR}^{(2)} + \sum_q \frac{A_q \cdot e^{-i\theta_q}}{(\omega_{IR} - \omega_q) + i\Gamma_q} \right|^2 \cdot I(\omega_{vis}) I(\omega_{IR}) \exp\left[-4 \ln 2 \frac{(\omega - \Omega)^2}{\Delta^2} \right]$$

Here, Ω and Δ refer to the frequency and bandwidth of the impinging broadband infrared (BBIR) pulse, while A_q, θ_q, ω_q, and Γ_q are amplitude, relative phase, frequency, and homogenous linewidth of the q-th vibrational mode, respectively. $\chi_{NR}^{(2)}$ is the non-resonant component of the interfacial second-order nonlinear susceptibility $\chi^{(2)}$. $\chi_{NR}^{(2)}$ is nearly independent of the BBIR frequency Ω and manifests as a featureless SFG contribution produced by the surface, but is highly dependent on the electronic structure of the surface [17]. Modifications such as a change in the surface oxidation or the presence of strongly adsorbed molecules such as CO can alter the interfacial electronic structure and influence $\chi_{NR}^{(2)}$ considerably. Thus, $\chi_{NR}^{(2)}$ is not a background, because it contains useful information about the electronic nature of the catalyst surface as well as a phase reference for determining the orientations of adsorbed molecular species [17-20]. Because we are mostly interested in resonant contributions of $\chi^{(2)}$ which are associated with adsorbed molecular species, we have applied a $\chi_{NR}^{(2)}$ suppression technique previously reported by Lagutchev et al. [21, 22]. This technique,

however, requires a compromise between a complete suppression of $\chi_{NR}^{(2)}$ and maintaining a relatively good signal-to-noise ratio of the observed vibrational bands.

In all SFG and electrochemical experiments a polished polycrystalline platinum disk (Matek) with a diameter of 6mm was used as working electrode. A flame-annealed platinum wire (99.99%) and a commercial Ag/AgCl (BASi; MF-2052; -0.25 vs. RHE) electrode served as counter and reference electrodes, respectively. All potentials throughout this article are reported with respect to this Ag/AgCl reference. Voltammetric experiments in 0.1 M H_2SO_4 and $HClO_4$ electrolytes (double distilled, GFS Chemicals) with 0.5 M ethanol CH_3CH_2OH (99.5%) were recorded with a Princeton Applied Research (PAR 263A) potentiostat. Solutions of 0.2 M isotopically-labeled ethanol were made in 0.1 M $HClO_4$ with $^{12}CH_3{}^{13}CH_2OH$ (>99%). All electrolytes used in this study were prepared with ultra-pure water (≥18.2 MΩ, total oxidizable carbon ≤ 4ppb) obtained from a Millipore Gradient A10 purification system and were thoroughly purged with Ar gas (ultra-high purity). Prior to each experiment, the Pt disk was cleaned in concentrated sulfuric acid, rinsed with ultrapure water, and electrochemically cleaned by potential cycling between -0.28 and 1.4 V for 50 or more cycles at a sweep rate of 200 mV/s.

The BB-SFG apparatus for spectro-electrochemistry employed in this study allows for rapid acquisitions of vibrational spectra synchronized with a voltammetric scan and has been reported elsewhere [23]. Tunable broadband infrared (BBIR) pulses were generated in an optical parametric amplifier (Light Conversion; Topas) pumped by a femtosecond Ti:Sapphire laser system (Quantronix; Integra C series) at a repetition rate of 1 kHz. The

BBIR pulses had pulse durations of ~120 fs, typical bandwidths Δ >150 cm^{-1} and pulse energies of approximately 8 and 3 μJ at frequencies Ω of 2083 and 1429 cm^{-1}, respectively. Narrowband visible pulses with 5 μJ pulse energy and a fixed wavelength of 800 nm were generated by narrowing the fs pulses to a bandwidth of <10 cm^{-1} with a Fabry-Pérot etalon. Narrow-band visible and BBIR pulses were overlapped in time and space at an incident angle of ~60º to the normal of the Pt-electrolyte interface. Sum-frequency photons were collected with a spectrograph and a charge-coupled device (CCD). The SFG, visible, and IR photons were all p-polarized. Spectro-electrochemical experiments were carried out in a previously described [23] electrochemical cell for synchronized SFG and electrochemical experiments. In this electrochemical cell, a well-defined gap of 25 μm between the electrode surface and a CaF_2 optical window is established by a Teflon spacer of the same thickness. The 25 μm electrolyte gap allows for voltammetric scans at sweep rates of ≤ 5 mV/s without the detriment of strong ohmic drop effects that are associated with thin-layer electrochemistry [23].

2.4 Results

Hanging-meniscus cyclic voltammograms (CVs) of 0.5 M ethanol electrooxidation on a polycrystalline Pt surface immersed in 0.1 M perchloric acid and 0.1 M sulfuric acid solutions are presented in Fig. 2.2a and b, respectively. These CVs reveal four distinct voltammetric features, which are characteristic of ethanol oxidation (three features on the anodic and one on the cathodic sweep) that are qualitatively similar in both electrolytes. The onsets of the three features on the anodic sweep appear at

approximately 0.2V, 0.4V and 0.75 V respectively. The first two oxidation features are more distinct in sulfuric acid electrolyte than in the perchloric acid electrolyte. On the cathodic sweep, the onset of a reactivation feature corresponding to the reductive stripping of Pt surface oxides and subsequent ethanol oxidation is observed around 0.5 to 0.6 V (Fig. 2.2).

Chronoamperometric measurements for the electrooxidation of 0.5 M ethanol on polycrystalline Pt were performed in order to demonstrate the long-term difference in current densities produced in sulfuric and perchloric acid solutions. Fig. 2.3 shows the chronoamperograms (CAs) at potentials of 0, 0.5 and 0.8 V. At 0.5 V, the current density in perchloric acid reaches equilibrium at ~0.8 mA/cm^2, whereas in sulfuric acid the equilibrium is established at a notably lower current density of ~0.6 mA/cm^2 (Fig. 2.3). Similarly, at 0.8 V the current density equilibrates at ~0.3 mA/cm^2 in perchloric and slightly below ~0.2 mA/cm^2 in sulfuric acid solution. Although the current densities for each of the above electrochemical measurements are consistently lower in sulfuric acid, the overall shape of the chronoamperograms is similar in both electrolytes.

Fig. 4a and b present two series of potentiodynamic BB-SFG spectra recorded in 0.5 M regular ethanol ($^{12}CH_3{}^{13}CH_2OH$) on a polycrystalline Pt electrode in 0.1 M $HClO_4$ and 0.1 M H_2SO_4, respectively. Vibrational bands in Fig. 4 correspond to adsorbed CO molecules which are formed by electrooxidation of ethanol. For these experiments, the BBIR frequency was tuned to ~1960 cm^{-1} to excite vibrations of CO molecules adsorbed on both Pt atop (~2080 cm^{-1}) and Pt bridge sites (1850 cm^{-1}). Vibrational bands attributable to CO molecules adsorbed on Pt atop sites are observed in both supporting

electrolytes, while vibrational bands at 1850cm^{-1} due to CO molecules adsorbed on bridge sites are present in sulfuric acid solution only.

The electrooxidation of isotopically-labeled ethanol was studied with SFG in order to elucidate the formation of CO. BB-SFG spectra with the BBIR pulse centered at 2174 cm^{-1} were recorded in 0.1 M $HClO_4$ with 0.2 M isotopically-labeled ethanol ($^{12}CH_3{}^{13}CH_2OH$) and are presented in Fig. 2.5a and b, respectively. Fig. 2.5a reveals two vibrational bands at 2030 cm^{-1} and 2100 cm^{-1} that are attributable to ^{13}CO and ^{12}CO molecules adsorbed onto Pt atop sites, respectively. Note that the SFG intensity of the ^{13}CO vibrational band is much higher than the SFG intensity of the ^{12}CO vibrational band. In order to obtain a better understanding of surface-adsorbed intermediates of ethanol and their potential dependence we have fitted the vibrational bands with model functions of the interfacial second-order susceptibility $\chi^{(2)}$ and with A_q, Γ_q, ω_q and $\chi_{NR}^{(2)}$ as adjustable parameters (see section 2.3). The amplitudes A_q of the atop CO band arising from regular ethanol ($^{12}CH_3{}^{13}CH_2OH$) as a function of applied potential are shown in Fig. 2.6a and 2.6b for $HClO_4$ and H_2SO_4 solutions, respectively. As reported earlier, the vibrational band assigned to bridge-bonded CO is observed only in sulfuric acid electrolyte and its amplitude is presented in Fig. 2.6c. The amplitudes of ^{13}CO and ^{12}CO vibrational bands are shown in Fig. 2.7a and b, respectively. The potential dependences of all CO vibrational band amplitudes in Figs. 2.6-2.7 follow very similar behavior during both the anodic and cathodic sweeps. After an initial slight increase of the CO amplitudes for potentials *E* from -0.2 to 0.4 V, they start to decrease rapidly for E >0.4 V to negligible values for *E* >0.7 V. The amplitudes remain negligible through the end of

the anodic sweep and do not begin to increase again until potentials of *E* <0.6 V are established during the cathodic sweep (Figs. 2.6-7).

Fig. 2.8 presents a comparison of SFG spectra recorded at two different BBIR frequencies during the electrooxidation of ethanol on a polycrystalline Pt surface in 0.1 M H_2SO_4. In Fig. 2.8a the frequency of the BBIR pulse was tuned to 2080 cm^{-1} to excite CO stretching vibrations, while in Fig. 2.8b the BBIR frequency was at ~1400 cm^{-1} to probe vibrational bands attributable to adsorbed acetate and adsorbed sulfuric acid anions. The SFG spectra in Fig. 8a show a vibrational band at ca. 2080 cm^{-1} corresponding to the adsorption of CO molecules on the Pt surface at potentials *E* <0.4 V. CO is oxidatively removed from the Pt surface at *E*>0.4V which results in a dramatic decrease in the intensity of the CO vibrational band. SFG spectra at *E* >0.6 V in Fig. 2.8a appear featureless and indicate the absence of adsorbed CO for these potentials. In Fig. 8b a broad feature arises at 1300 cm^{-1} between -0.2 and 0.4 V due to a non-resonant contribution to the SFG intensity (see section 2.3, Eqn (1)). The amplitude $\chi_{NR}^{(2)}$ of this non-resonant contribution is plotted as a function of electrode potential in Fig. 6d. For *E* >0.4 V, $\chi_{NR}^{(2)}$ contributions rapidly decrease to negligible values in the anodic sweep and recover during the cathodic sweep for potentials <0.6 V (Fig. 6d). It should be noted that the potential dependence of $\chi_{NR}^{(2)}$ for both anodic and cathodic sweep follows exactly the potential dependence of the previously described CO vibrational bands (Figs. 2.4-7).

At potentials between 0.5 and 1.0 V with negligible $\chi_{NR}^{(2)}$ contributions and in the absence of adsorbed CO (Fig. 2.5-7), vibrational bands at ~1400 cm^{-1} and ~1280 cm^{-1} are

observed. These bands are assigned to symmetric carboxylate ($-^{12}COO^-$) stretching vibrations of adsorbed acetate [4, 13, 24] (~1410 cm^{-1}) and S−O stretching vibrations of co-adsorbed sulfuric acid anions (~1280 cm^{-1}). The precise nature of this species is still a matter of considerable debate [25-27]. Radiotracer, voltammetry, and STM experiments suggest that this molecular adsorbate is sulfate [26-28], while infrared studies suggest that it is bisulfate [29, 30]. In recognition of this uncertainty, we refer to this adsorbing species as (bi)sulfate [4, 31, 32]. Figs. 2.8a and 2.8b enhance this particularly interesting potential and frequency region for $HClO_4$ and H_2SO_4 electrolytes, respectively. In both electrolytes the acetate vibrational band at ~1410 cm^{-1} arises at E >0.6 V, increases in intensity with increasing potential, reaches a local maximum and subsequently decreases to negligible intensities prior to 1.0 V. On the cathodic sweep, a similar intensity-potential profile is observed in the same potential region. The vibrational band assigned to co-adsorbed (bi)sulfate is, however, observed in H_2SO_4 electrolyte only (Fig. 2.9). Fig. 2.10 shows the amplitudes A_q of acetate and (bi)sulfate bands as a function of the applied potential. In $HClO_4$ the maximum amplitude of the acetate vibrational band is observed around 0.7 V for both anodic and cathodic sweeps (Fig. 2.10a) while Fig. 2.10b reveals acetate adsorption in dilute H_2SO_4 in a wider potential range with the maximum amplitude at a much higher potential of 0.9 V. The amplitude of the (bi)sulfate band increases for potentials >0.7 V and reaches its maximum at the end of the anodic sweep. During the cathodic sweep it steadily decreases from 1 V to 0.6 V, where it is displaced by the newly formed CO adlayer.

In addition to the SFG experiments with regular ethanol ($^{12}CH_3{}^{13}CH_2OH$) in this frequency region, potentiodynamic SFG spectra shown in Fig. 2.5b were recorded during electrooxidation of isotopically-labeled ethanol ($^{12}CH_3{}^{13}CH_2OH$) and reveal a vibrational band due to symmetric $-^{13}COO^-$ stretching vibrations of adsorbed and isotopically-labeled acetate. A comparison of the spectra in Fig. 2.9a-b reveals remarkable differences in the linewidths Γ_q of the acetate vibrational bands between the two different supporting electrolytes (Tab. 1). In perchloric acid solution the linewidth Γ_q is ~50 cm^{-1}, where as in sulfuric acid Γ_q is ~29 cm^{-1} only. The linewidth of the labeled acetate shown in Fig. 2.5b is ~25 cm^{-1}.

2.5 Discussion

Potentiodynamic SFG spectra that were recorded during the electrooxidation of both regular and isotopically-labeled ethanol reveal CO as the main surface-adsorbed intermediate at *E*<0.6 V (Figs. 2.5 and 2.8). Increasing the electrode potential leads to an oxidative removal of CO and to the predominant adsorption of acetate and, in the case of a H_2SO_4 electrolyte, to the co-adsorption of (bi)sulfate anions (Fig. 2.9). On the basis of our spectroscopic and voltammetric observations, we propose a reaction mechanism for ethanol electrooxidation on polycrystalline Pt in Scheme 2.1, which will be substantiated and discussed later in the text. Scheme 2.1 shows oxidation of ethanol by dehydrogenation and the formation of acetaldehyde in step (a). In step (b) adsorbed acetaldehyde and adsorbed ethanol (parallel to (a)) quickly decomposes into surface-

adsorbed $–CH_x$ and $–CH_xO$ fragments [10]. Note that no direct observation has been made of a $–CH_xO$ fragment, and we use it here as a convenient and necessary logical precursor to the more oxidized CO molecule, however short-lived such a fragment may be. These fragments can oxidize and form adsorbed CO (step (c)) at potentials as low as -0.2 V, (Section 2.5.1). For electrode potentials $\geq$0.4 V, the adsorbed CO molecules oxidize further to CO_2 (step (d)) (Section 2.5.2), which diffuses away from the catalyst surface. Not all single-carbon fragments of ethanol oxidize to CO and subsequently to CO_2, however. As shown in step (e) of Scheme 1, adsorbed $–CH_x$ fragments can be electroreduced at sufficiently low potentials to CH_4, which subsequently desorbs from the surface and diffuses in the bulk electrolyte [33, 34] In the likely case that the C–C bond is not broken, acetaldehyde can oxidize to adsorbed acetate (step (f)) (Section 2.5.3). At this point, the adsorbed acetate can only diffuse from the surface by conversion to acetic acid (step (g)). Further oxidation of acetic acid to CO_2 at fuel cell relevant potentials is not possible. Therefore, the formation of this product represents an undesirable 'dead-end' of the ethanol oxidation.

2.5.1 Electrooxidation of –CHx and –CHxO fragments from ethanol

The formation of CO from both $–CH_x$ and $–CH_xO$ fragments (step (c)) is confirmed by our spectroscopic data on the electrooxidation of regular (Fig. 2.4) and isotopically-labeled ethanol ($^{12}CH_3{}^{13}CH_2OH$) (Fig. 2.5). In Fig. 2.5 CO vibrational bands of both ^{12}CO and ^{13}CO are clearly resolved and indicative of the oxidation of ethanol fragments in step (c). The coverages of ^{13}CO and ^{12}CO are not identical, however, as we observe a

greater quantity of ^{13}CO formed from the $-^{13}COH$ fragment. Because the latter fragment is already partially oxidized, further oxidation to CO is far more facile than the oxidation of $-^{12}CH_x$ fragments, as is evidenced by the SFG amplitudes shown in Fig. 2.7. Here, the amplitude of the ^{13}CO vibrational band is considerably higher than the amplitude of the ^{12}CO vibrational band. Such a difference strongly implies that the surface coverage of adsorbed ^{13}CO molecules is much higher than the surface coverage of adsorbed ^{12}CO molecules, and consequently indicates that the $-^{12}CH_x$ fragment oxidizes to ^{12}CO to a far lesser extent. At this point it should be noted that dipole-dipole coupling effects arising from interactions between the different CO species could be the cause for different ^{13}CO and ^{12}CO SFG amplitudes. These coupling effects, which are well-known phenomena observed in closed-packed CO adlayers [35-37] may shift vibrational intensity from the ^{12}CO vibrational band to the ^{13}CO vibrational band and consequently result in a virtually lower ^{12}CO intensity. If such a shift in intensity were present in Fig. 2.5a, then the higher amplitude we observe in the ^{13}CO vibrational peak would not necessarily correspond to higher ^{13}CO coverages. However, this scenario is rather unlikely since a previous analysis of dipole-coupling effects with well-defined mixtures of $^{12}CO/^{13}CO$ on Pt(111) by Severson et al. [35] shows the opposite behavior. In their work, Severson et. al. showed that for well-defined mixtures with >17% ^{12}CO, the ^{12}CO vibrational band dominated the infrared spectra. It therefore appears clear that there is an intensity shift from the ^{13}CO vibrational band to the ^{12}CO band. Thus, if our Pt catalyst has an equal coverage of ^{13}CO molecules (formed from $-CH_xO$ fragments) and ^{12}CO molecules (formed from $-CH_x$) fragments, we would expect much higher intensities of the ^{12}CO vibrational band. The

fact that we see the opposite, a higher intensity of ^{13}CO vibrational bands, suggests that the surface coverage of ^{12}CO molecules is less than 17%. This is further supported in an FTIR study of ethanol ($^{12}CH_3{}^{13}CH_2OH$) oxidation on Pt(332) surfaces performed by Souza-Garcia et al [38]. They are unable to observe ^{12}CO at potentials lower than 0.2 V, but infer the existence of an adsorbed $–CH_x$ species by comparing the intensities of the consequent $^{12}CO_2$ and $^{13}CO_2$ vibrational peaks. They report that the intensities of $^{12}CO_2$ compared to $^{13}CO_2$ vibrational bands are different by a ratio of 1:3 [38]. We therefore conclude that the oxidation of adsorbed $–CH_x$ species to CO is significantly more difficult than the oxidation of $–CH_xO$ species and leads to an accumulation of adsorbed $–CH_x$. At potentials lower than 0 V, adsorbed $–CH_x$ species can be electroreduced to methane, as shown in step (e) of Scheme 2.1. This is supported by prior studies using differential electrochemical mass spectrometry (DEMS) [33, 34] as well as a SERS study that observed surface-adsorbed $–CH_x$ species [10]. Therefore, the electrooxidation of adsorbed $–CH_x$ species to CO is expected to be less efficient and competes with the electroreduction to CH_4, and has to be considered as a serious issue in the performance of ethanol-based fuel cells.

2.5.2 Electrooxidation of CO from ethanol

Our spectroscopic results presented in Figs. 2.4-2.8 show that as soon as the electrode potential is increased to 0.4 V there is a steady drop in the intensity of the CO vibrational bands, as is most clearly seen in the corresponding SFG amplitudes in Figs. 2.6-7. This drop in amplitude originates from the oxidative removal of CO from the Pt

surface and the formation of CO_2 according to step (d) in Scheme 2.1. The dramatic decrease in CO amplitudes (Figs. 2.6-7) at potentials >0.4 V coincides with the first voltammetric feature at the same potentials Fig. 2.2(a-b). This voltammetric feature on the anodic potential sweep corresponds largely to CO oxidation, as confirmed in prior studies by Hitmi et al. [39]. Conversely, on the cathodic potential sweep, we see the re-appearance of the CO vibrational band at E<0.4 V, where the Pt oxide layer is stripped and ethanol is oxidized to CO on active Pt sites. There is a slight hysteresis observed in the recovery of the CO atop vibrational band amplitude at E<0.4 V on the cathodic sweep, seen in Fig 2.5(a-b). This is likely attributable to the slow diffusion of ethanol into the 25 μm gap and subsequent accumulation of CO on the atop Pt sites. We do not observe such a slow rise in the vibrational band amplitude at the beginning of the anodic sweep because the electrode is held at 0 V for several minutes prior to the scan, which is sufficient time to achieve saturation coverage of CO molecules on the catalyst surface. The recovery of bridge-bonded CO (Fig. 2.6c) is more reversible, as one might expect given that CO binds more preferentially to these bridge sites when overall CO coverage is lower [40]. The $\chi_{NR}^{(2)}$ amplitude is also highly reversible. A close comparison of Figs. 5a-c with 5d as well as a comparison of Fig. 2.8 a and b reveal a nearly identical potential dependence of the non-resonant contribution $\chi_{NR}^{(2)}$ (Eqn. (2.1)) compared to the potential dependence of the CO amplitudes. In fact, Fig. 2.8 shows substantial changes in the contribution of $\chi_{NR}^{(2)}$ as soon as the CO adlayer starts to oxidize. We recall that the $\chi_{NR}^{(2)}$ contribution is purely electronic in origin and is caused by the non-linear

response of free electrons at the metal side of the interface. The strong chemisorption of CO on most metal surfaces localizes the electrons in the adsorbate-metal bonds and consequently decreases $\chi_{NR}^{(2)}$ contributions [18, 19]. Consequently, the observed changes in $\chi_{NR}^{(2)}$ can be attributed to changes in CO coverage [20, 41].

In addition to the potential-induced changes in CO coverage, a significant effect of the H_2SO_4 and $HClO_4$ supporting electrolyte on CO amplitudes and CO binding behavior is observed. Fig. 2.4 shows that the vibrational band assigned to CO molecules bound to bridge sites of the Pt electrode is observed in sulfuric acid electrolyte only. This observation is in agreement with previous studies of ethanol electrooxidation which also report the absence of bridge-bound CO in $HClO_4$ [10, 14, 34, 42]. The presence of CO molecules on bridge sites in vibrational SFG spectra (Fig. 2.4b) is indicative of an overall lower surface coverage of CO in sulfuric acid electrolyte. This conclusion is supported (i.) by previous spectroscopic studies of CO on Pt surfaces which established that CO molecules bind preferentially to Pt bridge sites when the overall coverage of CO molecules is lower [40] and (ii.) by our electrochemical data, which show significantly lower current densities from ethanol oxidation in sulfuric acid media compared to perchloric acid media (Fig. 2.2-2.3). Furthermore, prior studies of anion adsorption have shown that sulfate anions adsorb more strongly than perchlorate anions [43] and that this increased adsorption strength can result in less frequent cleavage of the C–C bond [44], therefore yielding fewer adsorbed CO molecules. These results suggest that (bi)sulfate anions inhibit ethanol oxidation at potentials as low as 0 V [45-47] and can significantly reduce the efficiency of ethanol-based fuel cells.

2.5.3 Formation of acetate species from ethanol oxidation

After the CO adlayer has been stripped from the Pt surface at potentials >0.4 V, Pt surface sites become available for other more weakly adsorbed molecular species such as acetate or (bi)sulfate. In fact, a vibrational band of adsorbed acetate arises, as shown in Figs. 2.8 and 2.9 at these potentials. The formation of acetate is represented as step (f) in the reaction Scheme 1. Additionally, we observe a pronounced effect of the supporting electrolyte on the presence and potential dependence of interfacial molecular species. Fig. 2.9b shows an additional vibrational band at 1280 cm^{-1} attributable to (bi)sulfate anions that is present between 0.5 and 0.9 V in sulfuric acid solution but absent in perchloric acid (Fig. 2.9a). Co-adsorption of (bi)sulfate with the acetate anion widens the potential range in which both anions are adsorbed. This is most clearly seen in Fig. 2.10, which contrasts the potential dependence of acetate and (bi)sulfate amplitudes. In comparison to the acetate band in sulfuric acid media, the band in perchloric acid media is found in a much narrower potential range of approximately 0.6 to 0.8 V (Fig. 10a). In addition to the different potential dependence of acetate adlayers in both supporting electrolytes, co-adsorbed (bi)sulfate confines the acetate anions on the Pt surface in a more ordered fashion. The latter is evidenced by a notably smaller linewidth Γ_q of acetate vibrational bands in sulfuric acid compared to perchloric acid solutions (Tab. 2.1). Furthermore, the decline of the acetate vibrational band amplitude on the cathodic sweep occurs between 0.5 and 0.6 V (Fig. 2.10), which

corresponds with the voltammetric reactivation of the Pt surface via the removal of surface oxides (Fig. 2.2). Once this acetate vibrational band disappears and the surface oxides are removed, the CO vibrational band once again emerges on the cathodic sweep (Fig. 2.8).

The acetate anion, however, does not oxidize within the potential range in which fuel cells operate and thus either diffuses from the surface as acetic acid (step (g) in Scheme 2.1) or blocks Pt catalyst sites. The stabilization of acetate on the surface by (bi)sulfate co-adsorption additionally discourages the use of dilute sulfuric acid as an electrolytic medium for fuel cells, since the reaction pathway in which acetate and acetic acid are produced yields only four electrons per ethanol molecule and is therefore undesirable.

2.5.4 Other surface adsorbed ethanol intermediates

In this section we will address other possible intermediates that have been frequently reported by previous studies of ethanol electrooxidation on polycrystalline Pt surfaces. Acetaldehyde is well-established as a reaction intermediate and has been identified mostly by infrared spectroscopy [12, 42]. So far it is agreed that acetaldehyde either desorbs from the Pt surface and diffuses in the bulk electrolyte or it remains adsorbed on the surface but is quickly decomposed into CO via steps (b) and (c) of Scheme 2.1. Further oxidation of acetaldehyde to acetate and subsequently to acetic acid is also possible (steps (f) and (g)). Heinen et al. report in their recent study of ethanol oxidation on thin-film Pt electrodes an acetyl anionic species with a vibrational

band at ca. 1630 cm^{-1}. Hypothetically, this species is a long-lived surface-adsorbed intermediate of ethanol and acetaldehyde electrooxidation. As Heinen et al. point out, the observation of molecular species with vibrational bands in the frequency region of 1600 to 1700 cm^{-1} with linear-optical infrared spectroscopy, is impaired by potential-induced background changes related to the changing molecular structure of interfacial H_2O. The broad bending mode of liquid water is at 1644 cm^{-1} [48] which renders the unambiguous identification of molecular species such as acetyl extremely difficult. One way to circumvent this problem is to substitute D_2O for H_2O for these experiments. D_2O has no strong adsorption bands for frequencies of 1600 to 1700 cm^{-1} and is well-suited to verify possible acetyl bands. We have therefore performed additional background-free vibrational SFG experiments of ethanol oxidation in electrolytes that substituted D_2O for H_2O. We did not observe any acetyl vibrational bands at or around 1630 cm^{-1} in our broadband SFG spectra, which in fact appeared featureless.

2.6 Conclusions

Reaction pathways of ethanol electrooxidation on polycrystalline Pt electrodes in contact with H_2SO_4 and $HClO_4$ electrolytes were studied with broadband sum-frequency generation and electrochemistry. In this article we report the first SFG spectra of acetate and (bi)sulfate co-adsorption during ethanol oxidation. A summary of all possible pathways substantiated by our experimental results is given in Scheme 1. Low potentials (E<0.4 V) produce pathways that lead to the formation of CO, while for E>0.4 V, acetate is the main surface product of ethanol electrooxidation. Our observations of

^{12}CO and ^{13}CO species from the electrooxidation of isotopically-labeled ethanol ($^{12}CH_3{}^{13}CH_2OH$) show that the carbon−carbon bond of an ethanol molecule can be easily broken at low potentials. Oxidation of the resultant $–CH_x$ fragment to molecular CO is, however, far less easy than the oxidation of the complementary $–CH_xO$ fragment. In fact, although we show the first spectroscopic evidence that the $–CH_x$ fragment can oxidize even at -0.2 V, only a small fraction of $–CH_x$ is oxidized, while the rest possibly undergoes electroreduction to methane at potentials lower than 0 V. A comparison of SFG vibrational spectra and voltammetric data reveal significant effects of the supporting electrolyte: ethanol electrooxidation in H_2SO_4 results in lower current densities, adsorption of CO onto Pt bridge sites, and co-adsorption of acetate with (bi)sulfate in a relatively wide potential range, none of which is observed in $HClO_4$.

2.7 References

1. C. Lamy, A. Lima, V. LeRhun, F. Delime, C. Coutanceau and J.-M. Léger, *J. Power Sources*, 2002, **105**, 283-296.
2. C. Lamy, S. Rousseau, E. M. Belgsir, C. Coutanceau and J. M. Leger, *Electrochim. Acta*, 2004, **49**, 3901-3908.
3. F. Vigier, C. Coutanceau, A. Perrard, E. M. Belgsir and C. Lamy, *J. Appl. Electrochem.*, 2004, **34**, 439-446.
4. M. Heinen, Z. Jusys and R. J. Behm, *J. Phys. Chem. C*, 2010, **114**.
5. F. Colmati, G. Tremiliosi-Filho, E. R. Gonzalez, A. Berna, E. Herrero and J. M. Feliu, *Faraday Discuss.*, 2008, **140**, 379-397.
6. S. C. S. Lai and M. T. M. Koper, *Faraday Discuss.*, 2008, **140**, 399-416.
7. R. S. Ferreira, V. R. Oliveira, R. Reis, G. Maia and G. A. Camara, *J. Power Sources*, 2008, **185**, 853-856.
8. M. J. Giz and G. A. Camara, *J. Electroanal. Chem.*, 2009, **625**, 117-122.
9. J. F. Gomes, B. Busson, A. Tadjeddine and G. Tremiliosi-Filho, *Electrochim. Acta*, 2008, **53**, 6899-6905.
10. S. C. S. Lai, S. E. F. Kleyn, V. Rosca and M. T. M. Koper, *J. Phys. Chem. C*, 2008, **112**, 19080-19087.
11. Q. L. Zhong, B. Zhang, Y. M. Ding, Y. L. Liu, G. S. Rao, G. F. Wang, B. Ren and Z. Q. Tian, *Acta Phys.-Chim. Sin.*, 2007, **23**, 1432-1436.
12. J. F. Gomes, B. Busson and A. Tadjeddine, *J. Phys. Chem. B*, 2006, **110**, 5508-5514.
13. M. H. Shao and R. R. Adzic, *Electrochim. Acta*, 2005, **50**, 2415-2422.
14. F. Vigier, C. Coutanceau, F. Hahn, E. M. Belgsir and C. Lamy, *J. Electroanal. Chem.*, 2004, **563**, 81-89.
15. A. Lagutchev, G. Q. Lu, T. Takeshita, D. D. Dlott and A. Wieckowski, *J. Chem. Phys.*, 2006, **125**, 10.
16. F. T. Vidal, A., *Rep. Prog. Phys*, 2005, **68**, 33.
17. Y. R. Shen, *Nature*, 1989, **337**, 7.
18. H. W. K. Tom, C. M. Mate, X. D. Zhu, J. E. Cromwell, T. F. Heinz, G. A. Somorjai and Y. R. Shen, *Phys. Rev. Lett*, 1984, **52**.
19. X. D. Zhu, W. Daum, X.-D. Xiao, R. Chin and Y. R. Shen, *Phys. Rev. B*, 1991, **43**.
20. W. Akemann, K. A. Friedrich and U. Stimming, *J. Chem. Phys.*, 2000, **113**.
21. H. S. Lagutchev A, Dlott D, *J. Phys. Chem. C*, 2007, **111**, 3.
22. A. Lagutchev, A. Lozano, P. Mukherjee, S. A. Hambir and D. D. Dlott, *Spectrochim. Acta A*, 2010, **75**, 1289-1296.
23. G. Q. Lu, A. Lagutchev, D. D. Dlott and A. Wieckowski, *Surf. Sci.*, 2005, **585**, 3-16.
24. X. H. Xia, H.-D. Liess and T. Iwasita, *J. Electroanal. Chem.*, 1997, **437**, 233-240.
25. E. Herrero, J. M. Feliu, A. Wieckowski and J. Clavilier, *Surf. Sci.*, 1995, **325**, 131-138.
26. B. Braunschweig and W. Daum, *Langmuir*, 2009, **25**, 11112-11120.

27. R. Subbaraman, D. Strmcnik, V. Stamenkovic and N. M. Markovic, *J Phys. Chem. C*, 2010, **114**, 8414-8422.
28. A. Kolics and A. Wieckowski, *The Journal of Physical Chemistry B*, 2001, **105**, 2588-2595.
29. M. Ito, *Surf. Sci. Rep.*, 2008, **63**, 329-389.
30. A. Lachenwitzer, N. Li and J. Lipkowski, *J. Electroanal. Chem.*, 2002, **532**, 85-98.
31. F. C. Nart, T. Iwasita and M. Weber, *Electrochim. Acta*, 1994, **39**.
32. B. Braunschweig, P. Mukherjee, D. D. Dlott and A. Wieckowski, *J. Am. Chem. Soc.*, 2010, **132**.
33. B. Bittinscattaneo, S. Wilhelm, E. Cattaneo, H. W. Buschmann and W. Vielstich, *Ber. Bunsen-Ges. Phys. Chem. Chem. Phys.*, 1988, **92**, 1210-1218.
34. T. Iwasita and E. Pastor, *Electrochim. Acta*, 1994, **39**, 531-537.
35. M. W. Severson, C. Stuhlmann, I. Villegas and M. J. Weaver, *J Chem Phys*, 1995, **103**, 12.
36. I. Villegas and M. J. Weaver, *J Chem Phys*, 1994, **101**.
37. B. N. J. Persson, M. Tushaus and A. M. Bradshaw, *J. Chem. Phys.*, 1990, **92**.
38. J. Souza-Garcia, E. Herrero and J. M. Feliu, *Chem. Phys. Chem.*, 2010, **11**.
39. H. Hitmi, E. M. Belgsir, J. M. Leger, C. Lamy and R. O. Lezna, *Electrochim. Acta*, 1994, **39**, 407-415.
40. C. Lamy, *Electrochim. Acta*, 1984, **29**.
41. I. T. Bae, *J. Phys. Chem*, 1996, **100**.
42. G. A. Camara and T. Iwasita, *J. Electroanal. Chem.*, 2005, **578**, 315-321.
43. K. D. Snell and A. G. Keenan, *Electrochimica Acta*, 1982, **27**, 1683-1696.
44. S. C. S. Lai, S. E. F. Kleijn, F. T. Z. Öztürk, V. C. van Rees Vellinga, J. Koning, P. Rodriguez and M. T. M. Koper, *Catalysis Today*, 2010, **154**, 92-104.
45. G. Q. Lu, Crown, Alecia, and Wieckowski, Andrzej, *J Phys Chem B.*, 1999, **103**, 12.
46. H. E. Gamboa-Aldeco M, Zelenay P, Wieckowski A, *J. Electroanal. Chem.*, 1992, **348**, 6.
47. G. Horanyi and A. Wieckowski, *J. Electroanal. Chem.*, 1990, **294**, 267-274.
48. J. J. Max and C. Chapados, *J. Chem. Phys.*, 2009, **131**.

2.8 Figures

Molecular Species	Γ_q (cm^{-1})	ω_q (cm^{-1})
^{12}CO (atop)	28	2080-2100
^{12}CO (bridge)	40	1850
^{13}CO (atop)	30	2030
acetate ($HClO_4$)	50	1410
acetate (H_2SO_4)	29	1410
acetate ($^{12}CH_3{}^{13}CH_2OH$)	25	1350
(bi)sulfate	41	1280

Table 2.1: Frequencies ω_q and bandwidths Γ_q of vibrational bands used to identify adsorbates. References for these assignments are provided in the text.

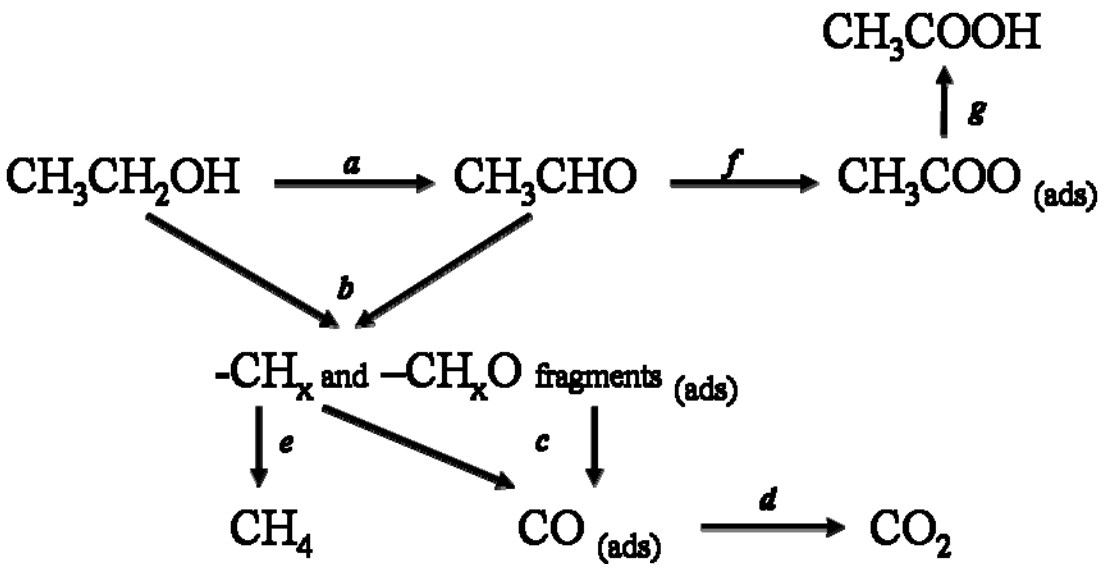

Scheme 2.1: Proposed reaction pathways for the electrooxidation of ethanol on a platinum surface in acidic electrolytes. Each pathway is discussed in detail in the text.

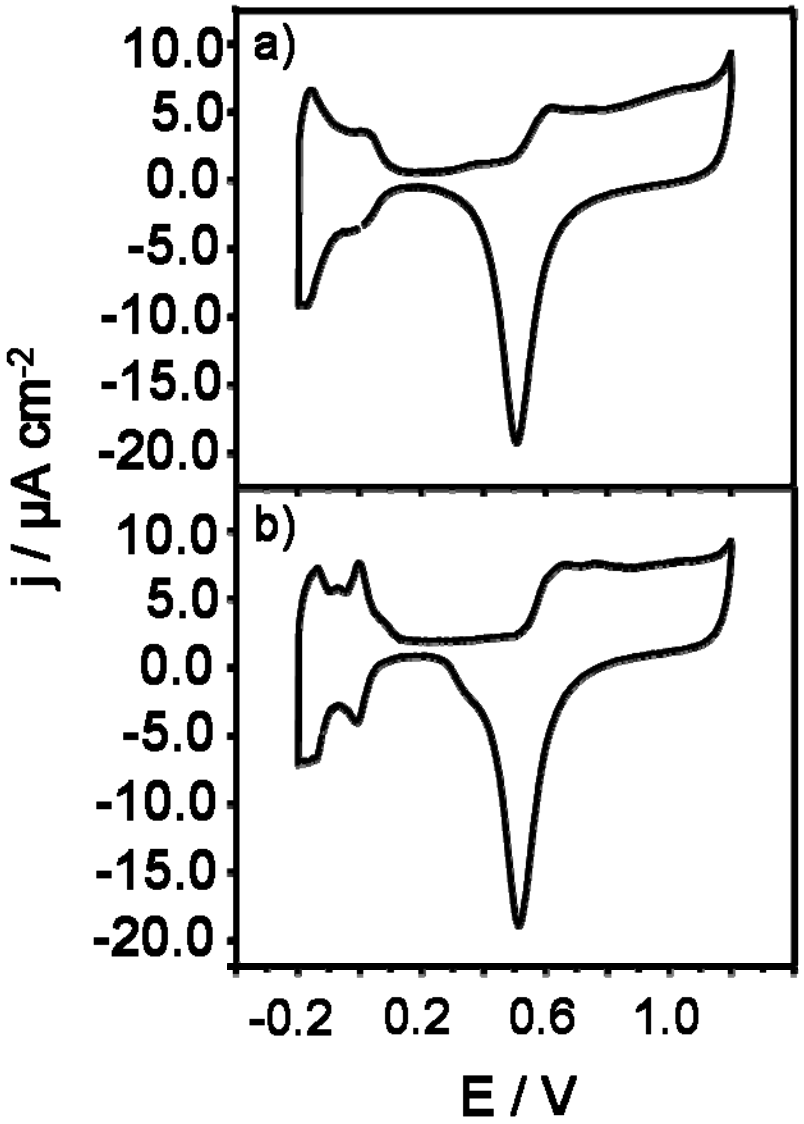

Figure 2.1. Hanging-meniscus cyclic voltammograms (CVs) of a polycrystalline platinum disk in a) 0.1 M $HClO_4$ and b) 0.1 M H_2SO_4. The CVs were recorded with a sweep rate of 5 mV/s.

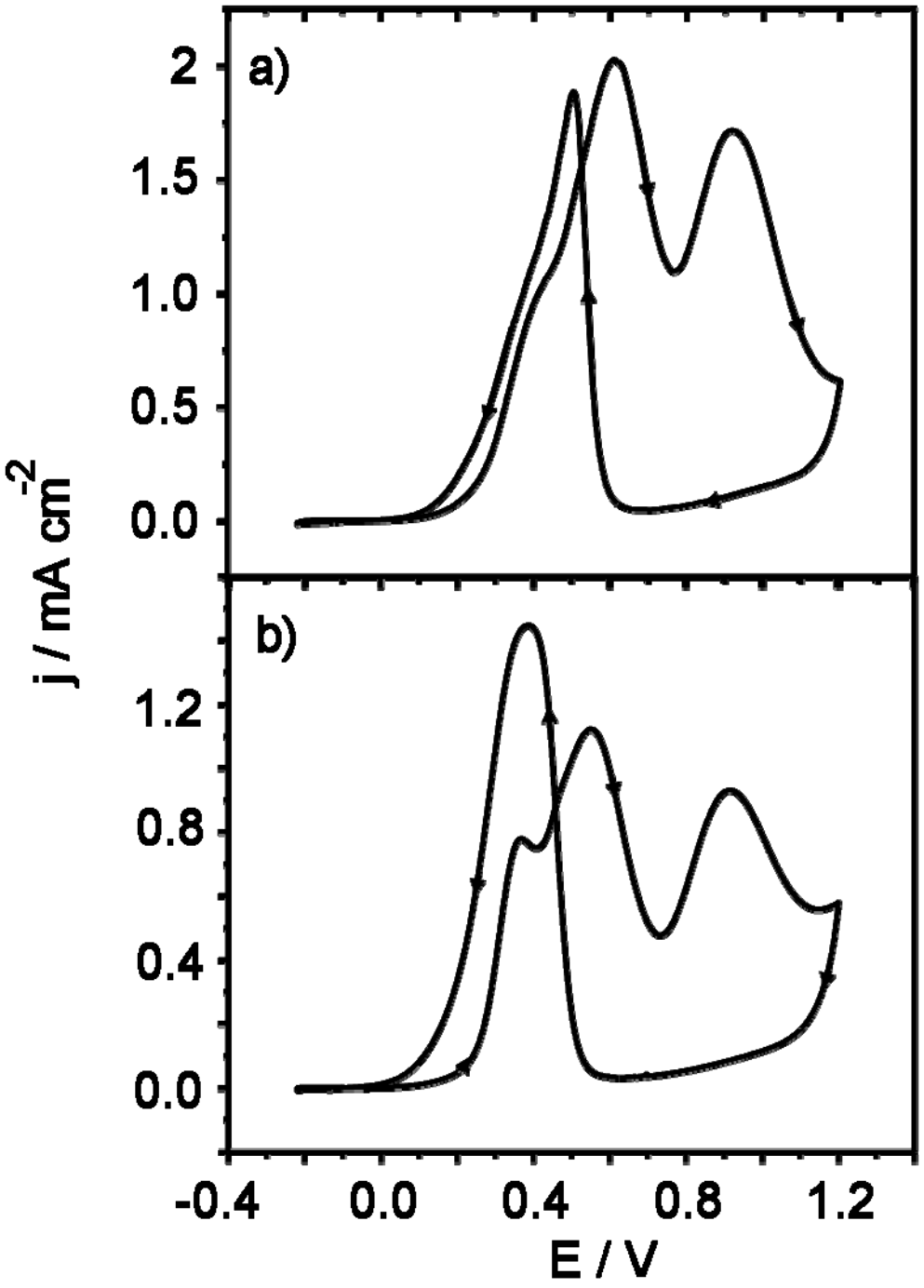

Figure 2.2: Hanging-meniscus cyclic voltammograms (CVs) of a polycrystalline platinum disk in 0.5 M ethanol with a) 0.1 M $HClO_4$ and b) 0.1 M H_2SO_4. The CVs were recorded with a sweep rate of 5 mV/s.

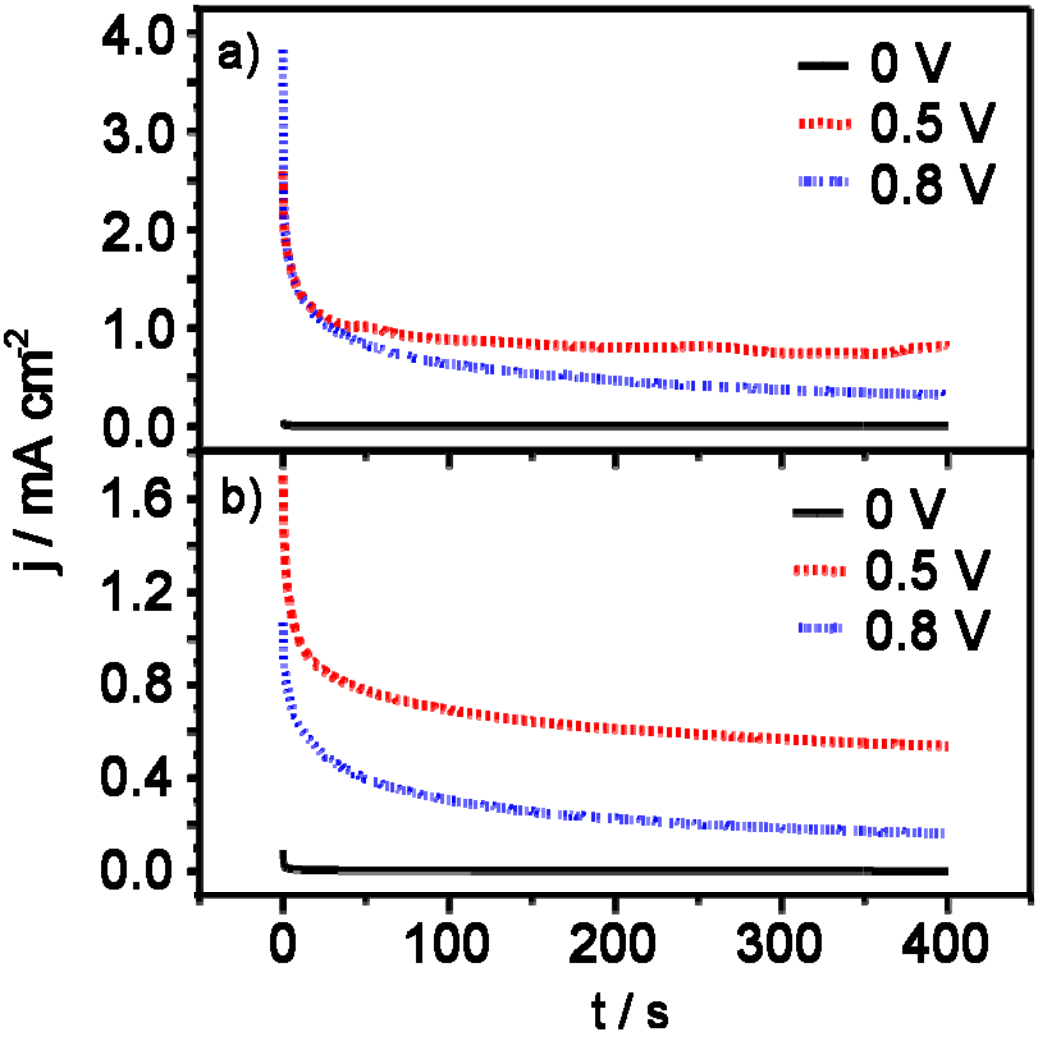

Figure 2.3: Chronoamperograms of a polycrystalline Pt disk in solutions of a) 0.1 M $HClO_4$ and b) 0.1 M H_2SO_4 each with 0.5 M ethanol. Potentials were stepped from open-circuit conditions to the potentials indicated in the figure.

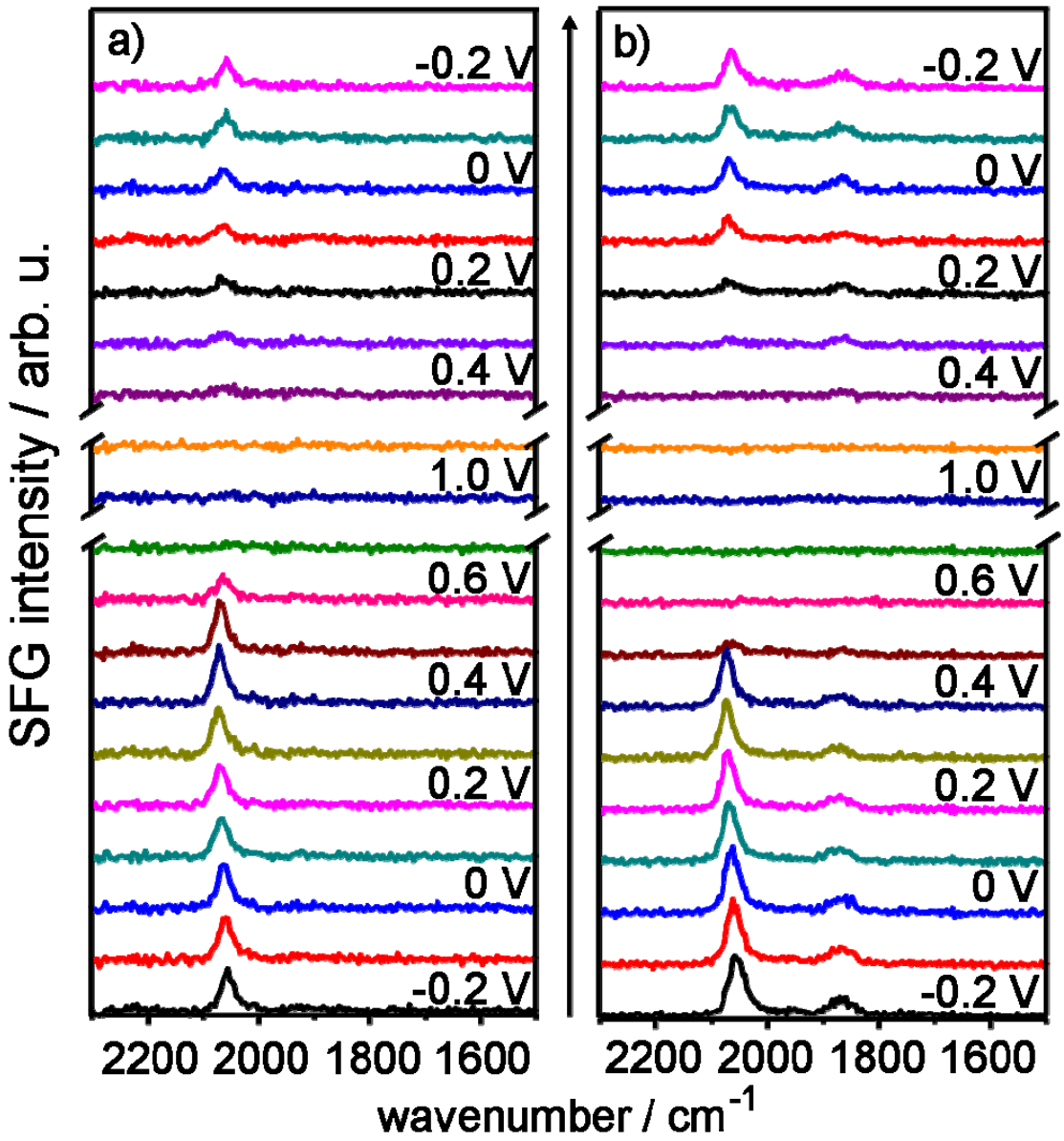

Figure 2.4: Consecutive series of potentiodynamic SFG spectra of atop and bridge-bonded CO vibrational bands recorded during 0.5 M ethanol ($^{12}CH_3{}^{12}CH_2OH$) electrooxidation on a polycrystalline Pt electrode in a) 0.1 M $HClO_4$ and b) 0.1 M H_2SO_4. Electrode potentials *E* / V were as indicated in the figure. The frequency Ω of the BBIR pulse was centered at 1961 cm^{-1}.

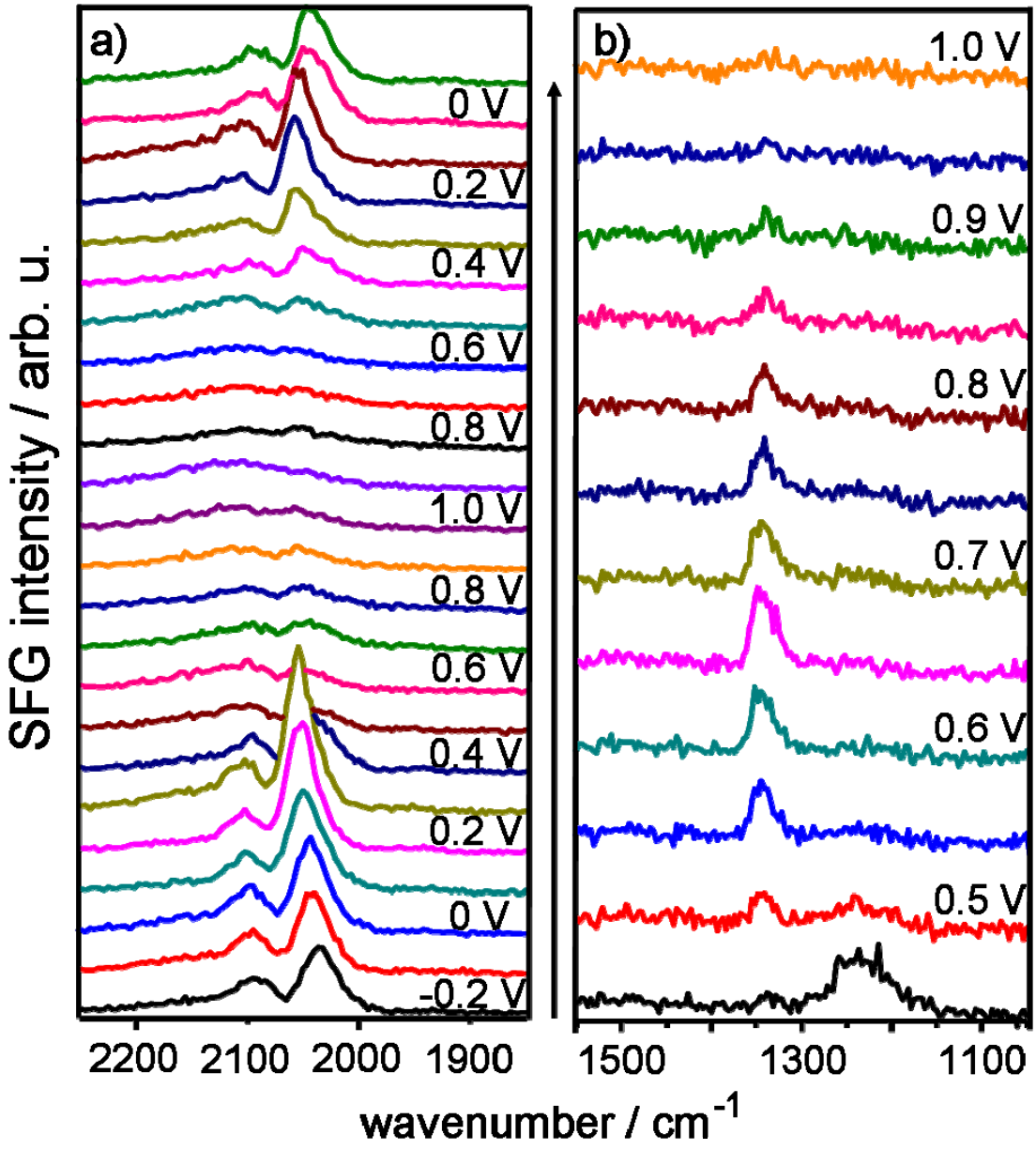

Figure 2.5: Consecutive series of potentiodynamic SFG spectra of a) $^{12}CO/^{13}CO$ and b) symmetric carboxylate ($-^{13}COO^-$) stretching vibrations. SFG spectra were recorded during electrooxidation of 0.2 M isotopically-labeled ethanol ($^{12}CH_3{}^{13}CH_2OH$) on a polycrystalline Pt electrode in 0.1 M $HClO_4$. Electrode potentials *E* / V are indicated in the figure. The frequency Ω of the BBIR pulse was centered at a) 2174 cm^{-1} and b) 1408 cm^{-1}.

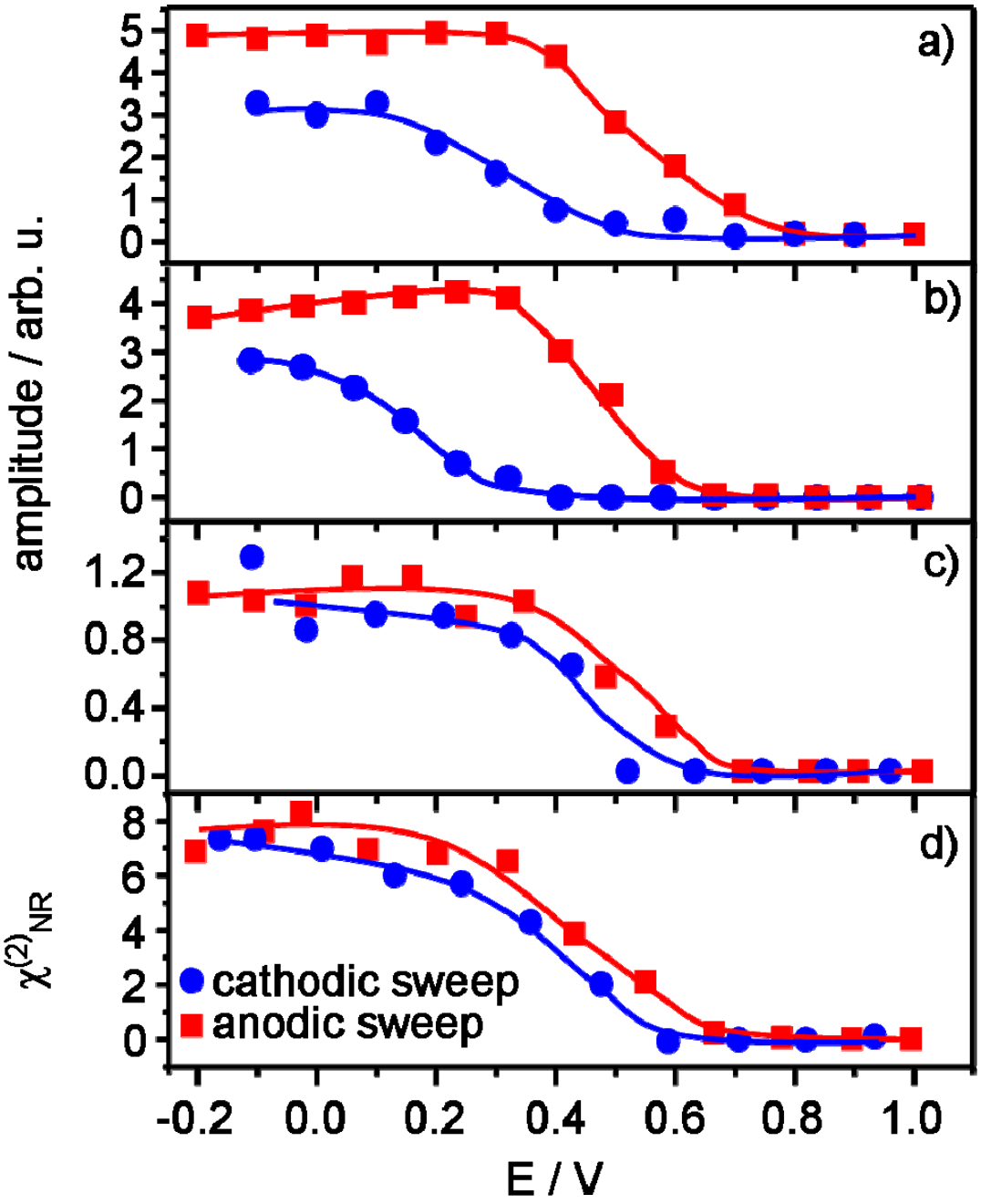

Figure 2.6: a) and b) potential dependence of modeled SFG amplitudes for atop CO atop vibrational bands (~2080 cm^{-1}) in Fig. 4 during electrooxidation of 0.5 ethanol on polycrystalline Pt in 0.1 M $HClO_4$ and 0.1 M H_2SO_4, respectively. c) SFG amplitude of vibrational bands in Fig. 4b corresponding to bridge-bonded CO (1850 cm^{-1}) during ethanol oxidation on Pt in 0.1 M H_2SO_4. d) Potential dependence of the non-resonant contribution $\chi^{(2)}_{NR}$ in Fig. 8 (1300 cm^{-1}). Curves are a guide to the eye.

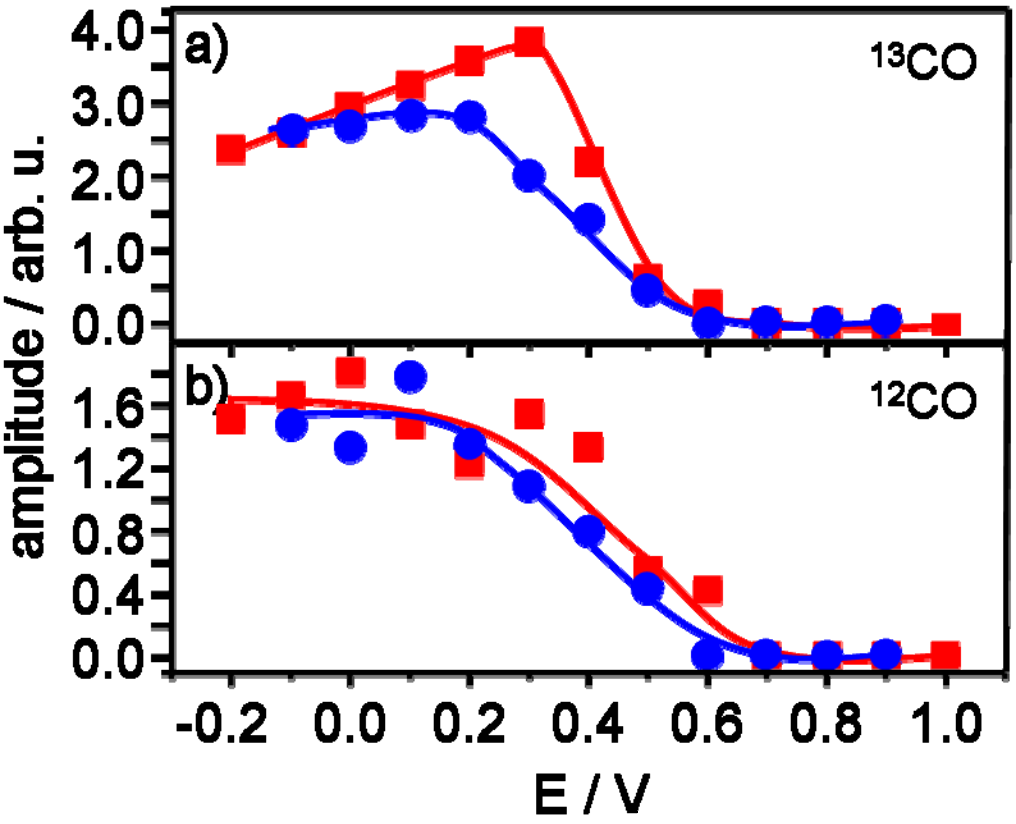

Figure 2.7: Potential dependence of modeled SFG amplitudes of a) ^{13}CO and b) ^{12}CO vibrational bands in Fig. 5 during electroxidation of 0.5 M isotopically-labeled ethanol ($^{12}CH_3{}^{13}CH_2OH$) on polycrystalline Pt in 0.1 M $HClO_4$. Curves are a guide to the eye.

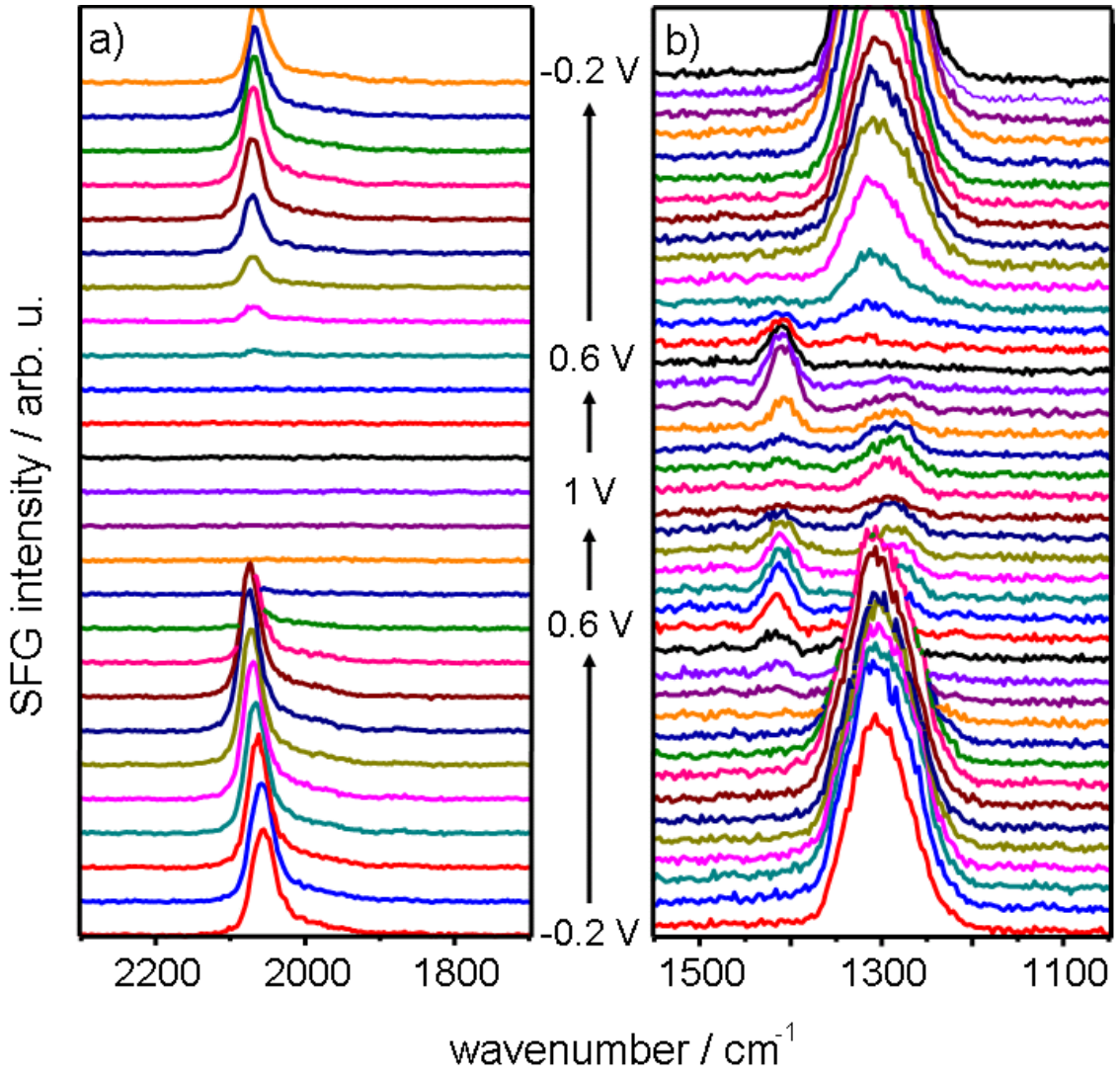

Figure 2.8: Consecutive series of potentiodynamic SFG spectra recorded during 0.5 M ethanol ($^{12}CH_3{}^{12}CH_2OH$) electrooxidation on a polycrystalline Pt electrode in 0.1 M H_2SO_4. Spectra in a) show vibrational bands of ^{12}CO adsorbed on atop Pt sites, while spectra in b) reveal (bi)sulfate and adsorbed acetate vibrational bands as well as $\chi_{NR}^{(2)}$ contributions. Electrode potentials *E* / V are indicated in the figure. The frequency Ω of the BBIR pulse was centered at a) 2083 cm^{-1} and b) 1428 cm^{-1}.

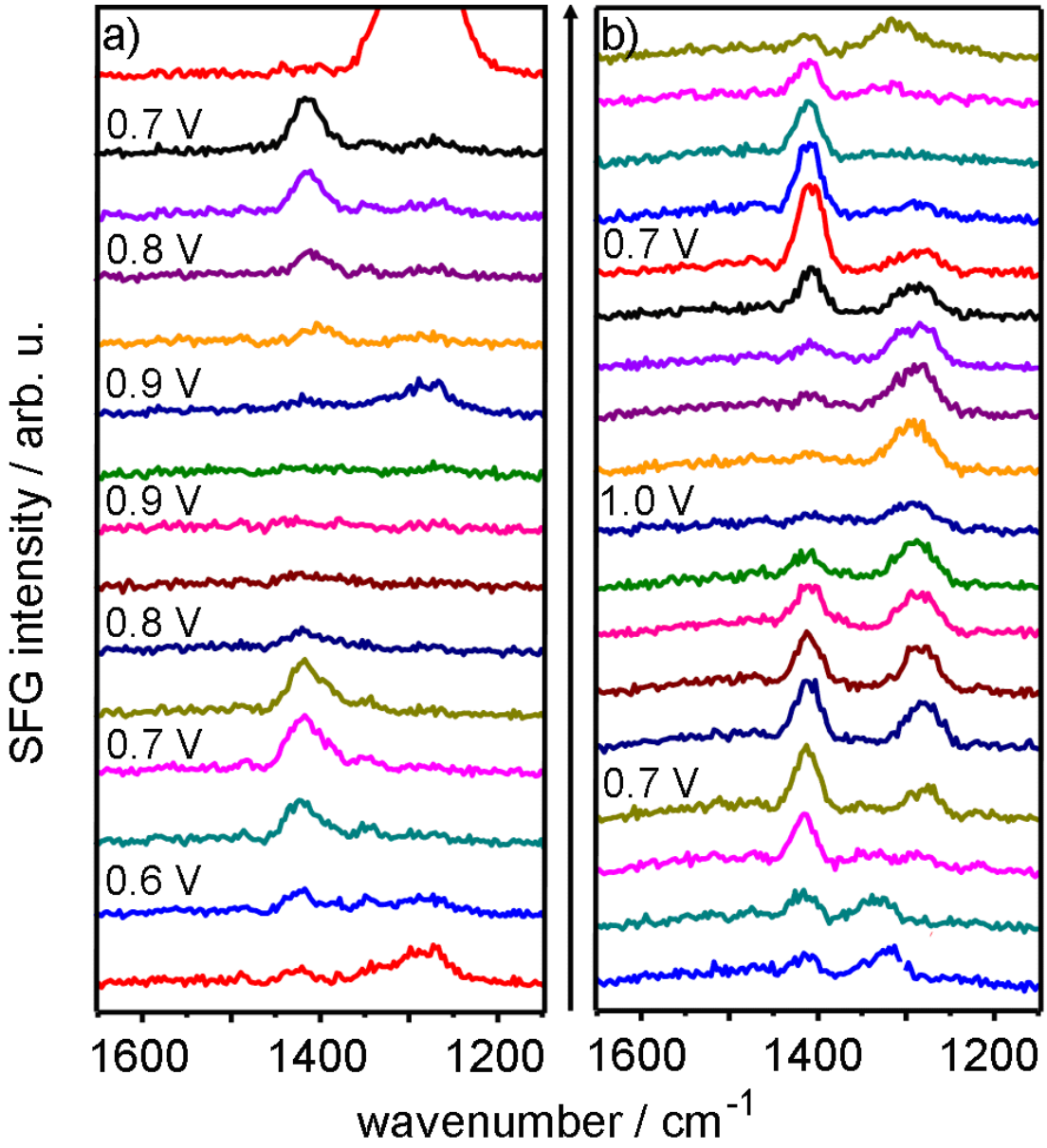

Figure 2.9: Consecutive series of potentiodynamic SFG spectra of adsorbed acetate (1410 cm^{-1}) and co-adsorbed (bi)sulfate (1280 cm^{-1}) vibrational bands. Spectra were recorded during 0.5 M ethanol ($^{12}CH_3{}^{12}CH_2OH$) electrooxidation on a polycrystalline Pt electrode in a) 0.1 M $HClO_4$ and b) 0.1 M H_2SO_4. Electrode potentials *E* / V are indicated in the figure. The frequency Ω of the BBIR pulse was centered at 1429 cm^{-1}.

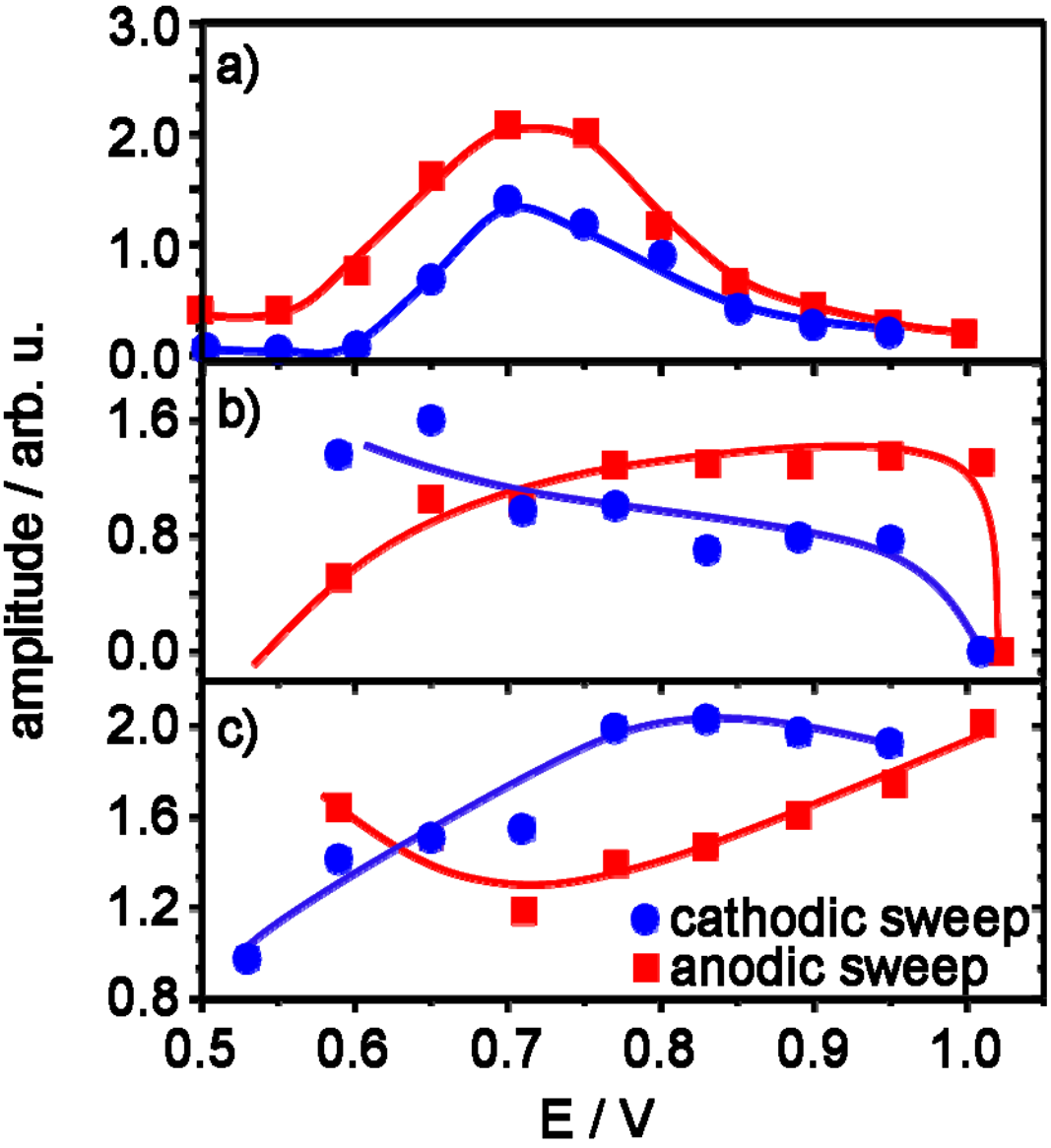

Figure 2.10: a) and b) SFG modeled amplitudes of acetate vibrational bands (1410 cm^{-1}) in Fig. 9 during electrooxidation of 0.5 M ethanol ($^{12}CH_3{}^{12}CH_2OH$) on polycrystalline Pt in 0.1 M $HClO_4$ and 0.1 M H_2SO_4, respectively. c) SFG amplitude of vibrational bands (1280 cm^{-1}) due to co-adsorbed sulfuric acid anions during ethanol oxidation in 0.1 M H_2SO_4. Curves are a guide to the eye.

CHAPTER 3

ETHANOL OXIDATION ON PLATINUM CATALYSTS IN ALKALINE ELECTROLYTES

3.1 Notes and Acknowledgements

This chapter is adapted from a manuscript that I authored called "Study of Ethanol Electrooxidation in Alkaline Electrolytes with Isotope Labels and Sum-Frequency Generation.[b]" It was published in the Journal of Physical Chemistry Letters in 2011 and is reproduced here with permission. In a sense, it's a continuation of studies presented in the prior chapter. In alkaline electrolytes, no larger two-carbon intermediate chemical moieties such as acetate were observed bound to the catalyst surface. In a sense, this, as well as the lower overpotential for CO oxidation, are considered notable advantages of alkaline conditions for liquid fuel cells. However, this manuscript does investigate CO formation in greater detail, and attempts to shift emphasis from merely oxidizing CO to recognizing the persistence of adsorbed $-CH_x$ fragments.

I'd like to acknowledge several people for their assistance with this manuscript, including Drs. Björn Braunschweig, Prabuddha Mukherjee, Dana D. Dlott, and Andrzej Wieckowski. Their assistance and conversations during the course of this work are still very much appreciated. Research described in this study was supported by the US Army

[b] Kutz, R. B.; Braunschweig, B.; Mukherjee, P.; Dlott, D. D.; Wieckowski, A. "Study of Ethanol Electrooxidation in Alkaline Electrolytes with Isotope Labels and Sum-Frequency Generation." J. Phys. Chem. Lett. 2011. 2, 2236.

Research Office under award W911NF-08-10309 as well as from the US Air Force Office of Scientific Research under award: FA9550-09-1-0163.

3.2 Introduction

Ethanol has become globally recognized as an important source of energy because it is abundant, has a high molecular energy density, and is easily produced from plant matter[1]. The majority of the ethanol produced in most industrial nations is used as a fuel additive for combustion engines as a means to reduce the dependency on foreign oil. However, using ethanol as a fuel in combustion engines is both inefficient and limited. Fuel blends with high ethanol content can pose public health risks[2], and the thermodynamic losses inherent to combustion engines remain an issue. Ethanol fuel cells[3-6] are ideally capable of bypassing these thermodynamic losses by converting chemical energy directly to electrical energy. Furthermore, both ethanol and fuel cells are clean and compactable, expanding the potential of ethanol fuel to power a wider variety of devices including portable electronics. Despite these advantages, the design of efficient ethanol fuel cell catalysts has proven to be highly challenging. It is clear from previous studies[7-9] that the full potential of ethanol for fuel cells cannot be realized unless active catalyst surface sites for C—C bond splitting as well as CO and —CH_x removal are simultaneously present and reaction conditions are optimized to promote higher selectivity towards CO_2 formation. For this reason, studies on the ethanol oxidation reaction (EOR) have been extensive[10-18], but they were primarily performed in acidic electrolytes. Alkaline electrolytes offer many advantages, however, particularly

since electrocatalytic activity toward ethanol oxidation is much greater in alkaline than in acidic media[19]. Furthermore, recent improvements on alkaline fuel cell designs include more robust membranes with reduced carbonation effects[20], and improvements upon membranes resistant to carbonate precipitation bring them closer to performing as efficiently as traditional proton exchange membranes[21]. Thus, understanding and enhancing EOR catalysis in alkaline media is becoming increasingly pertinent.

For this reason, we have used broadband sum-frequency generation (BB-SFG) vibrational spectroscopy to study the ethanol electrooxidation reaction on a polycrystalline Pt surface in alkaline media. Polycrystalline Pt catalysts provide a good model system for studies of ethanol electrooxidation in alkaline media because they are widely known as highly active but inefficient catalysts for EOR [22,23]. In order to establish the necessary characteristics of more efficient catalysts, we are interested in a molecular-level understanding of the EOR that reveals all possible steps that could decrease the overall efficiency. SFG, as an inherently surface-specific technique, provides a direct observation of only those molecular species that are adsorbed to the catalyst surface without spectral interference from the bulk electrolyte. The use of a Teflon spacer creates a fixed 25 μm gap between the optical window and Pt electrode, permitting the synchronous application of voltammetric sweeps at rates of < 5 mV/s without detrimental ohmic drop. Our data thus offer insights into the chemical identity of surface-adsorbed intermediates. We report new information on the mechanism of ethanol decomposition and CO formation in alkaline solution using isotopically-labeled

ethanol and clarify the behavior of adsorbed single-carbon intermediates that point to the presence of strongly adsorbed $-CH_x$ species in alkaline media.

3.3 Experimental

A polished polycrystalline platinum disk (Matek) with a 6 mm diameter was used as the working electrode in each SFG and electrochemical experiment. The counter electrode was a flame-annealed platinum wire (99.99%) and a the reference electrode was a commercial Ag/AgCl (BASi; MF-2052; -0.25 vs. RHE) electrode. However, all potentials throughout this article are reported with respect to a reversible hydrogen electrode (RHE). Voltammetric experiments were carried out using a Princeton Applied Research (PAR 263A) potentiostat. Solutions were prepared using NaOH (99.99%, Sigma-Aldrich), ethanol (CH_3CH_2OH, 99.5%), and isotopically-labeled ethanol ($^{12}CH_3{}^{13}CH_2OH$, >99%, Sigma-Aldrich). All dilutions were performed using ultra-pure water ($\geq$18.2 MΩ, total oxidizable carbon $\leq$ 4ppb) obtained from a Millipore Gradient A10 purification system and all solutions were thoroughly purged with Ar gas (ultra-high purity). Prior to each experiment, the Pt disk was soaked in concentrated sulfuric acid, rinsed with ultrapure water, and electrochemically cleaned by potential cycling between 0 and 1.3 V for >50 cycles at a sweep rate of 200 mV/s.

Our BB-SFG apparatus, which has been described elsewhere[1,2], permits the rapid acquisition of vibrational spectra synchronized with a voltammetric sweep. Tunable broadband infrared (BBIR) pulses were generated in an optical parametric amplifier

(Light Conversion; Topas) that was pumped by a femtosecond Ti:Sapphire laser system (Quantronix; Integra C series) at a repetition rate of 1 kHz. The BBIR pulses had typical pulse durations of ~120 fs, typical bandwidths of Δ >150 cm^{-1} and pulse energies of approximately 8 μJ at a frequency Ω of 2083 cm^{-1}. Narrow-band visible pulses with 5 μJ pulse energy and a fixed wavelength of 800 nm were generated by narrowing the fs pulses to a bandwidth of <10 cm^{-1} with a Fabry-Pérot etalon. Narrow-band visible and BBIR pulses were overlapped in time and space at an incident angle of ~60º to the normal of the Pt-electrolyte interface. Sum-frequency photons were collected with a spectrograph and a charge-coupled device (CCD). The SFG, visible, and IR photons were all p-polarized. Spectro-electrochemical experiments were carried out in a previously described electrochemical cell[2] for synchronized SFG and electrochemical experiments. In this electrochemical cell, a well-defined gap of 25 μm between the electrode surface and a CaF_2 optical window is established by a Teflon spacer of the same thickness. The 25 μm electrolyte gap allows for voltammetric scans at sweep rates of ≤ 5 mV/s without the detriment of strong ohmic drop effects that are associated with thin-layer electrochemistry [2].

The following equation describes the model used for the intensity $I(\omega_{SF})$ of the SFG signals and its dependent parameters:

$$I(\omega_{SF}) \propto \left| \chi_{NR}^{(2)} + \sum_q \frac{A_q \cdot e^{-i\theta_q}}{(\omega_{IR} - \omega_q) + i\Gamma_q} \right|^2 \cdot I(\omega_{vis}) I(\omega_{IR}) \exp\left[-4 \ln 2 \frac{(\omega - \Omega)^2}{\Delta^2} \right] \quad (3.1)$$

Here, Ω and Δ refer to the frequency and bandwidth of the impinging BBIR pulse, while A_q, θ_q, ω_q, and Γ_q are amplitude, relative phase, frequency, and homogenous linewidth

of the q-th vibrational mode, respectively. $\chi_{NR}^{(2)}$ is the non-resonant component of the interfacial second-order nonlinear susceptibility $\chi^{(2)}$. $\chi_{NR}^{(2)}$ is nearly independent of the BBIR frequency Ω and manifests as a featureless SFG contribution produced by the surface, but is highly dependent on the electronic structure of the surface [3]. Because we are mostly interested in resonant contributions of $\chi^{(2)}$ which are associated with adsorbed molecular species, we have applied a $\chi_{NR}^{(2)}$ suppression technique previously reported by Lagutchev et al.[1,4] This technique, however, requires a compromise between a complete suppression of $\chi_{NR}^{(2)}$ and maintaining a relatively good signal-to-noise ratio of the observed vibrational bands.

3.4 Results

Fig. 3.1 a) and b) present cyclic voltammograms (CVs) of polycrystalline platinum in a solution of a) blank 0.1 M NaOH and b) 0.1 M NaOH with 0.5 M ethanol. These CVs were recorded in a hanging-meniscus configuration and with a sweep rate of 50 mV/s. The CV in Fig 3.1a shows features between 0.05 and 0.45 V that are characteristic for hydrogen underpotential deposition/desorption on a clean polycrystalline Pt surface. The formation of surface oxides on the anodic sweep starts at ~0.45 V, while on the cathodic sweep the reduction of the previously formed oxides gives rise to a negative feature centered at ~0.7 V. The CV in Fig. 3.1b is characteristic of ethanol oxidation in alkaline media. The onset of the current feature centered between 0.4 and 0.85 V on

the anodic potential sweep coincides with the oxidation of surface-adsorbed CO (Fig. 3.2), which is preceded by the cleavage of ethanol's C—C bonds. The current density *j* decreases but remains above zero for the remainder of the anodic sweep, which implies some activity for oxidation of reaction intermediates at these potentials. The maximum in current density on the cathodic sweep is centered at ~0.6 V and coincides with the reductive stripping of Pt surface oxides.

In order to correlate the voltammetry with the formation and removal of specific intermediates of ethanol electrooxidation, consecutive SFG spectra were recorded in CO-saturated 0.1 M NaOH (Fig 3.2a) and in 0.1 M NaOH with 0.5 M ethanol (Fig. 3.2b). In both solutions, a vibrational band centered at 2030 cm^{-1} dominates the SFG spectra and can be assigned to stretching vibrations of CO molecules adsorbed on Pt atop sites[24]. For potentials > 0.35 V the amplitude of the CO band for both CO-saturated and ethanol containing electrolytes (Fig. 3.2) decreases with increasing surface oxide concentration (Fig. 3.1a). However, a substantial recovery of the CO band at more anodic potentials between 0.75 and 1.25 V is observed in ethanol-containing solution (Fig. 3.2b). We investigated this surprising potentiodynamic behavior of the CO intermediate in greater detail with a similar study using 0.5 M isotopically-labeled ethanol ($^{12}CH_3{}^{13}CH_2OH$). Fig. 3.2c presents the same spectral region for an experiment where isotopically-labeled ethanol is oxidized. Consistent with previous experiments with regular ethanol, oxidation of isotopically-labeled ethanol leads to an identical decrease and sudden increase of the CO band at higher potentials: At 0.05 V, a band at 1995 cm^{-1} attributable to ^{13}CO is observed, increases in intensity with increasing

potential and begins to diminish at 0.35 V. However, an apparent abrupt blue-shift of CO stretching frequencies to ~2030 cm^{-1} takes place, while the SFG intensity near 1995 cm^{-1} rapidly diminishes (Fig. 3.2c). It is very unlikely that potential-induced Stark tuning would be responsible for such an abrupt and dramatic frequency shift, as our further analysis demonstrates. Consequently, the band at 0.75 V must be composed of two bands at ~2030 cm^{-1} and ~1995 cm^{-1} that are attributable to ^{12}CO and ^{13}CO species, respectively. This conclusion is further substantiated by our SFG spectra at 0.85 V, where the ^{12}CO signal has clearly resolved into a band at 2030 cm^{-1}, and the ^{13}CO signal at 1995 cm^{-1} has fully diminished in amplitude (Fig. 3.2c).

Spectra were also recorded that observe what appears to be bridge-bound CO at approximately 1770 cm^{-1}, seen in Fig. 3.6. Unlike the waterfall spectra corresponding to atop CO, here the CO amplitude remains rather low and does not oxidize away from the surface until approximately 1.0 V.

In order to obtain a better understanding of the potential dependence of the reported vibrational bands, we have fitted our vibrational spectra with model functions according to eqn. 3.1. The amplitudes A_q of CO atop from regular ethanol and CO atop from isotopically-labeled ethanol are shown as a function of electrode potential in Figs. 3.3a and b respectively. Clearly, at low potentials in Fig. 3.3b, there is no ^{12}CO vibrational band. Surface-bound ^{12}CO species that would give rise to the latter band are formed at potentials >0.75 V only. The frequencies ω_q of the ^{13}CO and ^{12}CO from the oxidation of 0.5 M regular ethanol and 0.5 M isotopically-labeled ethanol are shown as a function of electrode potential in Figs. 3.3c and d respectively.

Spectra were also recorded in lower-concentration solutions of 0.2 M regular ethanol and isotopically labeled ethanol. We present these spectra as well because they more dramatically demonstrate the frequency separation between the ^{13}CO and ^{12}CO vibrational bands. A comparison of spectra modeled according to eqn. (1) is presented in Fig 3.4. Fig 3.4(a) shows CO vibrational bands from 0.2 M regular ethanol at 0.05 V and at 0.95 V. Similarly, Fig 3.4(b) shows CO vibrational bands from 0.2 M isotopically labeled ethanol at 0.05 V, where ^{13}CO dominates the spectrum, and at 0.95 V, where ^{12}CO dominates the spectrum. The more pronounced frequency shift in isotopically-labeled ethanol further emphasizes the hypothesis that these two vibrational bands are indicative of two different single-carbon species on the ethanol molecule.

3.5 Discussion

Complete oxidation of ethanol to CO_2 requires both the splitting of C–C bond and the subsequent oxidative removal of surface-adsorbed carbonaceous fragments. An ideal catalyst with a high selectivity for ethanol oxidation toward CO_2 formation, therefore, requires persistently available active sites that can catalyze both of these processes. Our observation of surface-adsorbed CO molecules at 0.05 V indicates that on a polycrystalline Pt surface, the ethanol molecule's C–C bond breaks at very low potentials and, subsequent to the dissociation of the ethanol molecule, at least one of the resulting single-carbon fragments can be further oxidized to CO. This scission of the C–C bond at low potentials is similarly observed in acidic media[16], but in alkaline media the resulting single-carbon fragments show remarkably different behavior. While in

acidic solutions CO oxidation typically occurs at potentials of ~0.65 V[16], it is observed at much lower potentials of 0.25 to 0.35 V in alkaline electrolytes (Fig. 3.2). Comparing the onsets for CO oxidation in acidic and alkaline electrolytes, we suggest that CO oxidation is more facile in alkaline than in acidic electrolytes as a result of a higher hydroxyl coverage at more cathodic potentials (Fig. 3.1a). Moreover, the presence and the oxidation of CO as a product of ethanol electrooxidation is consistent with the expected behavior in CO-saturated alkaline and acidic solutions reported in this and previous studies[24,25]. CO is, however, also observed at unusually high potentials which are well inside the region of oxide formation on polycrystalline Pt electrodes in blank alkaline electrolytes. In order to address the possible origin of the CO recovery, which appears to belie the relative ease of oxidizing CO in alkaline media, we tracked the oxidation of the different carbon species that are immediate products of ethanol C–C bond cleavage. In particular, subsequent oxidation of the resulting —$^{12}CH_x$ and —$^{13}COH_x$ fragments from isotopically-labeled ethanol ($^{12}CH_3{}^{13}CH_2OH$) results in surface adsorbed ^{12}CO and ^{13}CO.

In previous work[16] on ethanol oxidation in acidic media with isotopic labeling, we have demonstrated that oxidation of partially oxidized –CH_xO fragments occurs more rapidly at lower overpotentials compared to –CH_x fragments which resist further oxidation and persist on the Pt surface as a catalyst poison. It is reasonable to assume the absence of catalytic sites for efficient oxidation of –CH_x on polycrystalline Pt in alkaline electrolytes as well. This conclusion is corroborated by our SFG spectra during electrooxidation of $^{12}CH_3{}^{13}CH_2OH$, where at low potentials the formation of ^{13}CO is observed only, while ^{12}CO bands that can be expected from –$^{12}CH_x$ oxidation are absent.

A complete change of the situation takes place at high anodic potentials where ^{13}CO is absent and ^{12}CO dominates the SFG spectra. A sudden shift at 0.75 V in SFG intensity from the lower-frequency ^{13}CO band to the higher-frequency ^{12}CO band, displayed in Fig. 3.2c and further clarified in Fig. 3.3d, unequivocally demonstrates the oxidative stripping of ^{13}CO from the Pt surface and the simultaneous deposition of ^{12}CO. Further proof that possible bulk oxidation of ethanol does not produce CO vibrational bands at these potentials can be found in the observation that on a reverse potential sweep to 0.05 V, no CO bands were observed in the potential range between 0.85 and 1.25 V (Figure 3.5). Therefore, the observed CO band must originate from the oxidation of previously formed $–CH_x$. At these potentials CO is quickly oxidized to CO_2 and the remaining free adsorption sites are then covered with surface oxides which inhibit further oxidation reactions. At this point it should be noted that our results are in agreement with a voltammetric study by Lai and Koper [4], where the presence of stable $–CH_x$ intermediates on Pt(111) terrace sites in alkaline media is suggested. On polycrystalline Pt electrodes there is an abundance of (111) surface sites and, consequently, strongly adsorbed and stable $–CH_x$ species can exist on (111) sites of the polycrystalline Pt electrode as well. Bayer et. al also document a single-carbon species that can be reduced to methane at potentials below 0.2 V[26]. However, so far direct and persuasive spectroscopic evidence of such a species in alkaline media has eluded the community[7]. Furthermore, our results provide evidence that an anodic potential sweep to potentials of >0.65 V yields oxidation of $–CH_x$. Here, the supporting electrolyte may

play a crucial role and act as a co-catalyst that lowers the overpotential for the latter reaction.

In acidic media, the $–CH_x$ intermediate is oxidized to ^{12}CO even at potentials as low as 0.05 V, albeit only in relatively very small quantities[16,27]. We do not observe the same ^{12}CO peak at low potentials in alkaline media. This could be due to a much weaker intensity of the CO vibrational band in alkaline media. However, Severson et. al demonstrated that molecular dipole-dipole coupling between adsorbed ^{12}CO and ^{13}CO molecules dramatically shifts vibrational band intensity from the ^{13}CO to the ^{12}CO vibrational band[28]. Thus, if ^{12}CO is present on the surface at low potentials in alkaline media, it must be in very small quantities indeed for us to be unable to observe it. For high anodic potentials where ^{12}CO dominates the spectra, the possible presence of ^{13}CO adsorbed to atop sites cannot entirely be ruled out, but is extremely unlikely as we do not observe this band during the cathodic sweep.

The observation of CO bound to bridge sites within a much wider potential range than for atop sites is likely indicative of some steady-state production of CO past the atop oxidation point observed in Fig 3.2. This could be due to the bulk oxidation of ethanol as well as to the steady but slow formation of CO from surface-bound CH_x species. It is not entirely surprising that we would see CO formed by slow steady-state production on bridge sites but not atop sites, because, as mentioned in chapter 2, CO tends to bind preferentially to bridge sites when in low surface concentration. Unfortunately, isotopic analysis of this band did not provide further insights into its origins.

3.6 Conclusions

In conclusion, we have presented the first BB-SFG study of ethanol electrooxidation in alkaline media that permits new insights into the behavior of single-carbon species as a result of carbon-carbon bond splitting on the Pt electrode. In addition to the low overpotential for CO oxidation at ~0.35 V, we observed a recovery of the CO vibrational band at unusually high anodic potentials of 0.75 to 1.15 V. This hitherto unexpected behavior was investigated in detail with isotopically-labeled ethanol and points to the presence of strongly adsorbed single-carbon species such as $–CH_x$ which resist oxidation for potentials <0.75 V. Our results clearly demonstrate that the advantage of alkaline media – an oxidative removal of surface-bound CO at much lower overpotentials – is thus impaired by the persistence of strongly adsorbed $–CH_x$ species which block adsorption sites for the ethanol fuel and lead to a decrease in overall efficiency. It is now quite clear that the surface composition of more efficient catalysts will require active surface sites for C–C bond breaking and CO removal as well as an increased selectivity for CO_2 formation. However, the highest efficiencies can be achieved only if these surface sites are accompanied by active sites that also remove strongly bound $–CH_x$ species from the surface.

3.7 References

(1) Lynd, L. R.; Cruz, C. H. D. B. Make Way for Ethanol. *Science* **2010**, *330*, 1176-1177.

(2) Jacobson, M. Z. Effects of Ethanol (E85) versus Gasoline Vehicles on Cancer and Mortality in the United States. *Environ. Sci. Technol.* **2007**, *41*, 4150-4157.

(3) Heinen, M.; Jusys, Z.; Behm, R. J. Ethanol, Acetaldehyde and Acetic Acid Adsorption/Electrooxidation on a Pt Thin Film Electrode under Continuous Electrolyte Flow: An in Situ ATR-FTIRS Flow Cell Study. *J. Phys. Chem. C* **2010**, *114*, 9850-9864.

(4) Koper, M. T. M.; Lai, S. C. S. Ethanol electro-oxidation on platinum in alkaline media. *Phys. Chem. Chem. Phys.* **2009**, *11*, 10446-10456.

(5) Giz, M. J.; Camara, G. A. The ethanol electrooxidation reaction at Pt (111): The effect of ethanol concentration. *J. Electroanal. Chem.* **2009**, *625*, 117-122.

(6) Lai, S. C. S.; Koper, M. T. M. Electro-oxidation of ethanol and acetaldehyde on platinum single-crystal electrodes. *Faraday Discuss.* **2008**, *140*, 399-416.

(7) Lai, S. C. S.; Kleyn, S. E. F.; Rosca, V.; Koper, M. T. M. Mechanism of the Dissociation and Electrooxidation of Ethanol and Acetaldehyde on Platinum As Studied by SERS. *J. Phys. Chem. C* **2008**, *112*, 19080-19087.

(8) Gomes, J. F.; Busson, B.; Tadjeddine, A.; Tremiliosi-Filho, G. Ethanol electro-oxidation over Pt(h k l): Comparative study on the reaction intermediates probed by FTIR and SFG spectroscopies. *Electrochim. Acta* **2008**, *53*, 6899-6905.

(9) Vigier, F.; Rousseau, S.; Coutanceau, C.; Leger, J. M.; Lamy, C. Electrocatalysis for the direct alcohol fuel cell. *Top. Catal.* **2006**, *40*, 111-121.

(10) Camara, G. A.; Iwasita, T. Parallel pathways of ethanol oxidation: The effect of ethanol concentration. *J. Electroanal. Chem.* **2005**, *578*, 315-321.

(11) de Souza, J. P. I.; Queiroz, S. L.; Bergamaski, K.; Gonzalez, E. R.; Nart, F. C. Electro-oxidation of ethanol on Pt, Rh, and PtRh electrodes. A study using DEMS and in-situ FTIR techniques. *J. Phys. Chem. B* **2002**, *106*, 9825-9830.

(12) Tarnowski, D. J.; Korzeniewski, C. Effects of surface step density on the electrochemical oxidation of ethanol to acetic acid. *J. Phys. Chem. B* **1997**, *101*, 253-258.

(13) Xia, X. H.; Liess, H.-D.; Iwasita, T. Early stages in the oxidation of ethanol at low index single crystal platinum electrodes. *J. Electroanal. Chem.* **1997**, *437*, 233-240.

(14) Lee, A. F.; Gawthrope, D. E.; Hart, N. J.; Wilson, K. A Fast XPS study of the surface chemistry of ethanol over Pt {111}. *Surf. Sci.* **2004**, *548*, 200-208.

(15) Shao, M. H.; Adzic, R. R. Electrooxidation of ethanol on a Pt electrode in acid solutions: in situ ATR-SEIRAS study. *Electrochim. Acta* **2005**, *50*, 2415-2422.

(16) Kutz, R. B.; Braunschweig, B.; Mukherjee, P.; Behrens, R. L.; Dlott, D. D.; Wieckowski, A. Reaction pathways of ethanol electrooxidation on polycrystalline platinum catalysts in acidic electrolytes. *J. Catal.* **2010**, *278*, 181-188.

(17) Xu, C. W.; Shen, P. K. Novel Pt/CeO2/C catalysts for electrooxidation of alcohols in alkaline media. *Chem. Comm.* **2004**, 2238-2239.

(18) Kwon, Y.; Lai, S. C. S.; Rodriguez, P.; Koper, M. T. M. Electrocatalytic Oxidation of Alcohols on Gold in Alkaline Media: Base or Gold Catalysis? *J. Am. Chem. Soc.* **2011**, *133*, 6914-6917.

(19) Lai, S. C. S.; Kleijn, S. E. F.; Öztürk, F. T. Z.; van Rees Vellinga, V. C.; Koning, J.; Rodriguez, P.; Koper, M. T. M. Effects of electrolyte pH and composition on the ethanol electro-oxidation reaction. *Catal. Today* **2010**, *154*, 92-104.

(20) Varcoe, J. R.; Slade, R. C. T. An electron-beam-grafted ETFE alkaline anion-exchange membrane in metal-cation-free solid-state alkaline fuel cells. *Electrochem. Comm.* **2006**, *8*, 839-843.

(21) Lu, J. P. S.; Li, Y.; Huang, A.; Lu, L. Z. J. High-Performance Alkaline Polymer Electrolyte for Fuel Cell Applications. *Adv. Funct. Mater.* **2010**, *20*, 312-319.

(22) Lamy, C.; Lima, A.; LeRhun, V.; Delime, F.; Coutanceau, C.; Léger, J.-M. Recent advances in the development of direct alcohol fuel cells (DAFC). *J. Power Sources* **2002**, *105*, 283-296.

(23) Lamy, C.; Rousseau, S.; Belgsir, E. M.; Coutanceau, C.; Leger, J. M. Recent progress in the direct ethanol fuel cell: development of new platinum-tin electrocatalysts. *Electrochim. Acta* **2004**, *49*, 3901-3908.

(24) García, G.; Rodríguez, P.; Rosca, V.; Koper, M. T. M. Fourier Transform Infrared Spectroscopy Study of CO Electro-oxidation on Pt(111) in Alkaline Media. *Langmuir* **2009**, *25*, 13661-13666.

(25) Lu, G. Q.; Lagutchev, A.; Dlott, D. D.; Wieckowski, A. Quantitative vibrational sum-frequency generation spectroscopy of thin layer electrochemistry: CO on a Pt electrode. *Surf. Sci.* **2005**, *585*, 3-16.

(26) Bayer, D.; Berenger, S.; Joos, M.; Cremers, C.; Tubke, J. Electrochemical oxidation of C-2 alcohols at platinum electrodes in acidic and alkaline environment. *Int. J. Hydrogen Energ.* **2010**, *35*, 12660-12667.

(27) Souza-Garcia, J.; Herrero, E.; Feliu, J. M. Breaking the C-C Bond in the Ethanol Oxidation Reaction on Platinum Electrodes: Effect of Steps and Ruthenium Adatoms. *ChemPhysChem* **2010**, *11*, 1391-1394.

(28) Severson, M. W.; Stuhlmann, C.; Villegas, I.; Weaver, M. J. Dipole–dipole coupling effects upon infrared spectroscopy of compressed electrochemical adlayers: Application to the Pt(111)/CO system. *J. Chem. Phys.* **1995**, *103*, 9832-9843.

3.8 Figures

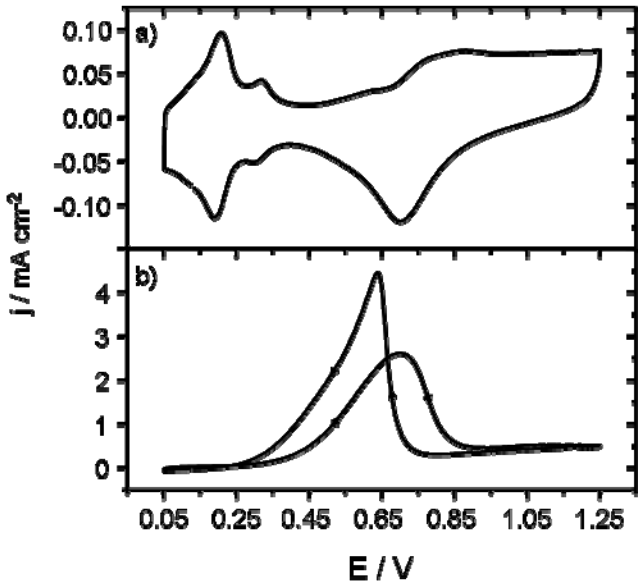

Figure 3.1. Hanging meniscus cyclic voltammograms of a polycrystalline Pt electrode in a) blank 0.1 M NaOH and b) 0.1 M NaOH with 0.5 M ethanol. The sweep rate for a) and b) was 50 mV/s.

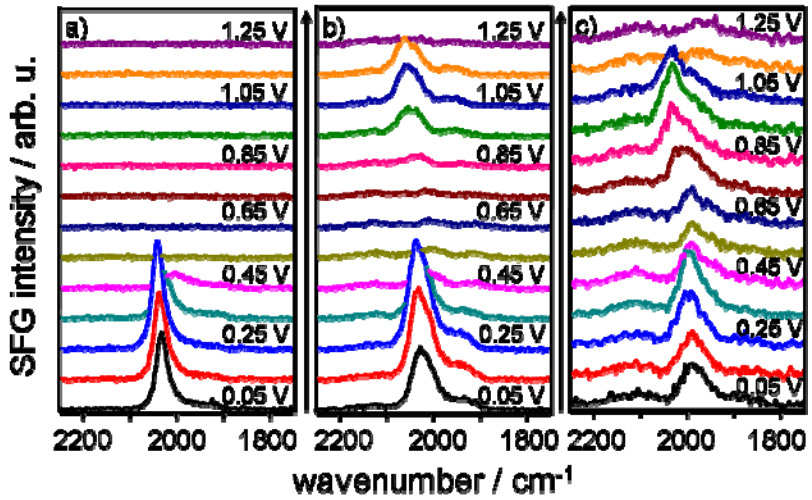

Figure 3.2. Potentiodynamic series of SFG spectra in 0.1 M NaOH with a) CO-saturation, b) 0.5 M ethanol (CH_3CH_2OH), and c) 0.5 M isotopically-labeled ethanol ($^{12}CH_3{}^{13}CH_2OH$). Potentials were as indicated in the figure. The acquisition time for each spectrum was 10 s for a) and 50 s for b) and c). The broadband IR pulse was centered at 2030 cm^{-1} for a) and b) and 1990 cm^{-1} for c).

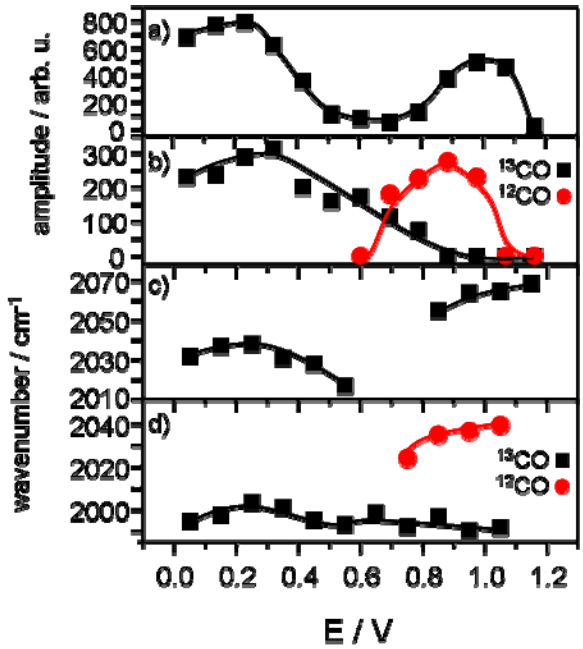

Figure 3.3. Potential dependence of SFG amplitudes for the vibrational bands in 0.1M NaOH centered at a) 2030 cm^{-1} with 0.5 M regular ethanol (Fig. 2b) and b) 2010 cm^{-1} and 1970 cm^{-1} with 0.5 M $^{12}CH_3{}^{13}CH_2OH$ (Fig. 2c). Frequencies of the CO vibrational bands from c) 0.5 M regular ethanol (Fig. 2b) and d) 0.5 M $^{12}CH_3{}^{13}CH_2OH$ (Fig. 2c).

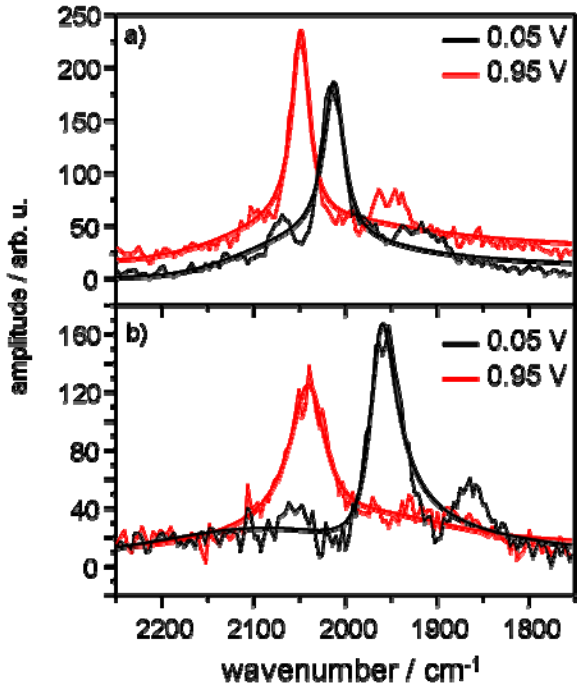

Figure 3.4. Comparison of the spectra for CO vibrational bands from solutions of a) 0.2 M regular ethanol and b) 0.2 M isotopically-labeled ethanol ($^{12}CH_3{}^{13}CH_2OH$) at potentials of 0.05 and 0.95 V. Modeled spectra are bolded and superimposed over their respective raw spectra to clearly indicate the position of each CO band.

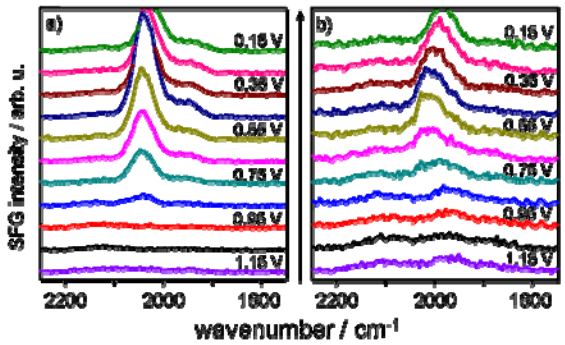

Figure 3.5 Potentiodynamic series of SFG spectra in 0.1 M NaOH with a) 0.5 M ethanol (CH_3CH_2OH), and b) 0.5 M isotopically-labeled ethanol ($^{12}CH_3{}^{13}CH_2OH$). Potentials and the direction of the potential sweep were as indicated in the figure. The acquisition time for each spectum was 50 s. The broadband IR pulse was centered at 2030 cm^{-1} for a) and 1990 cm^{-1} for b).

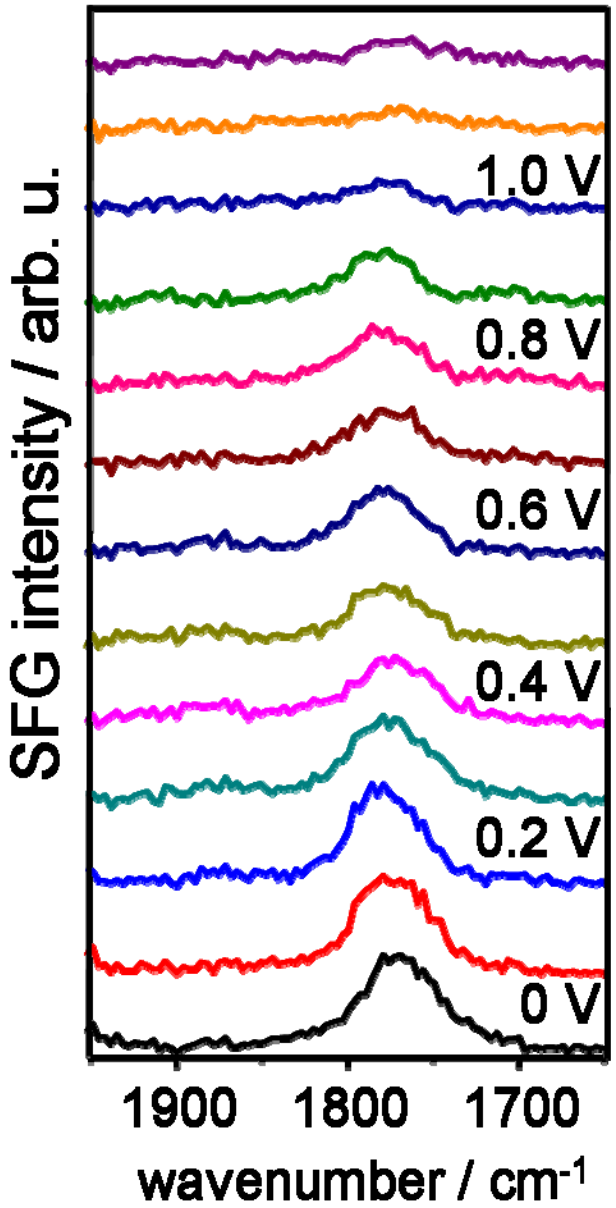

Figure 3.6. Potentiodynamic series of SFG spectra in 0.1 M NaOH with 0.5 M isotopically-labeled ethanol ($^{12}CH_3{}^{13}CH_2OH$). Potentials were as indicated in the figure. The acquisition time for each spectrum was 50 s. The broadband IR pulse was centered at 1770 cm^{-1}.

CHAPTER 4

FURTHER LIQUID FUEL STUDIES IN ACIDIC AND ALKALINE MEDIA

4.1 Notes and Acknowledgements

This chapter arises from further unpublished work done with both electrochemical and spectroscopic analyses of fuel oxidations. In some ways, it acts as a bridge for the prior two chapters, in that it offers more direct comparisons of other small organic molecule oxidations taking place in both alkaline and acidic electrolytes. Specifically, methanol and acetaldehyde oxidation on a Pt(poly) electrode are studied. Additionally, some spectroscopic information on the formic acid oxidation mechanism on a Pt(111) electrode is presented. Much of this work was done in an attempt to bring greater insight either to methanol or ethanol oxidation in varying pHs or simply observe new adsorbed chemical moieties, although the results are interesting in and of themselves and offer additional insight into the ability of electrochemical and spectroscopic techniques to complement one another.

I'd like to acknowledge several people for their assistance with this work, including Drs. Rachel Behrens, Björn Braunschweig, Prabuddha Mukherjee, Dana D. Dlott, and Andrzej Wieckowski. In particular, Drs. Behrens and Wieckowski were helpful in introducing me to the technique of fast-scan voltammetry. The specific spectra of the formate band were recorded by Dr. Braunschweig and are reproduced here with his permission. Research described in this study was supported by the US Army Research

Office under award W911NF-08-10309 as well as from the US Air Force Office of Scientific Research under award: FA9550-09-1-0163.

4.2 Introduction

The significant differences in the ethanol electrooxidation reactions that take place in acidic and alkaline electrolytes prompt one to wonder what the origin of these differences is and whether such disparity can also be found in the oxidation mechanisms of other small organic molecules. In particular, methanol and acetaldehyde are organic molecules that bear obvious similarity to ethanol, but they also bear potentially revealing differences. Methanol is a single-carbon molecule, and does not have the alpha carbon that was seen, in chapters 2 and 3, to persist on the platinum surface after carbon-carbon bond cleavage. Acetaldehyde is frequently considered an intermediate in ethanol oxidation[1-5] (indeed, it is featured in Scheme 2.1), and so one asks whether its oxidation would be significantly different from the oxidation of ethanol, and what this might say about their respective mechanisms.

Methanol's relative ease of oxidation when compared to ethanol has already made it a more practical fuel candidate for liquid fuel cells.[6-8] Multiple studies of methanol oxidation have yielded functioning prototype methanol fuel cells.[9, 10] Formic acid is another similar fuel source that functions similarly to a kind of liquid hydrogen, and research on formic acid[11] has produced powerful and innovative fuel cells for a variety of applications.[12-14] The power of SFG spectroscopy to probe deeper into these reaction mechanisms and possible adsorbates is thus potentially useful for the further

design of more immediately available fuel cells. Conversely, because methanol and formic acid are more volatile fuels than ethanol and have lower energy densities, any insights that their mechanisms of electrooxidation can provide for understanding ethanol's electrooxidation mechanism are well met.

Acetaldehyde, by contrast, is not really considered nearly as viable a fuel source for liquid fuel cells, although it has still been studied as such.[15-17] It is a molecule that bears much of the perceived disadvantages of ethanol, including the difficulty of C-C bond cleavage and the formation of varied single-carbon fragments, but does not even have the advantage of being as inexpensive or easily produced. The study of its electrooxidation mechanism is presented here solely as a contrast to the ethanol mechanism, and its further disadvantages as a fuel will become readily apparent.

With new innovations in membrane technology that pave the way for more practical alkaline fuel cells,[18, 19] a more complete understanding of how changes in pH affect these reactions is all the more necessary. Thus these studies provide a comparison of alkaline and acidic environments. As established in chapters 2 and 3, the polycrystalline platinum surface provides a good model catalyst surface for studying these reactions.

BB-SFG spectroscopy and in-situ electrochemistry are combined here much as they were in prior chapters. I also employ a technique known as fast-scan voltammetry, which permits unique electrochemical insight into how the proximity of certain current-generating chemical moieties to the electrode surface changes as a function of potential.[20, 21] Our lab has previously used this technique to study ethanol

electrooxidation on Pt(111) surfaces. The rapidity of the scan (10 V/s) precludes the observation of current generated from bulk oxidation of the fuel; thus, any signal generated from the anodic sweep comes from the oxidation of species that are already present at the electrode surface. In a sense, this is a surface-specific technique that is does not necessarily have the specificity, sensitivity or versatility of BB-SFG spectroscopy, but has a much finer time resolution.

4.3 Experimental

A polished platinum disk cut in the (111) orientation and a polished polycrystalline platinum disk (Matek) with 6 mm diameters were used as working electrodes in the SFG and electrochemical experiments. The counter electrode was a flame-annealed platinum wire (99.99%) and the reference electrode was a commercial Ag/AgCl (BASi; MF-2052; -0.25 vs. RHE) electrode. However, all potentials throughout this article are reported with respect to a reversible hydrogen electrode (RHE). Voltammetric experiments were carried out using a Princeton Applied Research (PAR 263A) potentiostat. Solutions were prepared using $HClO_4$ (double-distilled, GFS Chemicals), NaOH (>97%, Sigma-Aldrich), methanol (>99.9%, Sigma-Aldrich), acetaldehyde (>99.0%, Sigma-Aldrich) and formic acid (> 88%, Sigma-Aldrich). All dilutions were performed using ultra-pure water ($\geq$18.2 MΩ, total oxidizable carbon $\leq$ 4ppb) obtained from a Millipore Gradient A10 purification system and all solutions were thoroughly purged with Ar gas (ultra-high purity). Prior to each experiment, the Pt disk was soaked in concentrated sulfuric acid, rinsed with ultrapure water, and

electrochemically cleaned by potential cycling between 0 and 1.3 V for >50 cycles at a sweep rate of 200 mV/s. The Pt(111) disk was then annealed according to the Clavilier method, as follows. The disk was heated in a hydrogen flame to white heat for five minutes, then placed in a sealed argon/hydrogen environment to cool for five minutes. It was then lowered into ultrapure water that had been purged with argon and hydrogen so that a protective drop would form on the surface of the Pt(111) crystal, and it was then transferred to the electrochemical cell.

Our BB-SFG apparatus permits the rapid acquisition of vibrational spectra synchronized with a voltammetric sweep. Tunable broadband infrared (BBIR) pulses were generated in an optical parametric amplifier (Light Conversion; Topas) that was pumped by a femtosecond Ti:Sapphire laser system (Quantronix; Integra C series) at a repetition rate of 1 kHz. The BBIR pulses had typical pulse durations of ~120 fs, typical bandwidths of Δ >150 cm^{-1} and pulse energies of approximately 8 μJ at a frequency Ω of 2083 cm^{-1}. Narrow-band visible pulses with 5 μJ pulse energy and a fixed wavelength of 800 nm were generated by narrowing the fs pulses to a bandwidth of <10 cm^{-1} with a Fabry-Pérot etalon. Narrow-band visible and BBIR pulses were overlapped in time and space at an incident angle of ~60º to the normal of the Pt-electrolyte interface. Sum-frequency photons were collected with a spectrograph and a charge-coupled device (CCD). The SFG, visible, and IR photons were all p-polarized. Spectro-electrochemical experiments were carried out in a previously described electrochemical cell for synchronized SFG and electrochemical experiments. In this electrochemical cell, a well-defined gap of 25 μm between the electrode surface and a CaF_2 optical window is

established by a Teflon spacer of the same thickness. The 25 µm electrolyte gap allows for voltammetric scans at sweep rates of ≤ 5 mV/s without the detriment of strong ohmic drop effects that are associated with thin-layer electrochemistry.

The following equation describes the model used for the intensity $I(\omega_{SF})$ of the SFG signals and its dependent parameters:

$$I(\omega_{SF}) \propto \left| \chi_{NR}^{(2)} + \sum_q \frac{A_q \cdot e^{-i\theta_q}}{(\omega_{IR} - \omega_q) + i\Gamma_q} \right|^2 \cdot I(\omega_{vis}) I(\omega_{IR}) \exp\left[-4 \ln 2 \frac{(\omega - \Omega)^2}{\Delta^2} \right] \quad (1)$$

Here, Ω and Δ refer to the frequency and bandwidth of the impinging BBIR pulse, while A_q, θ_q, ω_q, and Γ_q are amplitude, relative phase, frequency, and homogenous linewidth of the q-th vibrational mode, respectively. $\chi_{NR}^{(2)}$ is the non-resonant component of the interfacial second-order nonlinear susceptibility $\chi^{(2)}$. $\chi_{NR}^{(2)}$ is nearly independent of the BBIR frequency Ω and manifests as a featureless SFG contribution produced by the surface, but is highly dependent on the electronic structure of the surface [22]. Because we are mostly interested in resonant contributions of $\chi^{(2)}$ which are associated with adsorbed molecular species, we have applied a $\chi_{NR}^{(2)}$ suppression technique previously reported by Lagutchev et al.[23, 24] This technique, however, requires a compromise between a complete suppression of $\chi_{NR}^{(2)}$ and maintaining a relatively good signal-to-noise ratio of the observed vibrational bands.

Fast-scan voltammetry was preformed by taking voltammetric sweeps at 10 V/s and applying iR (current-resistance) compensation. Prior to each voltammetric sweep,

the electrode was held at a given potential for 60 seconds. Due to the very rapid nature of the technique and the need to apply iR compensation, features on the resultant cyclic voltammogram are frequently somewhat broad and distorted. The level of iR compensation is dynamically adjusted for each system in order to limit the extent to which the CVs are distorted from the shapes that are typically expected at much slower sweep rates such as 50 mV/s.

4.4 Results

Figure 4.1 shows comparative cyclic voltammograms of Pt(poly) in a) 0.1 M NaOH and b) 0.1 M $HClO_4$. There are three distinct and obvious differences in their features. First, the double layer region between 0.3 and 0.75 V in $HClO_4$ is quite a bit thicker in current density and narrower in potential scale in the NaOH electrolyte. Secondly, the oxide reduction peak in NaOH is broader and centered at more negative applied potentials. Third, and perhaps most relevantly, the oxide formation onset occurs more than 100mV more anodic in $HClO_4$ than in NaOH.

Figure 4.2 shows cyclic voltammograms drawn from the oxidation of methanol in acidic and alkaline electrolytes. In acidic electrolytes, there are two distinguishable current features on the anodic sweep and one on the cathodic sweep. This cathodic-sweep current feature, as in earlier chapters, is a restoration feature associated with the stripping of surface oxides, both of which occur at approximately 0.75 V. The same relationship is seen between the cathodic sweep feature and oxide reduction in the

NaOH sweeps. In NaOH solution, there is also a single current feature prominently visible on the anodic sweep.

Figure 4.3 shows amperograms taken from solutions of methanol in a) $HClO_4$ and b) NaOH. In perchloric acid, holding at 0.6 V produced the most current, although some sustained current was also generated at 1.0 V. Current density produced by holding at 0.6 V in NaOH solution is remarkably higher, but it is practically negligible at the other two potentials in alkaline solution.

Figure 4.4 shows a potentiodynamic series of SFG spectra taken from the oxidation of methanol in NaOH. CO from methanol oxidation in acidic solutions has been previously reported in the literature, but the scan of methanol oxidized in NaOH is presented here for its anomalous nature. The vibrational band corresponding to adsorbed CO changes in intensity as a function of potential and has a rather dynamic Stark tuning response, but it never fully disappears at any potential. Figure 4.5 is a comparison of this Stark tuning response and the amplitude of the CO vibrational band from methanol oxidation in NaOH electrolyte. The blue band corresponds to the anodic sweep and the red band corresponds to the cathodic sweep. In Fig. 4.5b, the black line is the CV of methanol oxidation in NaOH superimposed as a convenient reference.

Figure 4.6 is a comparative series of fast-scan cyclic voltammograms of methanol adsorbed at varying potentials on a Pt(poly) crystal in a) $HClO_4$ and b) NaOH electrolytes. The peak visible at approximately 0.8 V (+/- 0.1V) corresponds to a CO-stripping peak. Unfortunately, the blank CV of Pt(poly) is distorted even with iR compensation, and the beginning of the oxide formation region is warped such that it looks slightly similar to

the CO oxidation peak at higher anodic potentials. However, it can be distinguished as being narrower, pointed, and less intense, and the disappearance of the CO oxidation feature at the holding potential of 0.7 V is readily apparent.

Figure 4.7 shows hanging meniscus cyclic voltammograms of acetaldehyde being oxidized in a) 0.1 M $HClO_4$ and b) 0.1 M NaOH. Figure 4.8 shows amperograms of this same system. The current response of acetaldehyde in NaOH is different largely due to the very sharp and sudden current feature on the cathodic sweep at about 0.7 V, coinciding with the removal of surface oxides. This restoration feature is far more significant in alkaline media than acidic media when compared to the current response on the anodic sweep. It is somewhat unsurprising that the amperograms show a sustained significant current response only at 0.8 V in either electrolyte, as this is the only one of the three tested potentials in which a current feature is observed in the cyclic voltammogram. Note that this sustained current appears much higher in alkaline than in acidic electrolytes.

It should be noted that holding the potential anywhere between 0 V and 0.5 V in NaOH electrolyte with 0.5 M acetaldehyde caused the solution to turn yellow within a matter of seconds and began to cause current overload responses from the potentiostat, likely indicating a sudden increase in the resistance of the region between the working and reference electrode. Some chemical transformation of the solution was taking place (possibly a polymerization of the acetaldehyde molecule) that was apparently not reversible, as sweeping the potential in either direction did nothing to affect the solution after that point.

Figure 4.9 shows a potentiodynamic series of SFG spectra comparing the CO vibrational band from acetaldehyde oxidation in a) 0.1 M $HClO_4$ and b) 0.1 M NaOH. Contrary to what is expected from knowing the behavior of ethanol oxidation in alkaline media shown in chapter 3, here surface-bound CO continues to be observed up to 0.7 V. Figure 4.10 clarifies this behavior and further shows that the CO formation and adsorption behavior from acetaldehyde oxidation is very similar between acidic and alkaline electrolytes.

Finally, Figure 4.11 shows a meniscus CV of formic acid oxidation on a Pt(111) surface in 0.1 M H_2SO_4 and Figure 4.12 shows potentiodynamic spectra of the same system. Fig 4.12a shows the vibrational band at approximately 1340 cm^{-1} corresponding to the symmetric O-C-O stretch of the adsorbed formate radical. Fig 4.12b shows this same system with the IR focus at 2080 cm^{-1} in order to show the relationship between adsorbed CO from formic acid oxidation and adsorbed formate. As was the case for acetate in ethanol oxidation, formate appears on the surface once CO has been stripped away.

4.5 Discussion

The studies of methanol and acetaldehyde oxidation in alkaline media are remarkable for their anomalous behavior, providing results that are somewhat unexpected from literature precedent and the studies of ethanol oxidation presented in chapter 3. Analyses of data from methanol, acetaldehyde, and formic acid studies are presented here in separate sections.

4.5.1 Methanol Oxidation

The formation of surface-bound CO from methanol oxidation in acidic electrolytes has been thoroughly reported on in the literature,[25-28] and I performed a study in NaOH only to provide contrast to the ethanol oxidation in alkaline electrolytes. The SFG-observed persistence of surface-bound CO across the entire potential range was quite unexpected, however, and is difficult to trust this waterfall of spectra in Fig 4.4 as truly, or at least obviously, representative of the mechanism of CO formation and oxidation from methanol fuel in alkaline electrolytes. It thus bears closer examination. By comparing the Stark tuning response to the CO band amplitude, as shown in Fig 4.5, one notices an interesting relationship. At the onset of the anodic current feature at approximately 0.3 V, there is a very modest steady decline of the CO vibrational band amplitude and a rather more dramatic dip in the Stark tuning response. Both the CO band amplitude and Stark tuning response then dramatically rise at approximately 0.9 V and continue to do so until the end of the anodic sweep. Their behaviors on the cathodic sweep are also similar.

This visual accord between the Stark tuning and band amplitude curves is more apparently a contradiction, however. To the extent that variations in Stark tuning are understood to correlate to CO coverage, one expects Stark tuning values to be higher at lower CO coverages (this relationship is more fully expanded upon in Chapter 5). Thus, if both curves are indicative of the surface coverage of CO, then they ought more predictably to be inversions of one another.

A better and more thorough understanding of what is occurring spectroscopically is thus quite challenging, but fast-scan voltammetry can be used to determine whether there is sufficient reason to believe that CO is truly adsorbed to the catalyst surface at very high potentials in this system, as Fig 4.4 seems to indicate. Figure 4.6 shows the persistence of a strong CO-stripping current feature at holding potentials as high as 0.6 V, but not at the high anodic potentials indicated in the SFG spectra. This is similar to what is observed in acidic media, as shown in Fig 4.6a. Thus, we can infer that if Fig 4.4 is to be trusted, then what is being observed at potentials above 0.6 V is almost certainly the steady-state formation of CO due to rapid bulk oxidation of the methanol molecule. Unfortunately, one can only conjecture from this point about the more specific spectral behavior of adsorbed CO in this system. If methanol is truly so rapidly oxidized in alkaline media to form significant quantities of CO across the entire potential range, then the low time-resolution of our SFG system may be prohibitive of our acquiring more precise data on this point.

4.5.2 Acetaldehyde Oxidation

Acetaldehyde oxidation appears similar in acidic and alkaline electrolytes, despite the precedent set for ethanol oxidation in Chapters 2 and 3. Figure 4.7 shows current features in both a) and b) that have very similar onset potentials, although the 'restoration' feature on the cathodic sweep in Fig. 4.7b is obviously much larger than the current features on the anodic sweep. Figure 4.8 shows that the vibrational band corresponding to atop-site CO appears to actually persist at higher potentials in alkaline

media, quite contrary to what is expected from the ordinarily lower overpotentials required for oxidizing CO to CO_2.

With the available data, one can only conjecture as to the cause of this behavior. However, we see this same persistence of surface-adsorbed CO in alkaline electrolytes on Pt(111) surfaces, as Chapter 5 will show. This implies that although the higher pH environment can promote CO oxidation at lower overpotentials, there is probably still some requirement that kinds of catalyst surface sites be available for CO oxidation to occur at these lower overpotentials. As mentioned earlier, holding the potential for even a short amount of time in the region between 0 and 0.5 V appears to cause a chemical transformation of the acetaldehyde solution which may be polymerization. Whatever its exact nature, it could be that this behavior, which is not observed in ethanol, is causing the blockage of surface sites required for CO to oxidize at lower overpotentials.

Regardless, two things are clear: carbon-carbon bond cleavage of acetaldehyde can occur at potentials as low as 0 V, and it is very unlikely that acetaldehyde persists for any considerable length of time as an intermediate in the ethanol oxidation reaction in alkaline electrolytes. The former is obvious from the observance of CO at very low overpotentials. The latter is clear because we do not see this same strong persistence of CO in such a single wide potential range during oxidation of 0.5 M ethanol in NaOH, as seen in Chapter 3. If acetaldehyde were a significant long-lasting intermediate in the ethanol oxidation mechanism in NaOH, we would see this CO behavior during ethanol oxidation.

4.5.3 Formic Acid Oxidation

The oxidation mechanism of formic acid on platinum catalysts is fairly well-known.[29-31] The primary purpose of this study was to determine whether the formate radical could be observed using SFG. Previously it has been observed to persist mostly on Pt(111) surfaces and, to a much lesser extent, on Pt(100) surfaces.

The anodic sweep of Figure 4.11 shows one current feature with an onset at 0.65 V. This corresponds to the stripping of CO from the surface and the adsorption of the formate radical, as seen in Fig. 4.12. Thus, there is reason to believe that the adsorption of CO and formate is competitive. Additionally, the vibrational band at 1320 cm^{-1} is a symmetric carboxylate stretch, with no asymmetric stretch; the formate radical is believed to bind to the surface by its two oxygen atoms.[32]

4.6 Conclusions

The oxidation of methanol, acetaldehyde, and formic acid were studied under varying conditions. BB-SFG spectra of methanol oxidation in alkaline electrolytes were highly anomalous and difficult to confidently interpret. It is likely that they show steady-state formation of CO for much of the potential sweep, but the lower time-resolution of our SFG setup troubles the confirmation of this. Fast-scan cyclic voltammetry reveal that surface-bound CO is not found in significant quantities after holding at anodic potentials of 0.7 V and above.

The study of acetaldehyde as a possible intermediate of ethanol oxidation also yields anomalous results in alkaline electrolytes. Nevertheless, its unique CO production behavior and tendency to rapidly undergo a chemical transformation at low potentials indicated by a color change indicates that it is unlikely to be a long-lasting intermediate of ethanol oxidation in alkaline electrolytes. If it were, we would see some evidence of this behavior in the oxidation of ethanol itself.

Finally, formic acid oxidation on a Pt(111) crystal shows the adsorption of the formate radical to terrace sites at potentials above 0.65 V. The formate radical appears to compete with CO for binding sites. Unfortunately, this same band could not be observed on Pt(poly) or Pt(100) surfaces.

4.7 References

1. M. Heinen, Z. Jusys and R. J. Behm, *J. Phys. Chem. C*, 2010, **114**, 9850.
2. S. C. S. Lai, S. E. F. Kleyn, V. Rosca and M. T. M. Koper, *J. Phys. Chem. C*, 2008, **112**, 19080.
3. R. S. Ferreira, V. R. Oliveira, R. Reis, G. Maia and G. A. Camara, *J. Power Sources*, 2008, **185**, 853.
4. E. A. Batista, G. R. P. Malpass, A. J. Motheo and T. Iwasita, *Electrochem. Commun.*, 2003, **5**, 843.
5. E. A. Batista, G. R. P. Malpass, A. J. Motheo and T. Iwasita, *J. Electroanal. Chem.*, 2004, **571**, 273.
6. L. Barelli, G. Bidini, F. Gallorini and S. Servili, *Energy*, 2008, **33**, 554.
7. A. K. Shukla, M. K. Ravikumar and K. S. Gandhi, *J. Solid State Electrochem.*, 1998, **2**, 117.
8. V. Neburchilov, J. Martin, H. J. Wang and J. J. Zhang, *Journal of Power Sources*, 2007, **169**, 221.
9. N. T. Nguyen and S. H. Chan, *J. Micromech. Microeng.*, 2006, **16**, R1.
10. T. S. Zhao, W. W. Yang, R. Chen and Q. X. Wu, *Journal of Power Sources*, **195**, 3451.
11. G. Q. Lu, Crown, Alecia, and Wieckowski, Andrzej, *J Phys Chem B.*, 1999, **103**, 12.
12. N. V. Rees and R. G. Compton, *J. Solid State Electrochem.*, **15**, 2095.
13. X. W. Yu and P. G. Pickup, *Journal of Power Sources*, 2008, **182**, 124.
14. W. M. Qian, D. P. Wilkinson, J. Shen, H. J. Wang and J. J. Zhang, *Journal of Power Sources*, 2006, **154**, 202.
15. K. Taneda and Y. Yamazaki, *Journal of Power Sources*, 2006, **157**, 177.
16. S. Malhotra and R. Datta, *J. Electrochem. Soc.*, 1996, **143**, 3058.
17. S. Sun, M. Heinen, Z. Jusys and R. J. Behm, *Journal of Power Sources*, 2012, **204**, 1.
18. V. Rao, Hariyanto, C. Cremers and U. Stimming, *Fuel Cells*, 2007, **7**, 417.
19. J. R. Varcoe and R. C. T. Slade, *Fuel Cells*, 2005, **5**, 187.
20. T. Fukuda and A. Aramata, *J. Electroanal. Chem.*, 1999, **467**, 112.
21. G. Q. Lu, W. Chrzanowski and A. Wieckowski, *J. Phys. Chem. B*, 2000, **104**, 5566.
22. Y. R. Shen, *Nature*, 1989, **337**, 7.
23. A. Lagutchev, A. Lozano, P. Mukherjee, S. A. Hambir and D. D. Dlott, *Spectrochim. Acta A*, 2010, **75**, 1289.
24. H. S. Lagutchev A, Dlott D, *J. Phys. Chem. C*, 2007, **111**, 3.
25. J. A. Caram and C. Gutierrez, *Journal of Electroanalytical Chemistry*, 1993, **344**, 313.

26. W. S. Li, L. P. Tian, Q. M. Huang, H. Li, H. Y. Chen and X. P. Lian, *Journal of Power Sources*, 2002, **104**, 281.
27. V. Diaz and C. F. Zinola, *J. Colloid Interface Sci.*, 2007, **313**, 232.
28. T. D. Jarvi, S. Sriramulu and E. M. Stuve, *Colloid Surf. A-Physicochem. Eng. Asp.*, 1998, **134**, 145.
29. M. Choy, F. Hahn, J. M. Leger, C. Lamy and J. M. Ortega, *Thin Solid Films*, 2007, **515**, 3611.
30. J. D. Lovic, A. V. Tripkovic, S. L. J. Gojkovic, K. D. Popovic, D. V. Tripkovic, P. Olszewski and A. Kowal, *Journal of Electroanalytical Chemistry*, 2005, **581**, 294.
31. J. L. Haan and R. I. Masel, *Electrochimica Acta*, 2009, **54**, 4073.
32. Y. X. Chen, A. Miki, S. Ye, H. Sakai and M. Osawa, *Journal of the American Chemical Society*, 2003, **125**, 3680.

4.8 Figures

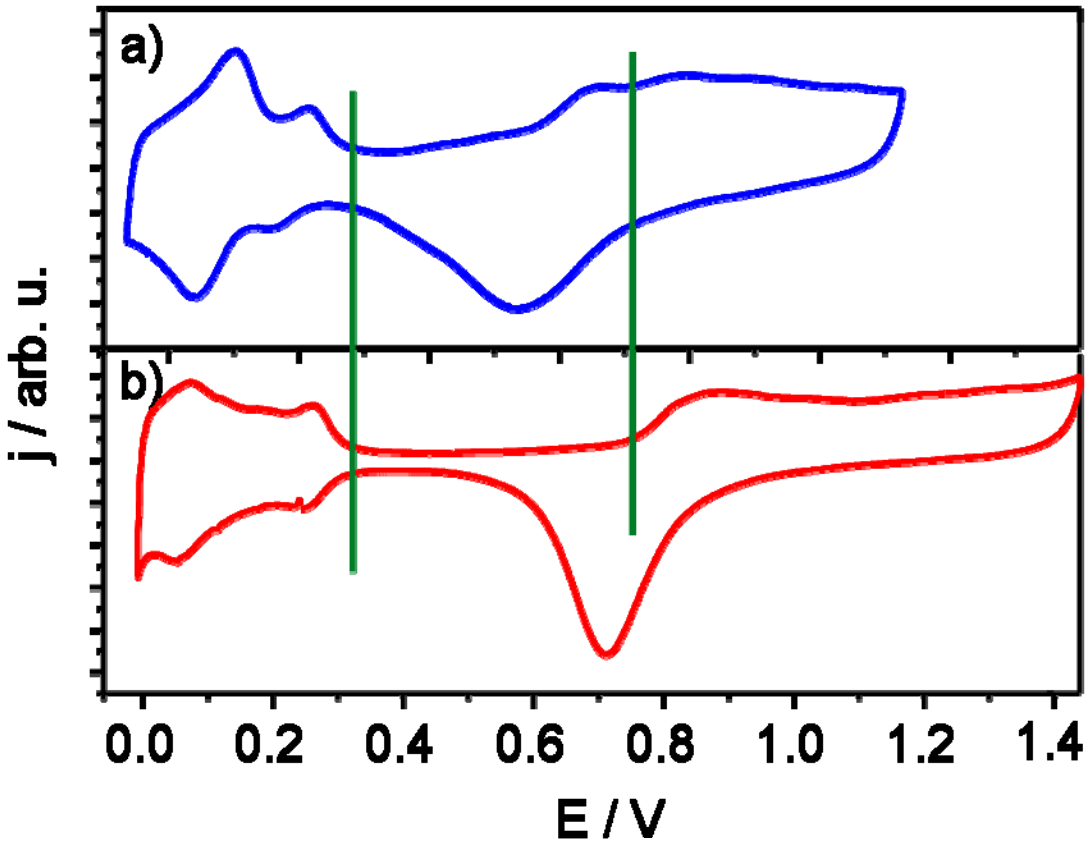

Figure 4.1. Hanging meniscus cyclic voltammograms of a polycrystalline Pt electrode in a) blank 0.1 M NaOH and b) blank 0.1M $HClO_4$. Green lines are a guide to show the double layer region in b) as compared to a). Sweep rates are 50 mV/s for both CVs and potentials are normalized against the RHE.

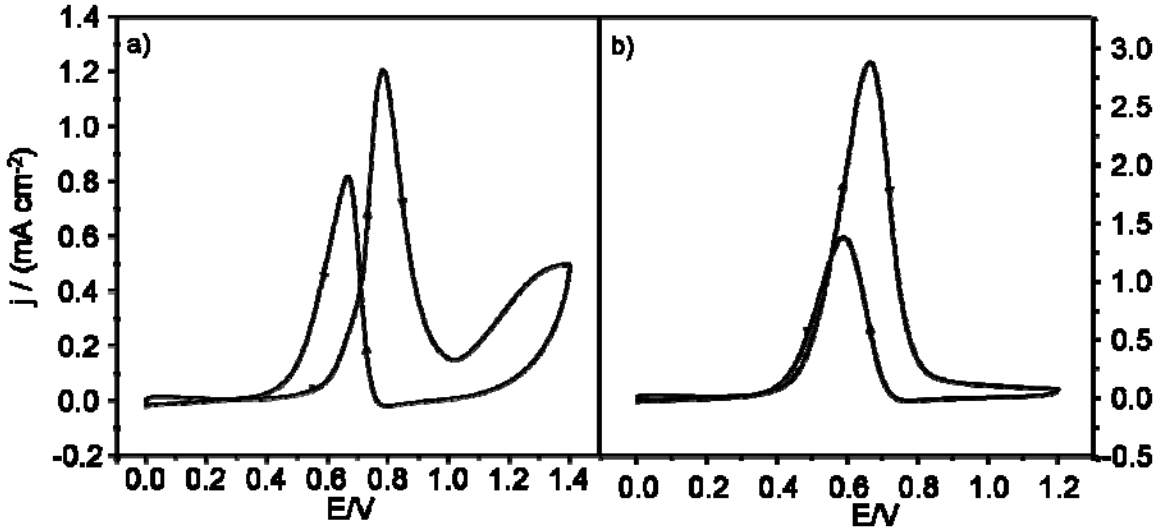

Figure 4.2. Hanging meniscus cyclic voltammograms of a polycrystalline Pt electrode in a) 0.1 M $HClO_4$ with 0.5 M methanol and b) 0.1 M NaOH with 0.5 M methanol. Sweep rates are 50 mV/s for both CVs and potentials are normalized against the RHE.

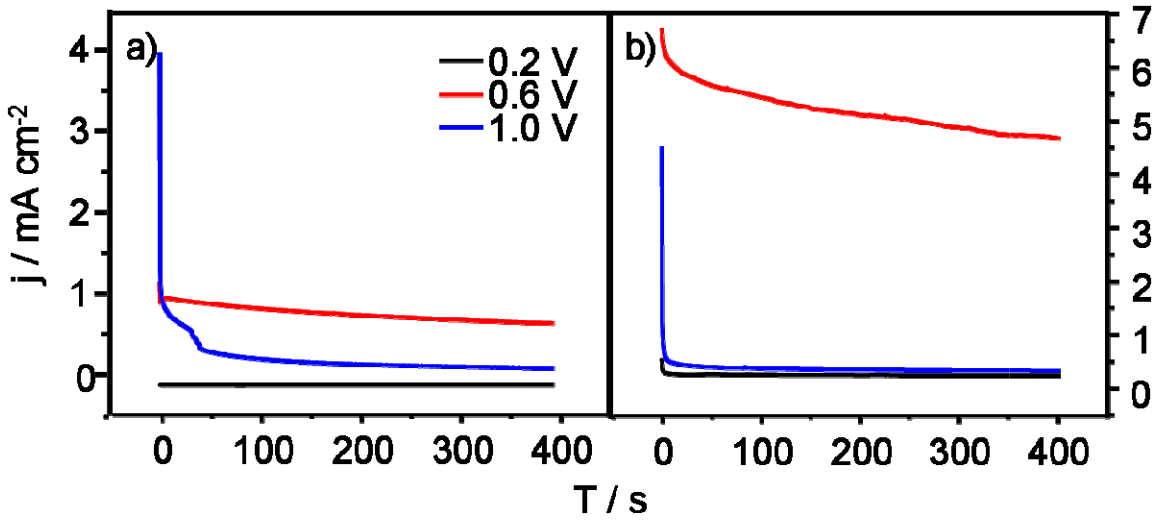

Figure 4.3. Chronoamperograms of a polycrystalline Pt disk in solutions of a) 0.1 M $HCLO_4$ and b) 0.1 M NaOH each with 0.5 M methanol. Potentials were stepped from open-circuit conditions to the potentials indicated in the figure.

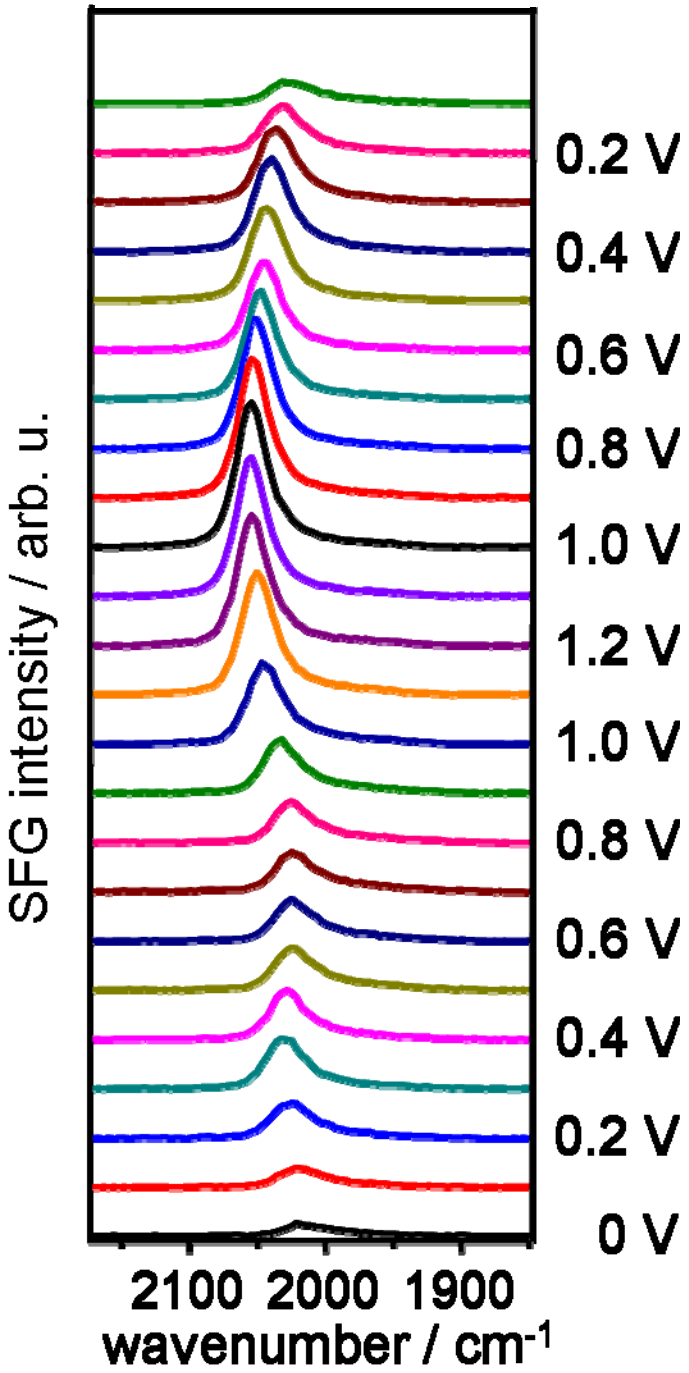

Figure 4.4. Potentiodynamic series of SFG spectra in 0.1 M NaOH with 0.5 M methanol. The broadband IR pulse was centered at 2030 cm^{-1}. Potential values are shown with respect to RHE.

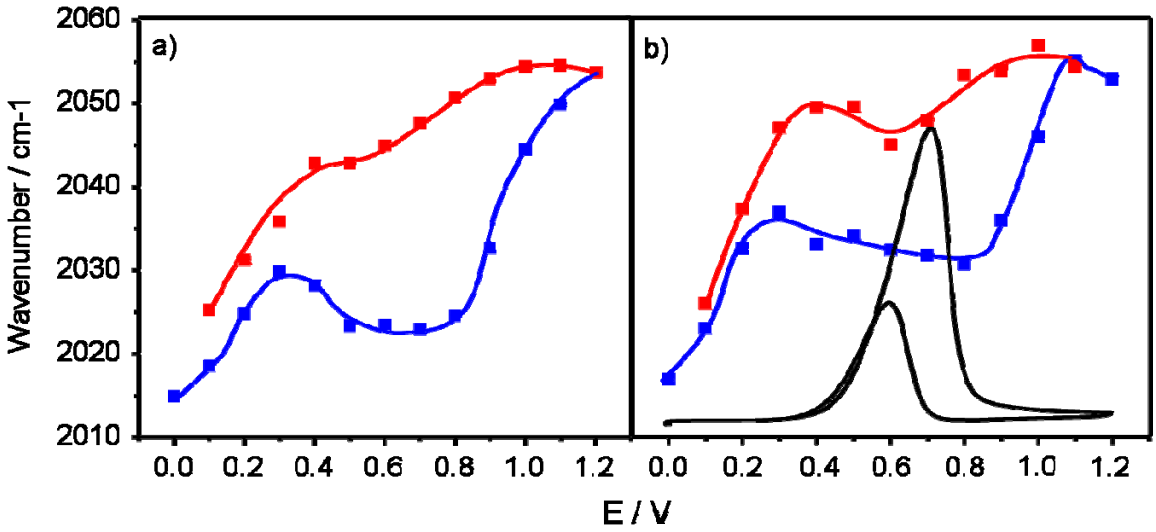

Figure 4.5. A comparison of a) the Stark tuning response of the CO vibrational band corresponding to CO created during the oxidation of methanol in NaOH solution and b) amplitude of that same vibrational band. The blue band corresponds to the anodic potential sweep, and the red band corresponds to the cathodic potential sweep. These curves are provided as guides for the eye. In part b), the black line represents the CV of methanol oxidation in NaOH, and is superimposed as reference.

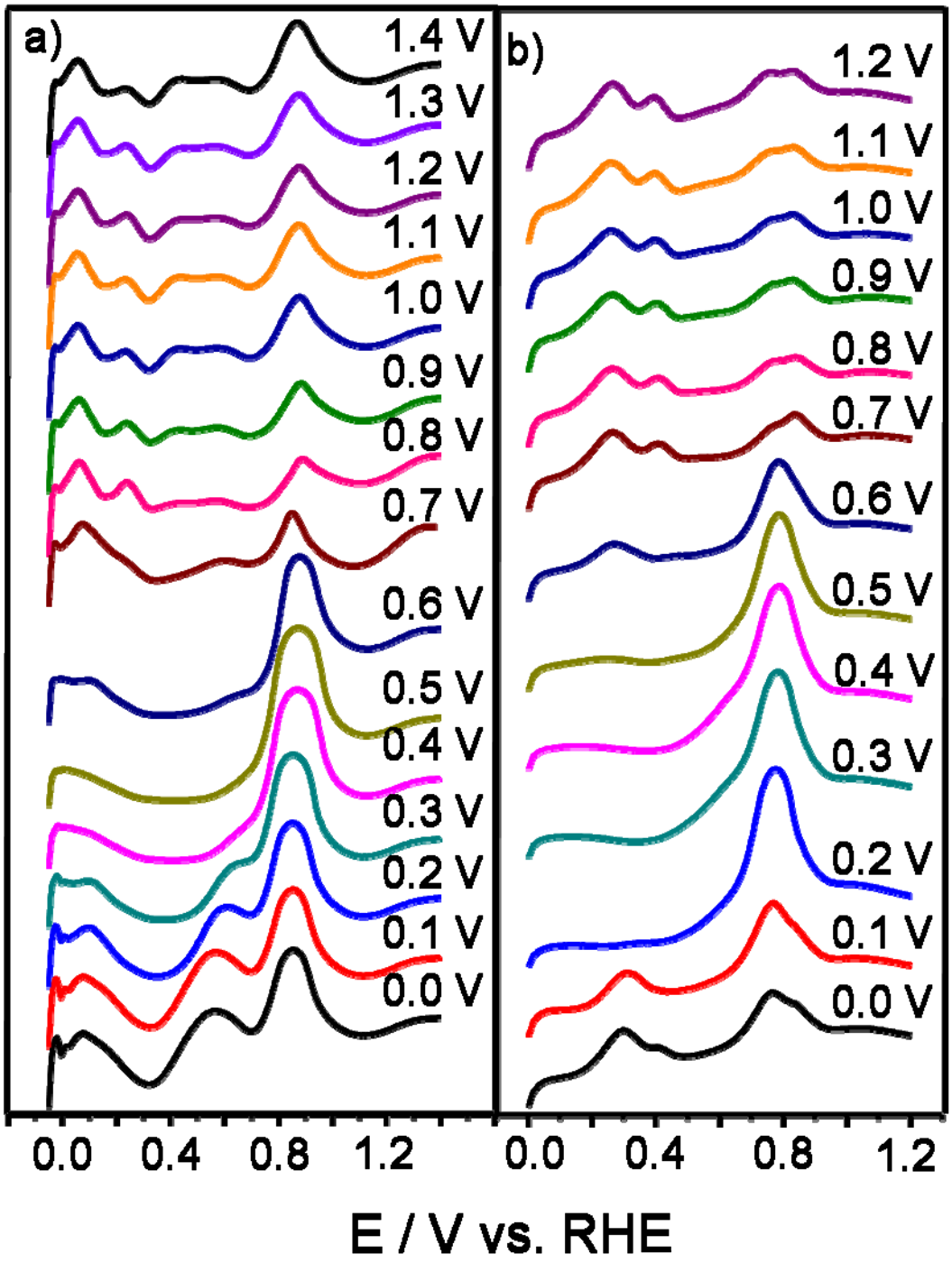

Figure 4.6. Potentiodynamic series of fast-scan cyclic voltammograms of a polycrystalline Pt electrode in a) 0.1 M $HClO_4$ with 0.5 M methanol and b) 0.1 M NaOH with 0.5 M methanol. Only anodic sweeps are shown. Each sweep was taken at 10 V/s. Indicated potentials were held for 60 seconds prior to each sweep.

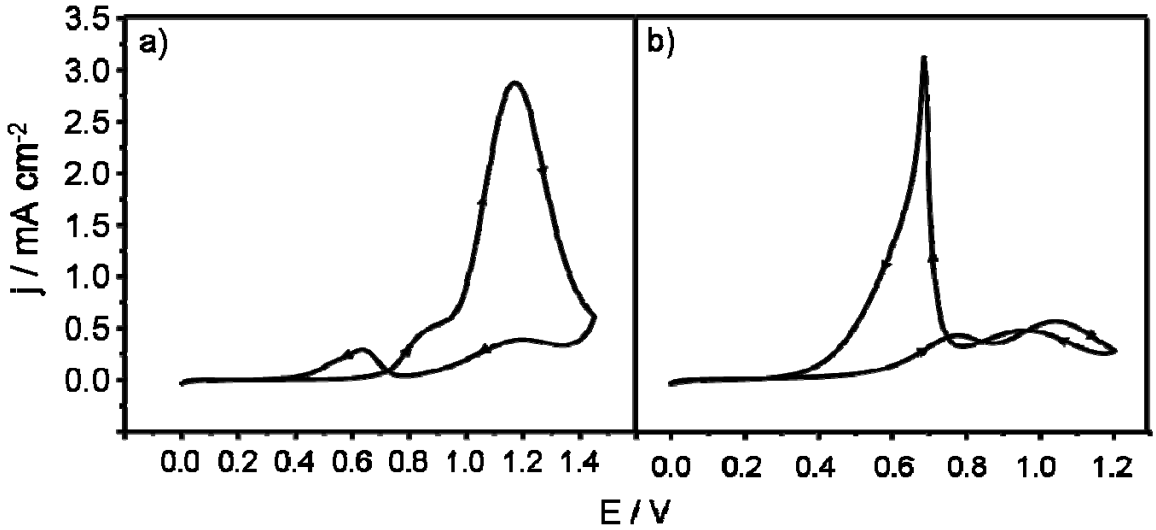

Figure 4.7. Hanging meniscus cyclic voltammograms of a polycrystalline Pt electrode in a) 0.1 M $HClO_4$ with 0.5 M acetaldehyde and b) 0.1 M NaOH with 0.5 M acetaldehyde. Sweep rates are 50 mV/s for both CVs and potentials are normalized against the RHE.

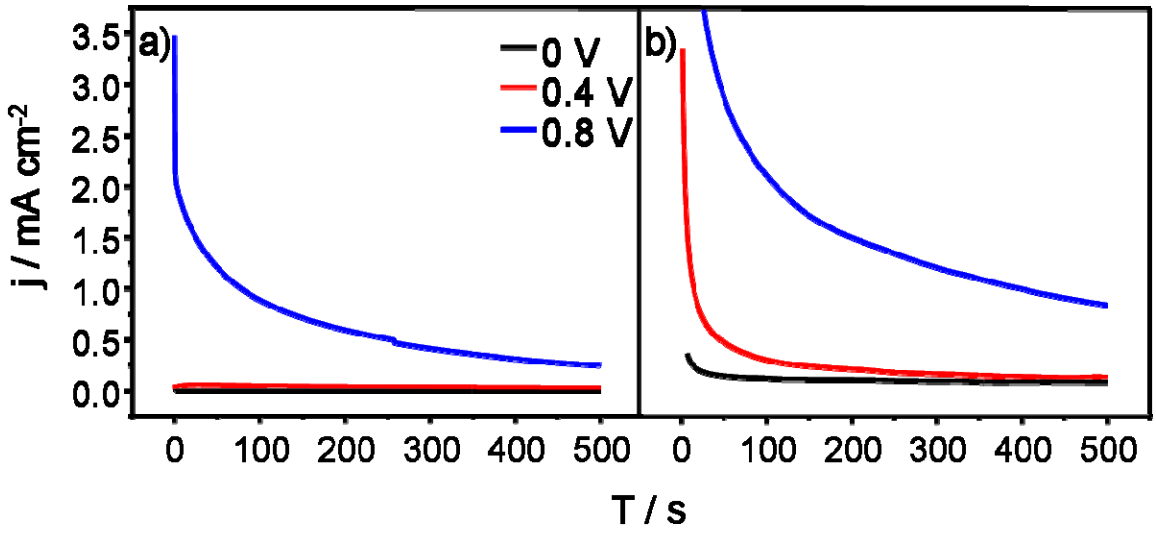

Figure 4.8. Chronoamperograms of a polycrystalline Pt disk in solutions of a) 0.1 M $HCLO_4$ and b) 0.1 M NaOH each with 0.5 M acetaldehyde. Potentials were stepped from open-circuit conditions to the potentials indicated in the figure.

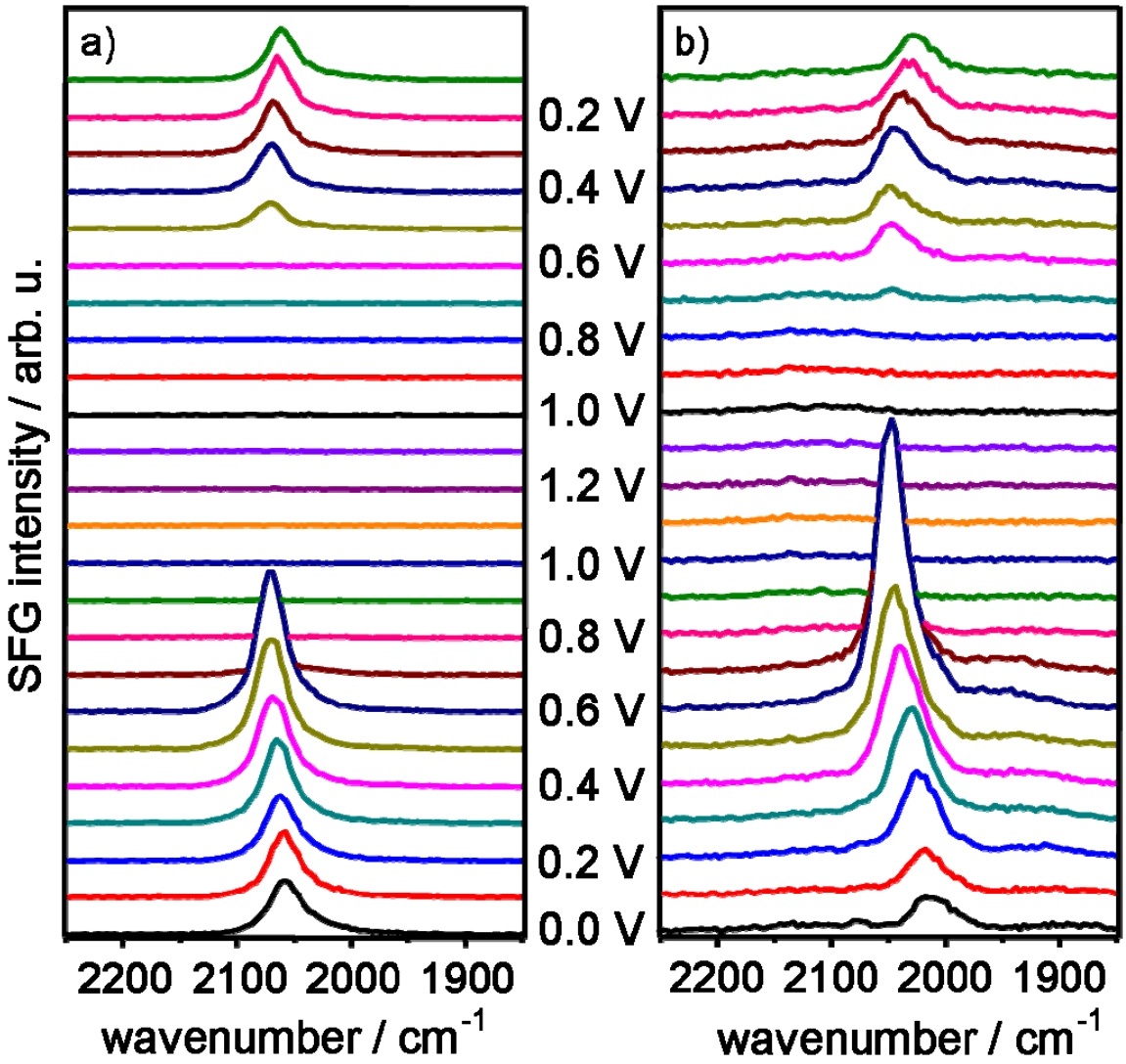

Figure 4.9. Potentiodynamic series of SFG spectra in a) 0.1 M $HClO_4$ with 0.5 acetaldehyde and b) 0.1 M NaOH with 0.5 M acetaldehyde. The broadband IR pulse was centered at 2080 cm^{-1} and 2030 cm^{-1} respectively. Potential values are shown with respect to RHE.

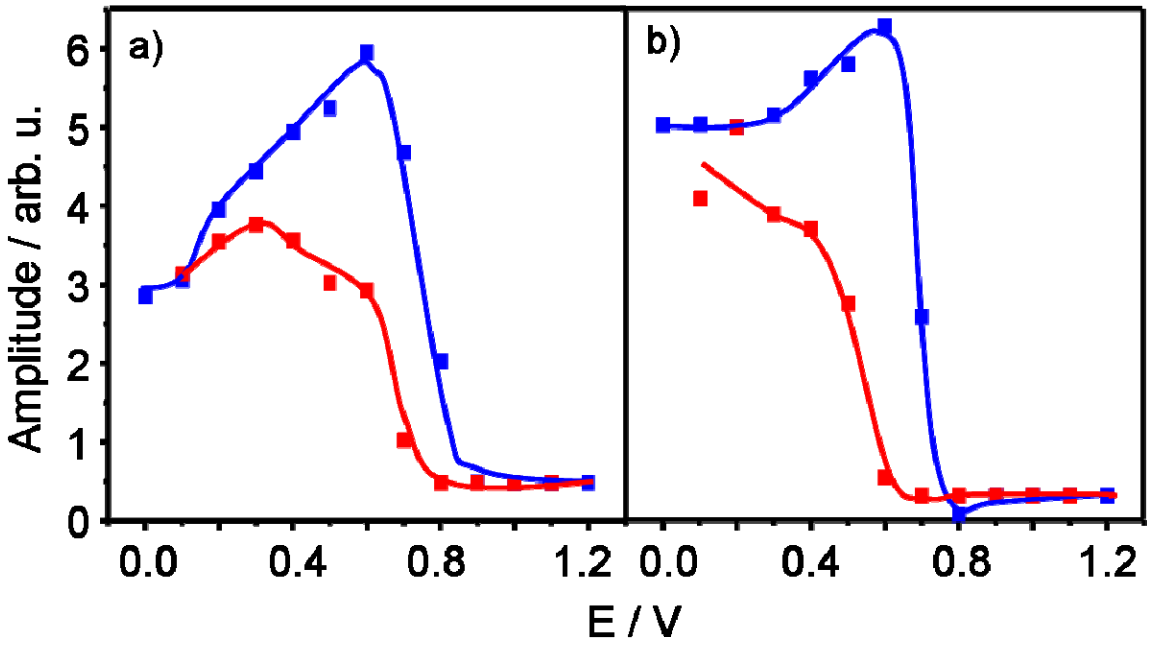

Figure 4.10. Potential dependence of SFG amplitudes for the vibrational bands corresponding to CO atop from the oxidation of 0.5 M acetaldehyde in a) 0.1 M $HClO_4$ and b) 0.1 M NaOH.

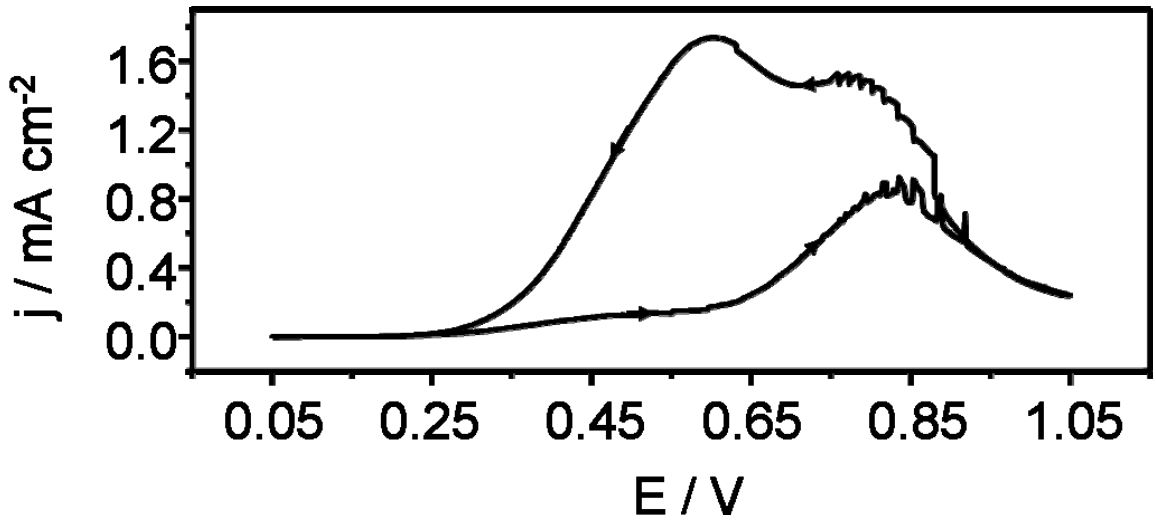

Figure 4.11. Hanging meniscus cyclic voltammogram of a Pt(111) electrode in 0.1 M H_2SO_4 with 0.5 M formic acid. The sweep rate is 50 mV/s and potentials are normalized against the RHE.

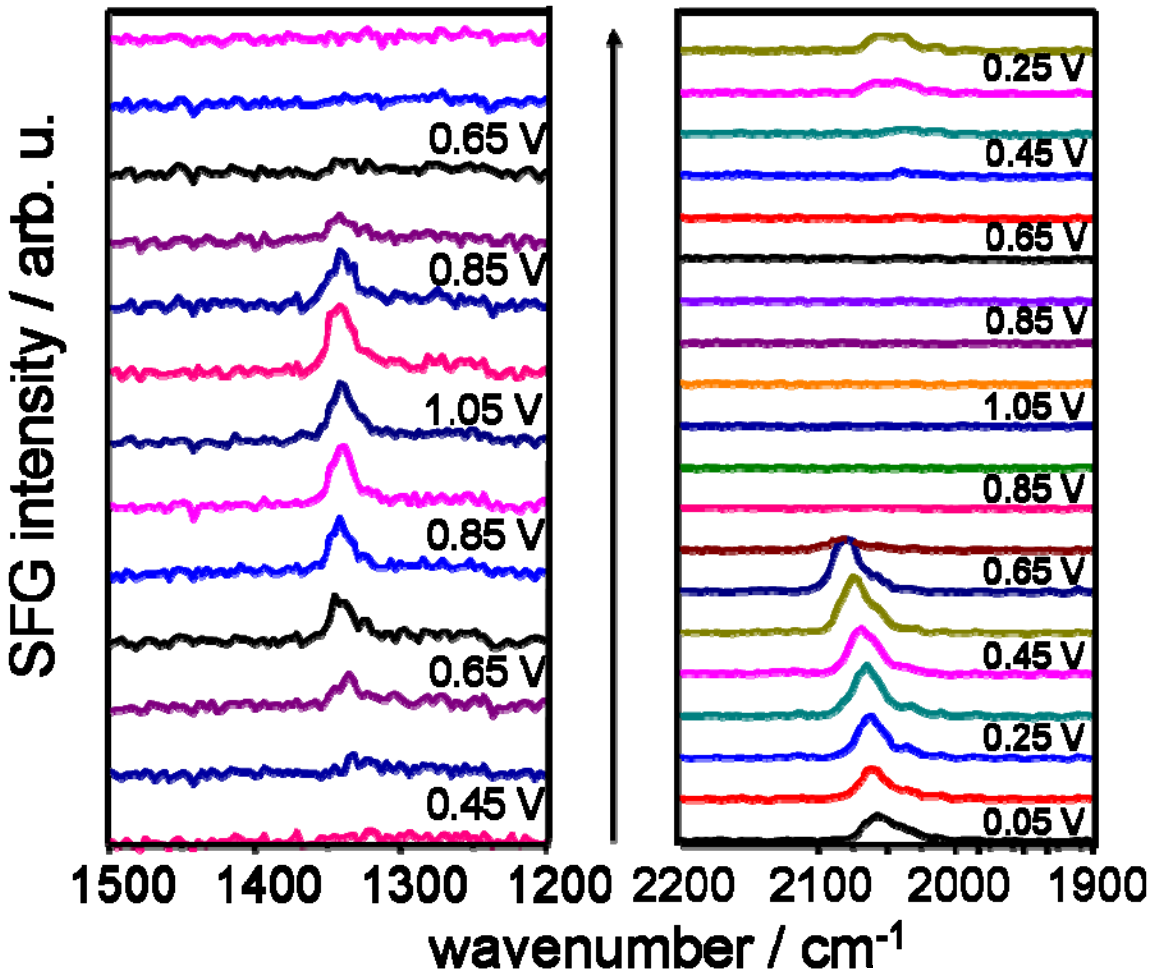

Figure 4.12. Potentiodynamic series of SFG spectra in 0.1 M H_2SO_4 with 0.5 formic acid. The broadband IR pulse was centered at a) 1340 cm^{-1} and b) 2080 cm^{-1} respectively. Potential values are shown with respect to RHE.

CHAPTER 5

STUDIES OF COVERAGE AND pH ON SPECTRAL BEHAVIOR OF CARBON MONOXIDE

5.1 Notes and Acknowledgements

This chapter arises from unpublished work done with both electrochemical and spectroscopic analyses of adsorbed carbon monoxide. Carbon monoxide is the one intermediate poison that unites all the small organic fuels with which this dissertation has dealt so far. Therefore, it may eventually be significantly advantageous for scientists to have a solid theoretical understanding of the molecular-level behavior of carbon monoxide. It was with this notion in mind that these studies were performed, to see how changes in pH, applied voltage and CO coverage on an ordered surface would affect the measurable properties of the adsorbate.

I'd like to acknowledge several people for their assistance with this work, including Drs. Prabuddha Mukherjee, Dana D. Dlott, Alfred Anderson and Andrzej Wieckowski. In particular, Drs. Anderson and Wieckowski were helpful in introducing this study and provoking discussion about the results of this work. Research described in this study was supported by the US Army Research Office under award W911NF-08-10309 as well as from the US Air Force Office of Scientific Research under award: FA9550-09-1-0163.

5.2 Introduction

Carbon monoxide is a well known catalyst-poisoning intermediate of most liquid fuel oxidations.[1-5] Platinum in particular is a catalyst well known for its high activity in such reactions,[6, 7] but is also very easily poisoned by carbon monoxide. Additionally, changes in catalyst morphology, electrolyte pH, applied potential and CO coverage appear to have significant influences on the behavior of surface adsorbed CO.[8-12] It is therefore obviously desirable to acquire a more thorough predictive understanding of how fine adjustments to these parameters may be made in order to limit the extent of CO poisoning and lower the overpotential for CO oxidation.

Such a predictive theoretical knowledge may be possible through modeling of CO adsorption behavior.[13-15] However, any sound theoretical model must accord be in accord with experimental data. For instance, if one were to try to construct a model that predicted changes in CO spectral behavior across a range of electrolyte pHs, then ideally the theory should match actual experimental spectroscopic data in the system being modeled. However, it is clearly better if most experimental parameters are constrained; in this way, one does not operate from the unwarranted assumption that spectral behavior of adsorbed CO is invariant of catalyst morphology or electrolyte composition. Thus, in our collaboration with Dr. Alfred Anderson, who was attempting to understand CO spectral behavior across a wide pH range, I chose to constrain both the catalyst morphology and electrolyte anion. Chapter 2 in particular has already shown that a change in electrolyte anion can change the adsorption behavior of CO, and the behavior

of various adsorbates has been previously shown to change as a function of the arrangement of surface sites.

The (111) crystal face of Pt was chosen in this work; it is a highly-ordered surface recognizable by the tightest possible arrangement of surface atoms. A diagram of this surface arrangement is provided as Figure 5.1. Its uniform and well-defined arrangement of Pt atoms makes it an ideal candidate for such modeling techniques as density functional theory. Some data drawn from studies on a polycrystalline surface are also provided as a means of comparison.

The phosphate buffer system was used for changing pH values without changing the electrolyte anion, as this buffer system can have pH values between approximately 1.6 and 12.7 without going below 0.1 M concentration, thus maintaining sufficient electrolyte conductivity. One disadvantage to the practical use of phosphate electrolytes is that the phosphate anion binds strongly to the Pt surface – more strongly, in fact, than sulfuric acid anions.[16, 17] However, spectral observation of adsorbed CO is not made significantly more difficult.

5.3 Experimental

A polished platinum disk cut to the (111) orientiation and a polished polycrystalline platinum disk (Matek) both with a 6 mm diameters were used as the working electrode in the SFG and electrochemical experiments. The counter electrode was a flame-annealed platinum wire (99.99%) and the reference electrode was a commercial Ag/AgCl (BASi; MF-2052; -0.25 vs. RHE) electrode. However, all potentials

throughout this article are reported with respect to a reversible hydrogen electrode (RHE). Voltammetric experiments were carried out using a Princeton Applied Research (PAR 263A) potentiostat. Solutions were prepared using phosphoric acid (99.99%, Sigma-Aldrich), sodium phosphate monobasic (>99.0%, Sigma-Aldrich), sodium phosphate dibasic (>99.0%, Sigma-Aldrich) and sodium phosphate tribasic (96%, Sigma-Aldrich). All dilutions were performed using ultra-pure water ($\geq$18.2 MΩ, total oxidizable carbon $\leq$ 4ppb) obtained from a Millipore Gradient A10 purification system and all solutions were thoroughly purged with Ar gas (ultra-high purity). Prior to each experiment, the Pt disk was soaked in concentrated sulfuric acid, rinsed with ultrapure water, and electrochemically cleaned by potential cycling between 0 and 1.3 V for >50 cycles at a sweep rate of 200 mV/s. It was then annealed according to the Clavilier method, as follows. The disk was heated in a hydrogen flame to white heat for five minutes, then placed in a sealed argon/hydrogen environment to cool for five minutes. It was then lowered into ultrapure water that had been purged with argon and hydrogen so that a protective drop would form on the surface of the Pt(111) crystal, and it was then transferred to the electrochemical cell.

Our BB-SFG apparatus permits the rapid acquisition of vibrational spectra synchronized with a voltammetric sweep. Tunable broadband infrared (BBIR) pulses were generated in an optical parametric amplifier (Light Conversion; Topas) that was pumped by a femtosecond Ti:Sapphire laser system (Quantronix; Integra C series) at a repetition rate of 1 kHz. The BBIR pulses had typical pulse durations of ~120 fs, typical bandwidths of Δ >150 cm^{-1} and pulse energies of approximately 8 μJ at a frequency Ω of

2083 cm^{-1}. Narrow-band visible pulses with 5 μJ pulse energy and a fixed wavelength of 800 nm were generated by narrowing the fs pulses to a bandwidth of <10 cm^{-1} with a Fabry-Pérot etalon. Narrow-band visible and BBIR pulses were overlapped in time and space at an incident angle of ~60º to the normal of the Pt-electrolyte interface. Sum-frequency photons were collected with a spectrograph and a charge-coupled device (CCD). The SFG, visible, and IR photons were all p-polarized. Spectro-electrochemical experiments were carried out in a previously described electrochemical cell for synchronized SFG and electrochemical experiments. In this electrochemical cell, a well-defined gap of 25 μm between the electrode surface and a CaF_2 optical window is established by a Teflon spacer of the same thickness. The 25 μm electrolyte gap allows for voltammetric scans at sweep rates of ≤ 5 mV/s without the detriment of strong ohmic drop effects that are associated with thin-layer electrochemistry.

CO stripping peaks for full coverage of CO were acquired by immersing the electrode in an electrolyte solution experiencing a steady flow of CO while holding at a potential of 0.1 V for twenty minutes. The electrolyte solution was then purged with Ar gas for an additional twenty minutes while the potential was still held. At this point, the disk was raised into the meniscus configuration, and a 50 mV/s cyclic voltammetric sweep was applied.

For the reduced CO coverage experiments, there was no easily available method in our laboratory of releasing precisely controlled small volumes of CO into solution, so the technique was improvised. Flow rate of CO was kept low enough to permit the observation of single bubbles of CO rising into the electrolyte solution. In both the

electrochemical and spectroscopic experiments, only a single bubble of CO was permitted to glance the Pt(111) surface. Although calculation of CO coverage is possible using this technique in an ordinary electrochemical cell by integrating the area under the CO-stripping curve and using the 420 $\mu C/cm^2$ CO charge constant, this cannot be done in the thin-layer configuration used in the SFG cell, thus precluding such quantitative comparisons.

5.4 Results

Figure 5.2 compares the voltammetric CO-stripping sweeps for the pH 1.6 and pH 4 phosphate solutions. The CO stripping peaks themselves are roughly comparable in intensity and onset (between 0.5 and 0.6 V vs RHE), although the pH 4 CO stripping peak appears slightly more narrow. Additionally, the blank CVs are significantly different. In both CVs, it is worth noting that the hydrogen UPD peaks are obvious and relatively well-defined.

Figure 5.3 compares the voltammetric CO-stripping sweeps for the next highest pH values, 10.1 and 12.7. Here the underlying blank CVs are less well-defined and lack the hydrogen UPD peaks found in the lower two pHs. At pH 10.1, the CO oxidation peak has approximately the same onset potential if not a bit lower, but is broader than at pH 4. By pH 12.7, the onset potential for the CO oxidation peak is closer to 0.3 V, and the peak itself is quite broad. Nevertheless, for all pH values, the CO peak is centered between 0.6 and 0.7 V. Each blank CV appears to lack the kind of broad, well defined oxide formation and reduction peaks seen in CVs of polycrystalline Pt surfaces.

Figures 5.4 and 5.5 show the potentiodynamic series of BB-SFG spectra for these pH values. CO appears to oxidize away from the surface after last being observed between 0.6 and 0.7 V for every pH value. Although CO band intensity varies between pHs (as can be roughly seen by the noise level), this should not be correlated to CO coverage or molecular arrangement; such comparisons are only strictly appropriate when made within the same potentiodynamic series due to changes in beam intensity and alignment from day to day. Additionally, bandwidth values vary between 2-5 cm^{-1} FWHM, which seems insufficient to confidently draw comparisons or inferences.

Figure 5.6 shows a selected range of modeled CO peaks in each phosphate system for the purpose of showing differences in CO vibrational frequency as well as Stark tuning. At the lowest pH value of 1.6, the Stark tuning rate is about 29 cm^{-1}/V and the frequency starts at about 2080 cm^{-1}. The Stark tuning rate has increased modestly to about 41 cm^{-1}/V by the highest pH value, and the vibrational frequency has lowered more significantly to approximately 2048 cm^{-1}.

Table 5.1 tabulates these results as well as some comparative results from non-phosphate electrolyte systems and a polycrystalline Pt disk. The Stark tuning range appears slightly wider in the H_2SO_4 – NaOH electrolyte system on a polycrystalline Pt disk, but not on an ordered Pt(111) surface.

Figure 5.7 shows comparative CO-stripping peaks on a Pt(111) surface in 0.1 M $HClO_4$ at different CO coverages. The difference between oxidation peaks appears more obvious and dramatic in this electroanalytical comparison for different CO coverages than it is for different pH values. At lower CO coverage, the CO oxidation peak has a

single onset is centered approximately 100 mV more negative. By contrast, the higher CO coverage peak seems to have two onsets. One starts at approximately 0.5 V and yields a low current plateau until between 0.6 and 0.7 V, at which point it transforms into a sharp intense peak centered at around 0.7 V.

Figure 5.8 shows a potentiodynamic series of spectra for lower CO coverage on a Pt(111) crystal in 0.1 M $HClO_4$. The CO peak initially appears at the expected frequency of 2080 cm^{-1}, but this frequency shifts more dramatically as a function of applied potential, giving a Stark tuning value closer to 40 cm^{-1}/V.

Figure 5.9 shows CO oxidation on Pt(111) electrode in 0.1 M NaOH, pH ~ 13. The figure is included here simply to verify that the high overpotential for CO oxidation seen in the phosphate buffer system at high pHs is a result of the morphology of the crystal surface, not the electrolyte composition.

5.5 Discussion

The loss of the sharp, well-defined hydrogen UPD region as the pH is increased does not appear to have an obvious effect on CO binding behavior. This is somewhat comparable to the difference between the H UPD regions in perchloric and sulfuric acid electrolytes, where the CO atop spectral behavior is practically the same, but the voltammetric H UPD region is far more well-defined in sulfuric acid.[1]

The center of the CO-stripping peak does appear to become more negative as pH values increase, but very slowly on a Pt(111) surface, such that at pH 12.7, it is still centered close to 0.6 V. This practical invariance of the CO-stripping potential with

increasing pH is further reflected in the SFG spectra, all of which see the CO band disappear by 0.65 or 0.7 V, with some minor error attributable to acquisition time. It is also in sharp contrast to the behavior witnessed on polycrystalline platinum surfaces, where increased in pH caused the overpotential of CO oxidation to drop dramatically, as seen in Chapters 2 and 3. Such a finding supports the hypothesis that CO oxidation occurs largely on defect sites that are far less present on well-ordered Pt(111) surfaces.

It is difficult to account for the significance of the much broader CO-stripping peak at the high 12.7 pH value. It is possible that some small amount of CO is being oxidized at lower overpotentials, but not as strongly as on polycrystalline surfaces, and not enough to fully diminish the CO vibrational band. If so, this would imply that CO coverage may be much lower in more alkaline solutions even on a Pt(111) surface at potentials as low as 0.3-0.4 V.

Experiments on lower-coverage CO adlayers were performed in order to investigate whether the spectral differences in vibrational frequency and Stark tuning rate observed at higher pH values were attributable to lower CO coverages. The invariance in vibrational frequency at 0.0 V between Fig. 5.2a and Fig. 5.8 seem to argue unequivocally that the dominant parameter responsible for the lower vibrational frequencies at higher pHs is not the extent of CO coverage. However, the observed Stark tuning rate for the lower-coverage CO system in Fig. 5.8 is approximately 40 cm^{-1}/V, which is very similar to the Stark tuning rate observed in alkaline systems. Thus we observe that higher pHs appear to have a direct effect on the observed frequency of the CO vibrational band, but an indirect effect on the Stark tuning rate.

5.6 Conclusions

The spectral behavior of adsorbed CO was studied primarily on an ordered Pt(111) surface across a range of pH values and with respect to the extent of CO surface-coverage. Controlling for surface morphology and electrolyte anion permitted more confident inferences to be drawn about the influence of the parameters of pH and adsorbate coverage. It was found that as pH is increased, the observed vibrational frequency at any given applied potential drops dramatically. The Stark tuning rate also increases. There did not appear to be a very strong effect on the overpotential of CO oxidation, despite significant differences in the blank voltammetric profile of the Pt(111) electrode. The breadth and precise position of the CO-stripping voltammetric feature did appear to change slightly, but did not appear to correlate with spectroscopic observations. By studying the effects of a lower level of CO surface coverage in a standard acidic electrolyte, these two effects were further disambiguated. The Stark tuning effect was shown to be possibly entirely attributable to the change in CO coverage, whereas the observed vibrational frequency remained what was previously observed at higher CO coverages in acidic electrolytes.

5.7 References

1. R. B. Kutz, B. Braunschweig, P. Mukherjee, R. L. Behrens, D. D. Dlott and A. Wieckowski, *Journal of Catalysis*, 2010, **278**, 181.
2. M. Heinen, Z. Jusys and R. J. Behm, *J. Phys. Chem. C*, 2010, **114**, 9850.
3. R. B. Kutz, B. Braunschweig, P. Mukherjee, D. D. Dlott and A. Wieckowski, *J. Phys. Chem. Lett.*, 2011, **2**, 2236.
4. J. S. Spendelow and A. Wieckowski, *Physical Chemistry Chemical Physics*, 2007, **9**, 2654.
5. Z. L. Liu and L. Hong, *Journal of Applied Electrochemistry*, 2007, **37**, 505.
6. H. Hitmi, E. M. Belgsir, J. M. Leger, C. Lamy and R. O. Lezna, *Electrochim. Acta*, 1994, **39**, 407.
7. T. Iwasita and E. Pastor, *Electrochim. Acta*, 1994, **39**, 531.
8. S. C. S. Lai, S. E. F. Kleijn, F. T. Z. Öztürk, V. C. van Rees Vellinga, J. Koning, P. Rodriguez and M. T. M. Koper, *Catal. Today*, 2010, **154**, 92.
9. M. T. M. Koper and S. C. S. Lai, *Physical Chemistry Chemical Physics*, 2009, **11**, 10446.
10. M. J. Giz and G. A. Camara, *J. Electroanal. Chem.*, 2009, **625**, 117.
11. G. GarciÌ a, P. RodriÌ guez, V. Rosca and M. T. M. Koper, *Langmuir*, 2009, **25**, 13661.
12. S. C. S. Lai and M. T. M. Koper, *Faraday Discuss.*, 2008, **140**, 399.
13. A. D. Allian, K. Takanabe, K. L. Fujdala, X. Hao, T. J. Truex, J. Cai, C. Buda, M. Neurock and E. Iglesia, *Journal of the American Chemical Society*, **133**, 4498.
14. V. I. Elokhin, A. V. Matveev, E. V. Kovalyov and V. V. Gorodetskii, *Chem. Eng. J.*, 2009, **154**, 94.
15. S. Salomons, R. E. Hayes, M. Votsmeier, A. Drochner, H. Vogel, S. Malmberg and J. Gieshoff, *Applied Catalysis B-Environmental*, 2007, **70**, 305.
16. K. D. Snell and A. G. Keenan, *Electrochim. Acta*, 1982, **27**, 1683.
17. V. S. Bagotzky, Y. B. Vassiliev, J. Weber and J. N. Pirtskhalava, *J. Electroanal. Chem.*, 1970, **27**, 31.

5.8 Figures

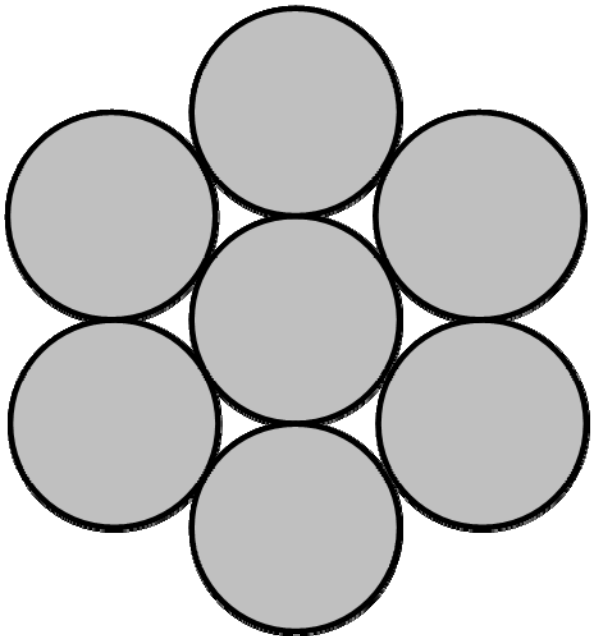

Figure 5.1. A simplified diagram of the arrangement of surface atoms in a Pt(111) electrode. Each circle represents a single atom.

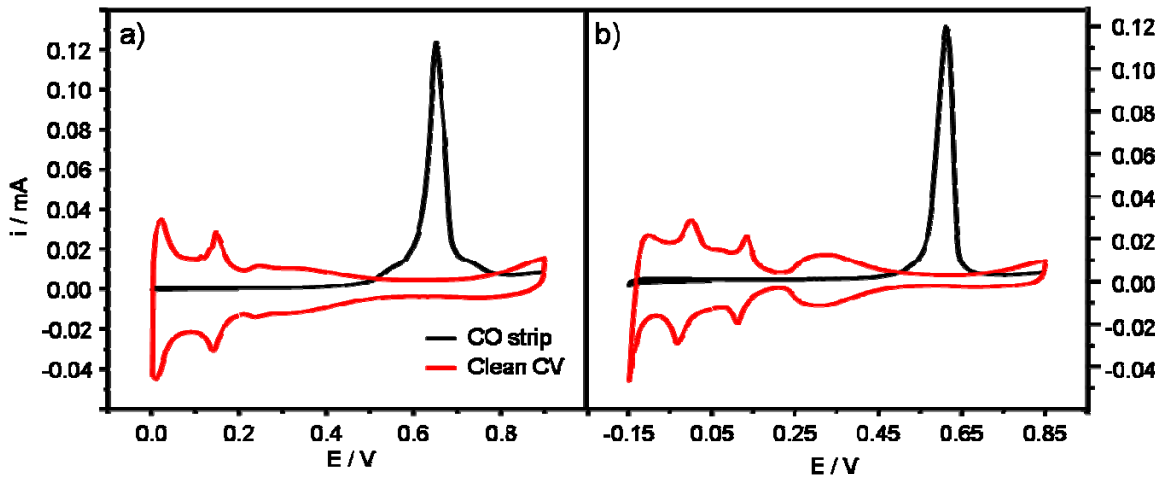

Figure 5.2. Hanging meniscus CO-sweep cyclic voltammograms of a polycrystalline Pt electrode in a) 0.1 M H_3PO_4 and b) 0.1 M NaH_2PO_4. The black line shows the first anodic sweep, and the red curve represents the restored surface after CO has been stripped off. Sweep rates are 50 mV/s for both CVs and potentials are normalized against the RHE.

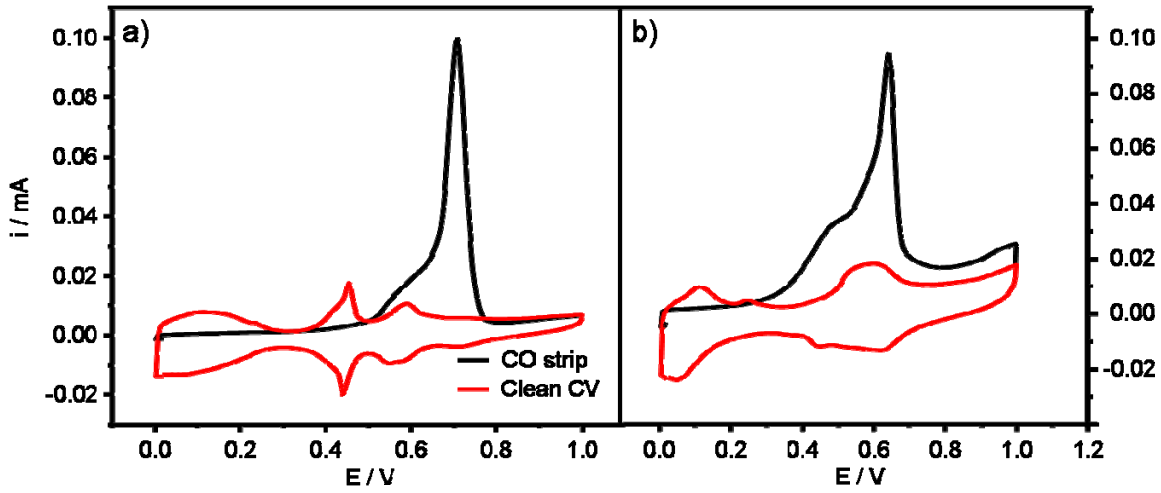

Figure 5.3. Hanging meniscus CO-sweep cyclic voltammograms of a polycrystalline Pt electrode in a) 0.1 M Na_2HPO_4 and b) 0.1 M Na_3PO_4. The black line shows the first anodic sweep, and the red curve represents the restored surface after CO has been stripped off. Sweep rates are 50 mV/s for both CVs and potentials are normalized against the RHE.

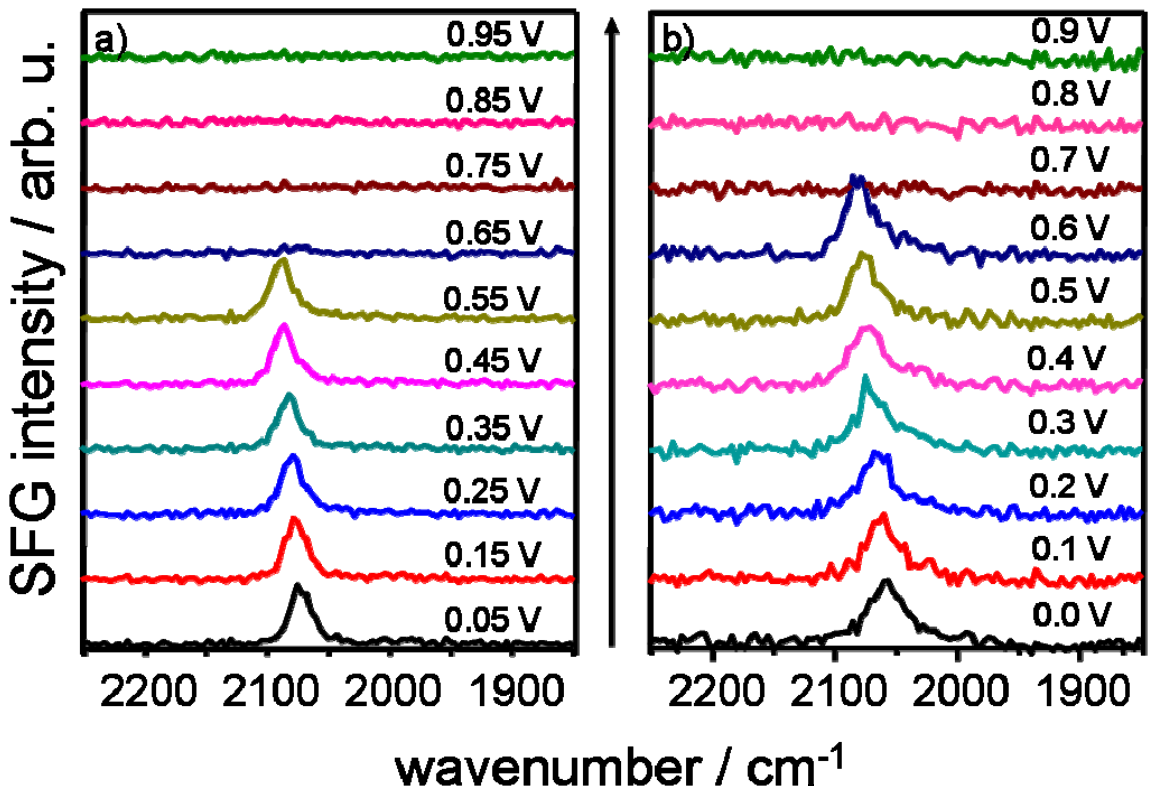

Figure 5.4. Consecutive series of potentiodynamic SFG spectra of atop CO vibrational bands recorded during on a Pt(111) electrode in a) 0.1 M H_3PO_4 and b) 0.1 M NaH_2PO_4. Electrode potentials *E* / V were as indicated in the figure. The frequency Ω of the BBIR pulse was centered at 2080 cm^{-1}. Spectra were acquired for a) 5 and b) 10 seconds.

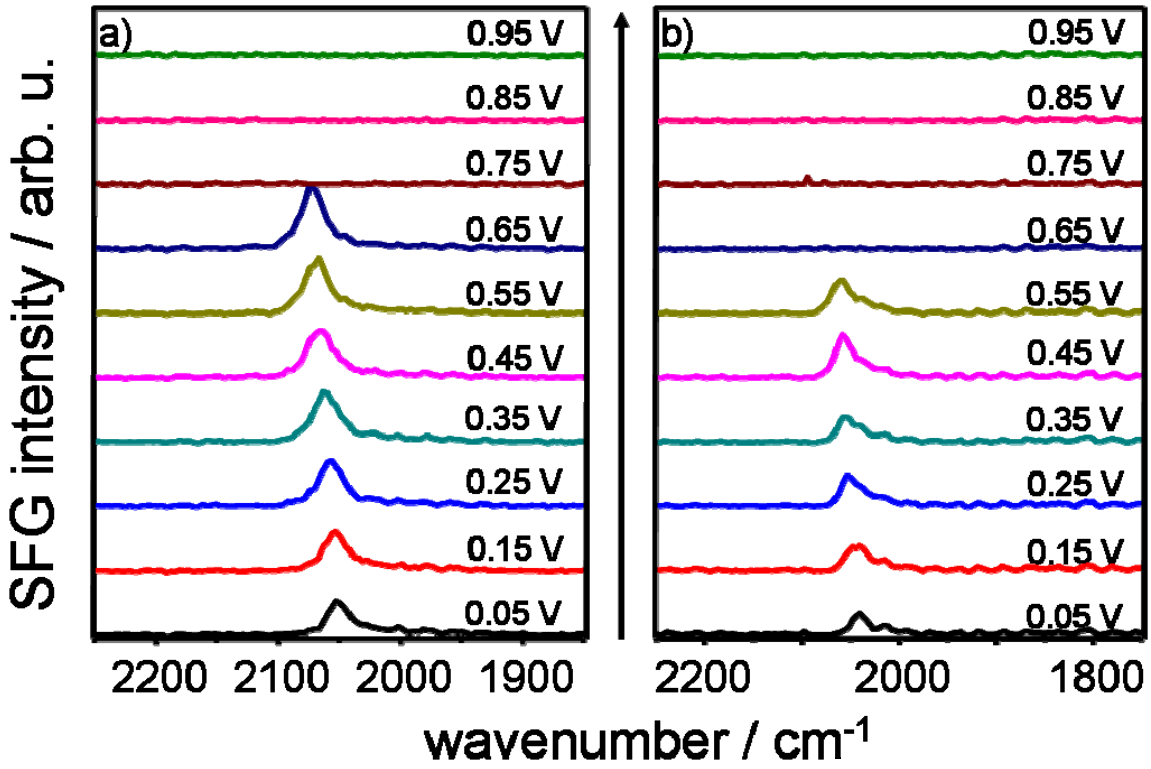

Figure 5.5. Consecutive series of potentiodynamic SFG spectra of atop CO vibrational bands recorded during on a Pt(111) electrode in a) 0.1 M Na_2HPO_4 and b) 0.1 M Na_3PO_4. Electrode potentials *E* / V were as indicated in the figure. The frequency Ω of the BBIR pulse was centered at 2020 cm^{-1}. Spectra were acquired for a) 10 and b) 25 seconds.

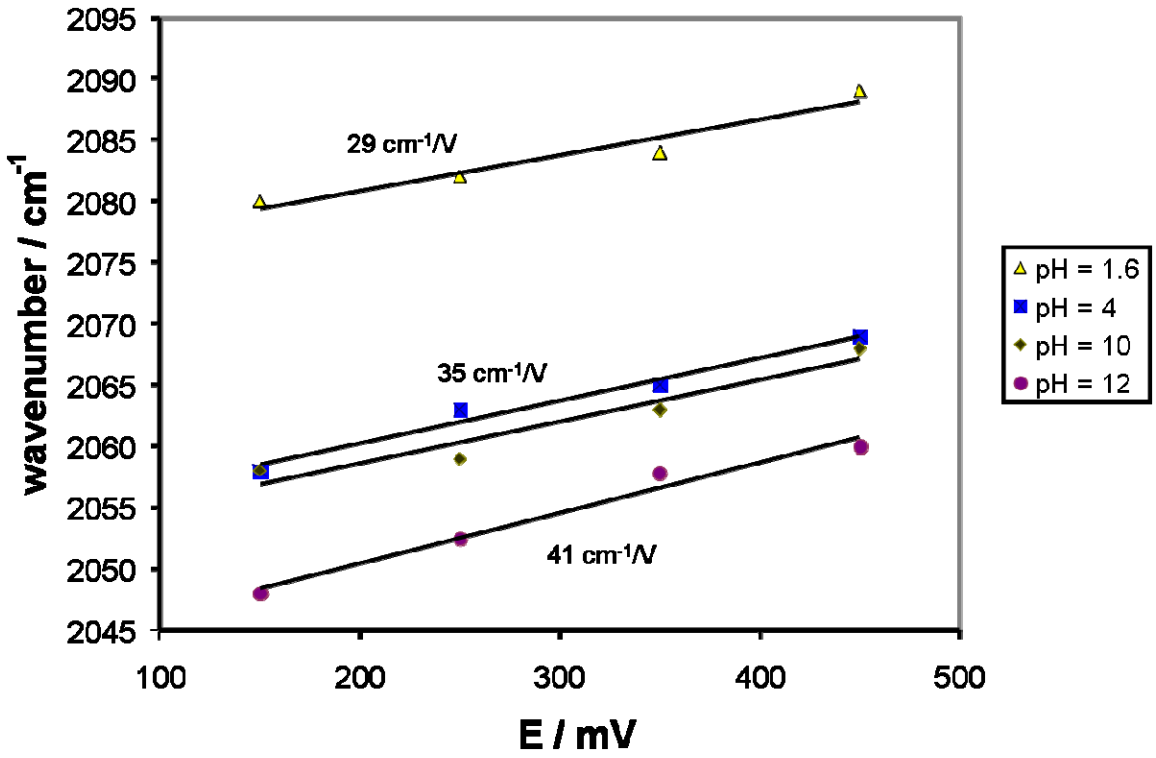

Figure 5.6. Comparison of Stark tuning slopes for CO bound to Pt(111) surfaces in each of the four pH values in the phosphate electrolyte system.

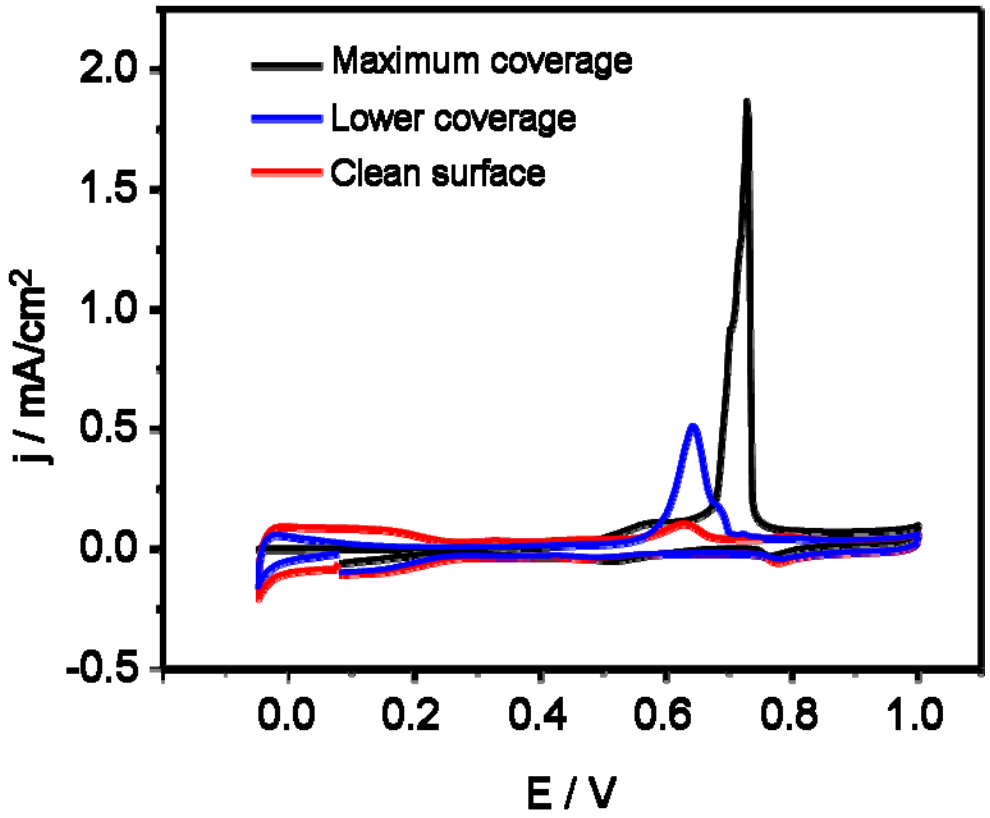

Figure 5.7. Comparative meniscus style cyclic voltammograms of a Pt(111) electrode in a 0.1 M $HClO_4$ solution.

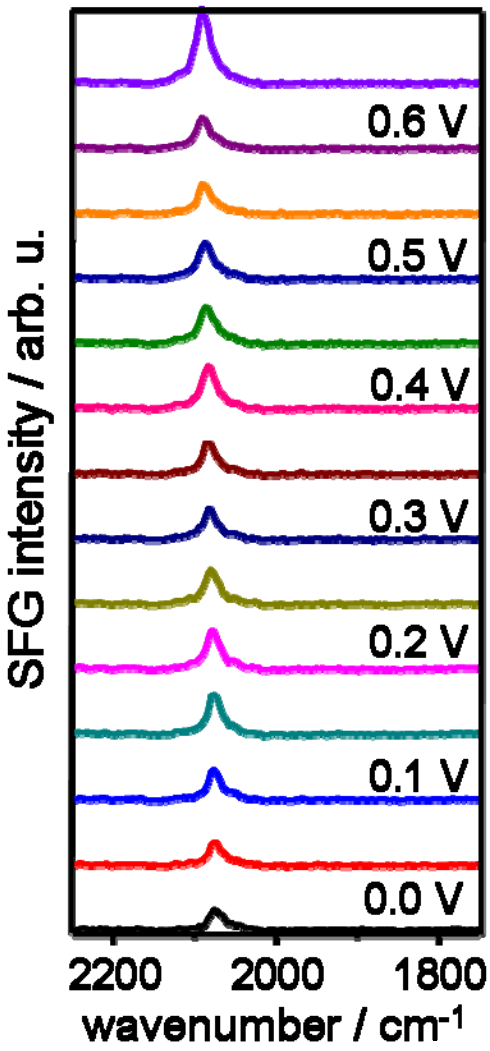

Figure 5.8. Consecutive series of potentiodynamic SFG spectra of atop CO vibrational bands recorded during on a Pt(111) electrode in 0.1 M $HClO_4$ with a very small quantity of CO adsorbed to the surface.. Electrode potentials *E* / V were as indicated in the figure. The frequency Ω of the BBIR pulse was centered at 2080 cm^{-1}.

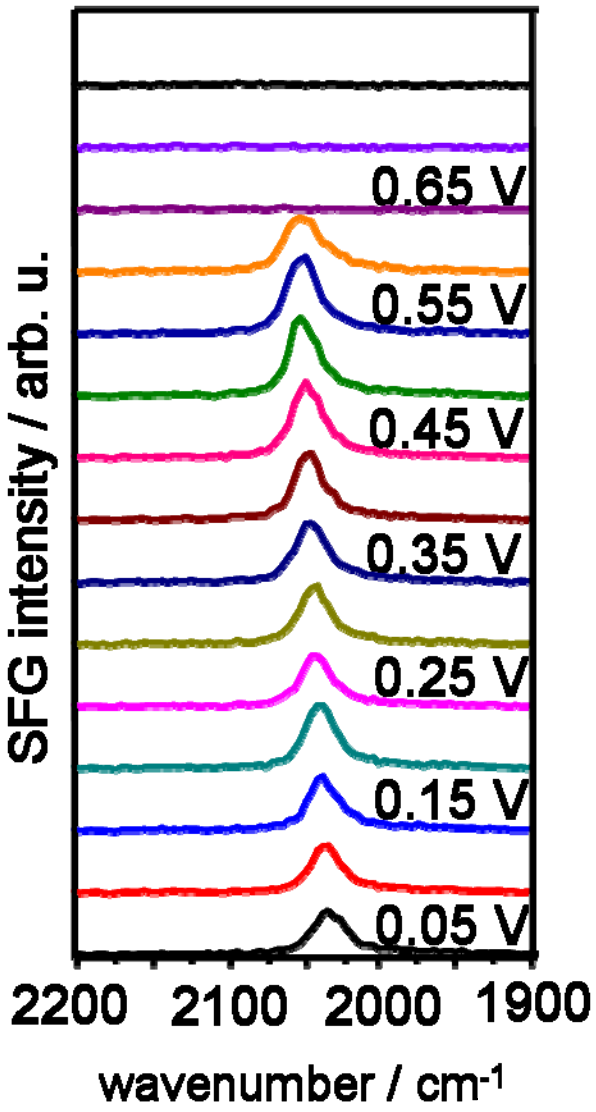

Figure 5.9. Consecutive series of potentiodynamic SFG spectra of atop CO vibrational bands recorded during on a Pt(111) electrode in 0.1 M CO-saturated NaOH. Electrode potentials *E* / V were as indicated in the figure. The frequency Ω of the BBIR pulse was centered at 2030 cm^{-1}.

Pt(111)		Pt(poly)	
Electrolyte	Stark Tuning (cm^{-1}/mV)	Electrolyte	Stark Tuning (cm^{-1}/mV)
H_2SO_4 (pH 1):	25	H_2SO_4 (pH 1):	25
NaOH (pH 13):	36	NaOH (pH 13):	45
H_3PO_4 (pH 1.6):	29		
NaH_2PO_4 (pH 4.1):	35		
Na_2HPO_4 (pH 10.1):	36		
Na_3PO_4 (pH 12.7):	41		

Table 5.1. Calculated Stark tuning rates for the CO adsorbate in each of the indicated electrolytes, divided by catalyst morphology. Electrolytes in every instance were at 0.1 M concentration.

CHAPTER 6

INVESTIGATIONS INTO SPECTROSCOPY OF COBALT OCTAETHYLPORPHYRINS

6.1 Notes and Acknowledgements

This chapter arises from unpublished work done with both electrochemical and spectroscopic analyses of octaethylporphyrins with a cobalt core. This is a departure from the theme of anode-side fuel reactions, and instead deals with novel systems for the oxygen reduction reaction (ORR). The cobalt-porphyrin system had already been identified for its potential usefulness by prior work in our laboratory, and thus there was interest in determining whether spectroscopic characterization of the porphyrin as a function of applied potential could provide insight into its stability and/or mechanism of operation. The results presented here are quite preliminary, but continue to show the capability of SFG spectroscopy to examine a wide variety of systems with unique results.

I'd like to acknowledge several people for their assistance with this work, including Jose Martinez and Drs. Niancai Cheng, Dana D. Dlott, and Andrzej Wieckowski. In particular, Jose Martinez was helpful with his work on the Raman instrument, and he is responsible for the acquisition of Figure 6.2, which is being used here with his permission. Dr. Niancai Cheng offered his prior experience and prepared the porphyrin samples. Research described in this study was supported by the US Army Research Office under award W911NF-08-10309 as well as from the US Air Force Office of Scientific Research under award: FA9550-09-1-0163.

6.2 Introduction

Developing a cheaper but still very effective catalyst for the oxygen reduction reaction (ORR) remains a significant problem in fuel cell development.[1-3] Platinum catalysts are understood to be very active,[4-6] but they are of course very expensive. Conversely, transition-metal N4 macrocycles have received a great deal of attention as potentially effective electrocatalysts for ORR.[7-10] They have yet to achieve the effectiveness of Pt catalysts, but their macrocyclic structure opens the possibility of more strongly correlating their reactivity with the details of their structure.[11]

Prior work in the Wieckowski lab has explored the enhanced catalytic activity of transition metal oxides coupled with octaethylporphyrins (OEP).[12] However, understanding the mechanism of this activity requires the ability to characterize every element of the Co-OEP structure and understand its dependence on parameters such as pH, applied electric potential, and electrolytic environment.

The work on this chapter is preliminary, but attempts to show how BB-SFG spectroscopy can contribute to such in-situ characterization by isolating the vibrational modes corresponding to surface-adsorbed Co-OEP. Early studies were performed using Raman spectroscopy in order to characterize the structure and indicate which vibrational modes seemed most pertinent for focus with SFG. I then moved to both dry and in-situ observations of Co-OEP adsorbed onto an Au electrode.

6.3 Experimental

A polished polycrystalline gold disk (Matek) with 6 mm diameter was used as a working electrodes in the SFG and electrochemical experiments. The counter electrode was a flame-annealed platinum wire (99.99%) and the reference electrode was a commercial Ag/AgCl (BASi; MF-2052; -0.25 vs. RHE) electrode. However, all potentials throughout this article are reported with respect to a reversible hydrogen electrode (RHE). Voltammetric experiments were carried out using a Princeton Applied Research (PAR 263A) potentiostat. Solutions were prepared using $HClO_4$ (double-distilled, GFS Chemicals), Toluene (99.8%, Sigma-Aldrich), and (2,3,7,8,12,13,17,18-Octaethylporphine cobalt (II) (Sigma-Aldrich). All dilutions were performed using ultra-pure water ($\geq$18.2 MΩ, total oxidizable carbon $\leq$ 4ppb) obtained from a Millipore Gradient A10 purification system and all solutions were thoroughly purged with Ar gas (ultra-high purity). Prior to each experiment, the Au disk was rapidly flame-treated in a hydrogen flame, polished sequentially in 0.1 and 0.03 micron alumina suspensions, soaked in concentrated sulfuric acid, rinsed with ultrapure water, and electrochemically cleaned by potential cycling between 0 and 1.6 V for >50 cycles at a sweep rate of 200 mV/s. Co-OEP was deposited onto the Au surface by immersing the electrode in a solution of Co-OEP dissolved in toluene for five minutes, and the electrode was then lightly rinsed and allowed to dry.

Samples for Raman spectroscopy were excited by a Nd:YAG 532 nm laser and spectra were recorded using a Spex Spectrometer. All samples for Raman spectroscopy were dry and exposed to the open air. Conversely, BB-SFG spectra were acquired in 0.1

M $HClO_4$ electrolyte with applied potential control. Our BB-SFG apparatus permits the rapid acquisition of vibrational spectra synchronized with a voltammetric sweep. Tunable broadband infrared (BBIR) pulses were generated in an optical parametric amplifier (Light Conversion; Topas) that was pumped by a femtosecond Ti:Sapphire laser system (Quantronix; Integra C series) at a repetition rate of 1 kHz. The BBIR pulses had typical pulse durations of ~120 fs, typical bandwidths of Δ >150 cm^{-1} and pulse energies of approximately 8 μJ at a frequency Ω of 2083 cm^{-1}. Narrow-band visible pulses with 5 μJ pulse energy and a fixed wavelength of 800 nm were generated by narrowing the fs pulses to a bandwidth of <10 cm^{-1} with a Fabry-Pérot etalon. Narrow-band visible and BBIR pulses were overlapped in time and space at an incident angle of ~60º to the normal of the Pt-electrolyte interface. Sum-frequency photons were collected with a spectrograph and a charge-coupled device (CCD). The SFG, visible, and IR photons were all p-polarized. Spectro-electrochemical experiments were carried out in a previously described electrochemical cell for synchronized SFG and electrochemical experiments. The use of a 25 micron spacer was eschewed for these experiments due to concerns about the attenuation of the IR beam. Instead, potentials were fixed and the system was permitted to equilibrate for 60 seconds prior to each acquisition. Acquisitions were 100 seconds in length.

6.4 Results

Figure 6.1 shows a reference diagram of the relevant chemical bonds in the larger OEP molecule. The transition metal center, Co, is bound by the four N atoms at

the center of the OEP. Figure 6.2 shows the acquired Raman spectrum of the Co-OEP. Particular emphasis is given to the V11 transition at 1577 cm^{-1}, as this band shifts in frequency as the transition metal center is changed.

Two SFG spectra are shown in Fig 6.3. The IR focus is centered at 1370 cm^{-1} in a) and 1562 cm^{-1} in b). These spectra were acquired for 100 seconds in a solution of 0.1 M $HClO_4$. Fig. 3a shows two vibrational bands, one at approximately 1577 cm^{-1} and one at approximately 1544 cm^{-1}. Figure 3b shows this same band at 1544 as well as two bands at 1494 cm^{-1} and 1458 cm^{-1}, attributable to a $C_\alpha C_m$ vibrational mode (previously classified as ν_{38})[13] and a CH_2 scissoring mode of the ethyl subsituent.[13] The transition at 1577cm^{-1} is attributable to a $C_\beta C_\beta$ stretching mode known as the V11 transition.[13] Characterization of the band at 1544 cm^{-1} is troublesome, however. It is very unlikely to be a non-resonant artifact, as it is quite narrow and does not change in shape or frequency as the IR focus is moved. The closest band we find in most Raman spectrum (including our own) is closer to 1520 cm^{-1}, and this is the V3 transition,[13] although prior work by Jarzecki et al. on very simple non-ethyl-substituent metalloporphyrins has found IR and Raman-active bands in this 1544 cm^{-1} region.[14] Additionally, our Raman spectra of Fe-OEP shows a similar unassigned spectral feature in this area.

Figure 6.4 shows the potential dependence of these vibrational bands. Although there is certainly a response in the intensity of each band to applied potential, there does not appear to be any Stark tuning response.

6.5 Discussion

BB-SFG spectroscopy is clearly capable of performing in-situ observations of complex molecules such as the Co-OEP macrocycle. Despite the difficulty of assigning the observed 1544 cm^{-1} vibrational band, the other vibrational bands are well-resolved and pertinent to changes in the electronic structure of the macrocycle itself – particularly the V11 band at 1577 cm^{-1}, which our Raman work has been shown to shift by as many as 10 cm^{-1} depending on the metal center.

Unfortunately, none of these bands appear to have a strong Stark tuning response. There is considerable change in the vibrational band intensities as a function of applied potential (particularly for the V11 band). Further study will be needed to obtain a better understanding of the significance of this effect.

There has been some question of the long term stability of these metal-porphyrin systems in acidic electrolytes, but for at least fundamental vibrational modes such as V11, there appears to have been no change in vibrational frequency moving from open air to $HClO_4$ electrolyte.

It is worth emphasizing that SFG-active vibrational modes must be both IR and Raman-active. BB-SFG spectra will therefore provide a unique selection of vibrational modes from a molecule that is otherwise very complex. However, many of the fundamental vibrational modes of the porphyrin exist in spectral regions that become increasingly difficult for our SFG system to probe. The power of the the IR pulse at 7000 nm is approximately 3 μJ and decreases as the wavelength is increased. Thus, probing lower frequencies attenuates the strength of the IR pulse.

6.6 Conclusion

Characterization of many of the fundamental vibrational modes of metal porphyrins has been previously achieved with Raman spectroscopy. Our Raman spectra of our Co-OEP sample shows its fidelity against literature precedent, and further study with SFG spectroscopy shows that certain vibrational modes can be isolated using this technique. Most significantly, the V11 vibrational mode, which is known to shift in frequency as the metal center is changed, was identified at 1577 cm^{-1}. No significant effect was noticed from the introduction of $HClO_4$. Changing the applied potential did not change the observed frequencies, but did alter the intensities of the bands. Further work with different metal centers and electrolyte systems is likely to yield interesting results, as the ability of BB-SFG to probe this macrocycle in-situ has been demonstrated in this preliminary work.

6.7 References

1. L. C. Wang, L. Zhang and J. J. Zhang, Electrochimica Acta, 56, 5488.
2. I. Roche, E. Chainet, M. Chatenet and J. Vondrak, J. Phys. Chem. C, 2007, 111, 1434.
3. K. P. Gong, F. Du, Z. H. Xia, M. Durstock and L. M. Dai, Science, 2009, 323, 760.
4. T. Toda, H. Igarashi, H. Uchida and M. Watanabe, J. Electrochem. Soc., 1999, 146, 3750.
5. U. A. Paulus, T. J. Schmidt, H. A. Gasteiger and R. J. Behm, Journal of Electroanalytical Chemistry, 2001, 495, 134.
6. S. Mukerjee and S. Srinivasan, Journal of Electroanalytical Chemistry, 1993, 357, 201.
7. U. I. Koslowski, I. Abs-Wurmbach, S. Fiechter and P. Bogdanoff, J. Phys. Chem. C, 2008, 112, 15356.
8. J. M. Ziegelbauer, T. S. Olson, S. Pylypenko, F. Alamgir, C. Jaye, P. Atanassov and S. Mukerjee, J. Phys. Chem. C, 2008, 112, 8839.
9. M. Lefevre and J. P. Dodelet, Electrochimica Acta, 2003, 48, 2749.
10. S. N. S. Z. Goubert-Renaudin, X., J. Electrochem. Soc., 2012, 159, B426.
11. T. G. Spiro and K. Prendergast, J. Am. Chem. Soc., 1991, 114, 3793.
12. S. N. S. Goubert-Renaudin, X. Zhu and A. Wieckowski, Electrochem. Commun., 2010, 12, 1457.
13. X.-Y. Li, R. S. Czernuszewicz, J. R. Kincaid, P. Stein and T. G. Spiro, J. Phys. Chem, 1990, 94, 47.
14. A. A. Jarzecki, P. M. Kozlowski, P. Pulay, B.-H. Ye and X.-Y. Li, Spectrochim. Acta A, 1996, 53, 1195.

6.8 Figures

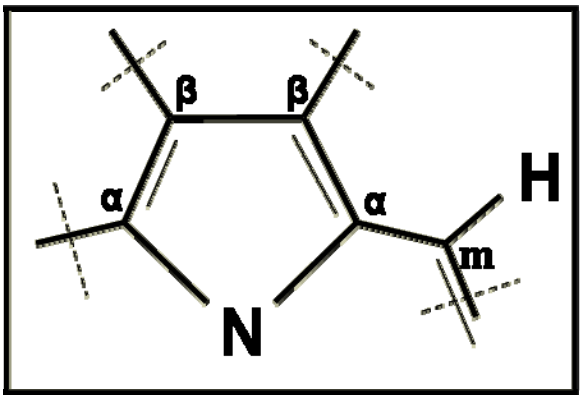

Figure 6.1. Truncated reference diagram of the octaethylporphyrin.

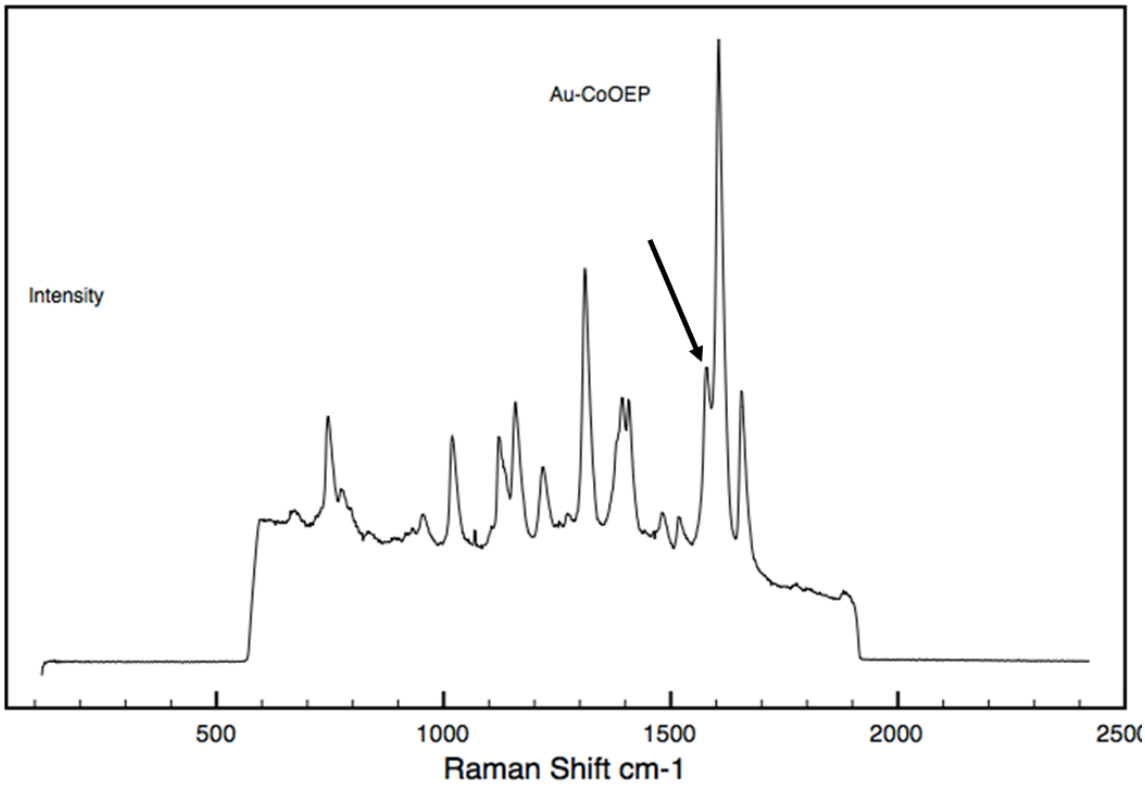

Figure 6.2. Raman spectrum of the Co-OEP adsorbed onto a dry Au surface. The bold black arrow points to the peak at 1577 cm^{-1}, a peak that shifts with changes to the metal center, also observed in SFG spectra.

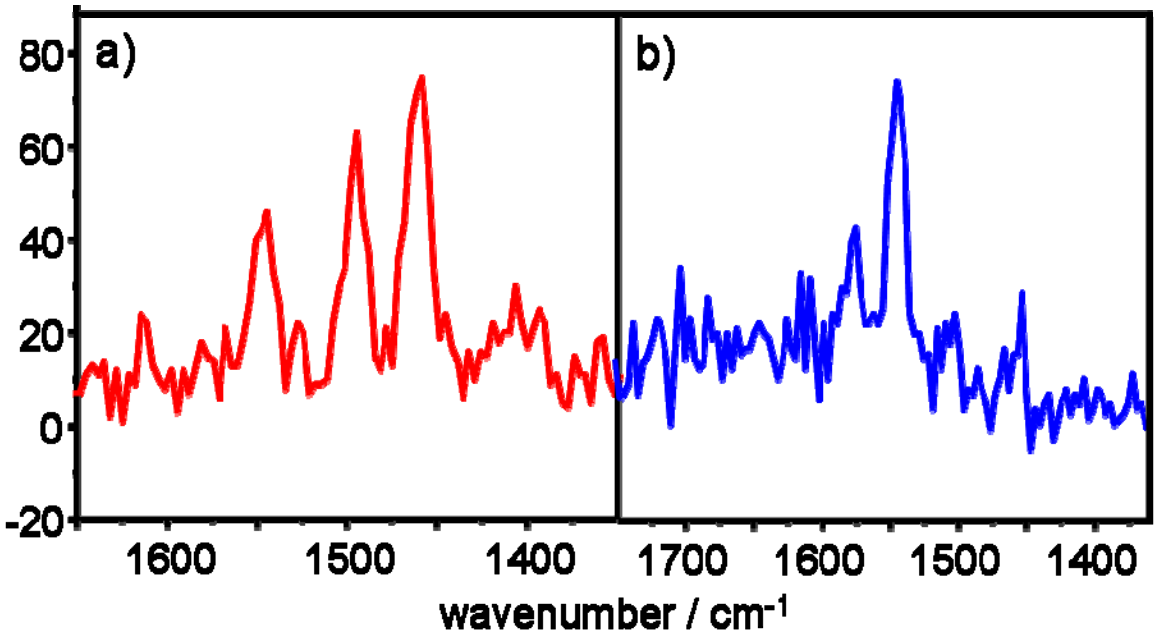

Figure 6.3. SFG spectra of the Co-OEP adsorbed onto an Au electrode in 0.1 M $HClO_4$ with an applied potential of 0.75 V vs RHE. Spectra were acquired for 100s each. The frequency Ω of the BBIR pulse was centered at a) 1370 cm^{-1} and b) 1562 cm^{-1} respectively.

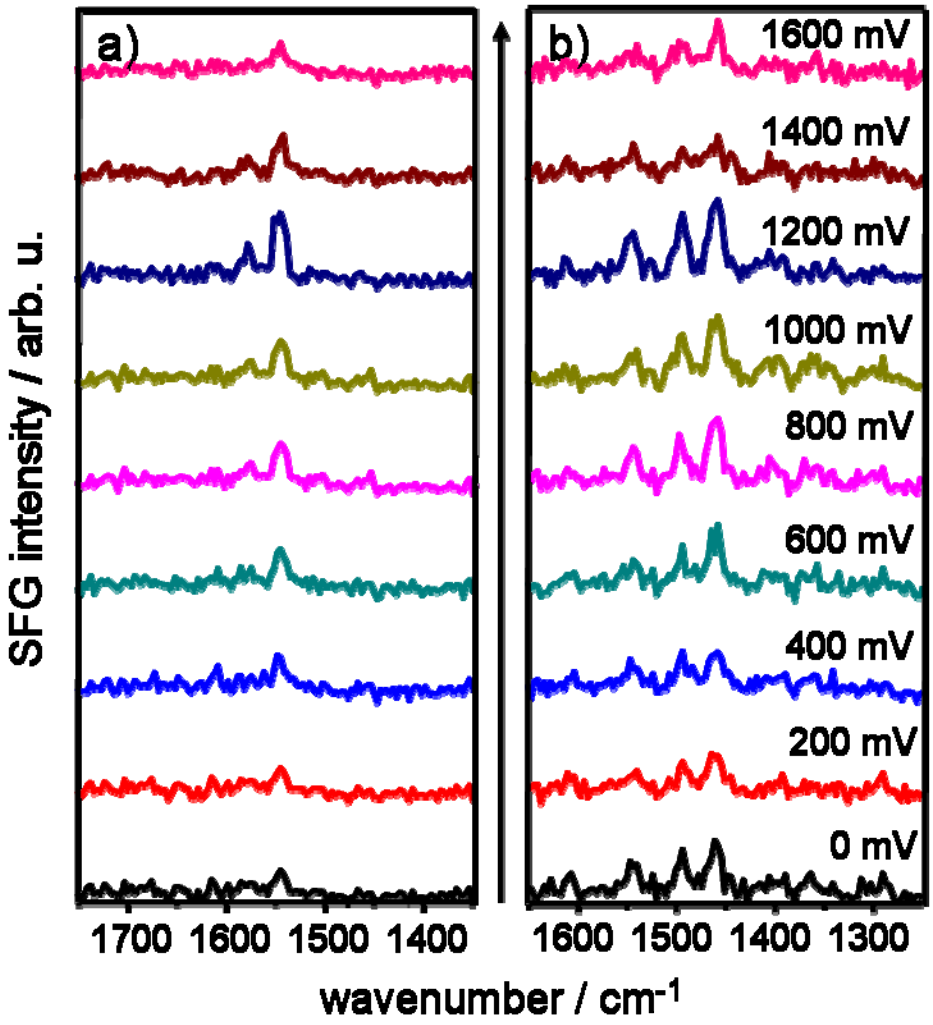

Figure 6.4. Consecutive series of potentiodynamic SFG spectra of the Co-OEP adsorbed onto an Au electrode in 0.1 M $HClO_4$. Electrode potentials *E* / V were as indicated in the figure. The frequency Ω of the BBIR pulse was centered at a) 1562 cm^{-1} and b) 1370 cm^{-1} respectively.

CHAPTER 7

CONCLUSIONS AND FURTHER DIRECTIONS

7.1 Conclusions

The further development of fuel cell catalysis demands a strong fundamental understanding of the surface science involved in fuel cell reactions. Thus, we require a thorough understanding of fuel reaction mechanisms, the behavior of reaction intermediates on the catalyst surface, the effect of the electrolytic environment and its surface-active components, and how the electronic and structural attributes of the catalyst surface affect these reactions. Furthermore, in the case of highly complex catalyst structures such as 4-N macrocycles for the oxygen reduction reaction, we should strive for a more complete understanding of how the catalyst structure is affected in-situ by changes to parameters such as pH, applied electric potential, metal center, and additive such as metal oxides.

Such work is necessarily very exacting and requires the use of techniques that can isolate and provide intense study of specific components of such a complex system. Thus, these studies have not only incorporated the indispensable elements of electrochemical analyses that permit a framework of understanding from which to proceed on each of the reaction mechanisms and catalyst systems studied, but they have made use of the advantages of BB-SFG spectroscopy.

There are several key findings in this work relating both to the capabilities of BB-SFG spectroscopy and to the oxidation mechanisms of small liquid fuels.

In ethanol oxidation in acidic electrolytes, there are a few noteworthy findings. First, the coadsorption behavior of (bi)sulfate and acetate permits acetate to persist on the platinum surface in a wider potential range in sulfuric acid electrolyte. Secondly, the choice of electrolyte anion affects the binding site of the CO intermediate. In perchloric acid, only atop CO was observed, whereas both atop and bridge-bound CO forms were found in sulfuric acid. Third, evidence taken from isotopic analysis of the ethanol molecule shows that there is formation of a single-carbon intermediate that does not easily oxidize into CO. This intermediate, dubbed $–CH_x$, is from the beta carbon of the ethanol molecule.

In ethanol oxidation in alkaline electrolytes, anomalous behavior was observed during the acquisition of SFG spectra showing that CO was forming on the surface at high anodic potentials. Isotopic study of this system revealed that the two potential domains showing CO vibrational bands were due to the formation of CO from each of the different carbon atoms in the ethanol molecule. Again, the beta carbon appears to persist as an intermediate species after cleavage of the carbon-carbon bond and oxidizes to CO at potentials above 0.85 V.

Methanol oxidation in alkaline electrolytes appeared to yield steady-state formation of CO across the entire potential range studied, leading to a potentiodynamic series of SFG spectra in which CO appeared to persist on the surface at every potential. This was more closely examined with fast-scan cyclic voltammetry, a technique with a

much higher time resolution. The result was that at very high anodic potentials, there was no evidence of surface-adsorbed CO.

Further evidence was provided against the notion that acetaldehyde is a long-lived intermediate of ethanol oxidation in alkaline electrolytes by studying its oxidation in 0.1 M NaOH. In addition to providing a potentiodynamic series of spectra in which surface-adsorbed CO persisted up to 0.7 V, a chemical transformation occurred when the potential was momentarily held at values between 0 and 0.5 V that turned the solution yellow. Neither of these phenomena are witness in the oxidation of ethanol in alkaline electrolytes.

The formate radical from formic acid oxidation was observed on a Pt(111) catalyst surface in 0.1 M H_2SO_4, as was CO from the oxidation of formic acid. There appears to be competitive adsorption of each of theses species on the Pt surface, as the vibrational band corresponding to the symmetric O-C-O stretch in formate appears only once CO is being oxidatively removed from the surface at 0.65 V.

Studies of the spectral behavior of CO on a Pt(111) surface for modeling purposes reveal two things. First, increasing pH values cause a modest increase in the Stark tuning response of the CO vibrational band as well as a significant decrease in the observed vibrational frequency at a fixed applied potential. However, it was shown that the first effect is most likely a secondary consequence of the change in pH, as surface-adsorbed CO shows a similar Stark tuning response in acidic electrolytes if there is a lower overall coverage of CO.

Finally, an examination of the use of BB-SFG to characterize cobalt octaethylporphyrin adsorbed to an Au surface show that the technique is capable of observing vibrational bands in-situ. Included is the V11 vibrational mode, which our Raman spectra have shown to change in frequency with changes to the transition metal center. The immersion of the porphyrin complex in acidic electrolyte did not appear to change the frequency of this V11 band, nor did it generate any strong Stark tuning effects.

7.2 Further Directions

The most significant drawback to the BB-SFG technique is the frequently strong non-resonant response. The Dlott laboratory has already noted the possibility implementing a method of eliminating the non-resonant component from detection without the use of a mechanical delay stage to suppress that contribution. If this system, based on advances from the Zanni group,[1-3] were to be implemented, it could significantly increase the possibility of performing more confident SFG studies on complex systems such as the metal-OEP systems and those systems where vibrational bands are simply more difficult to detect, such as is often the case in higher-pH environments or on different surface orientations.

Although the reaction mechanisms for ethanol oxidation have been thoroughly outlined in both acidic and alkaline electrolytes on a polycrystalline Pt surface, further study is required to bring these results forward so that they can be used to design more effective catalysts. Performing these studies on a variety of single crystal faces such as

Pt(111) and Pt(100) may bring into sharper relief the manner in which identified intermediates such as CO and acetate depend on surface morphology for their binding behavior. Such studies as have already been performed on single crystal faces leave certain questions. For instance, Garcia et al. claim the observation of a carbonate species adsorbed to the Pt(111) surface in 0.1 M NaOH simply as a result of the flow of CO into the cell chamber.[4] If carbonate is a poisoning species present on the electrode surface with a strong Stark tuning signal as they claim, then this should be observable with BB-SFG.

The relationship between electrolyte anion behavior of surface adsorbates ought to be better explored. For instance, a (bi)sulfate intermediate is shown to adsorb at high anodic potentials in sulfuric acid electrolytes. However, Chapter 2 also shows that sulfuric acid causes CO to bind more observably to bridge sites on the Pt crystal at much more cathodic potentials, even 0 V. Additionally, the cyclic voltammogram of a blank Pt surface shows relatively sharp hydrogen underpotential deposition peaks that are not present in perchloric acid electrolytes. If BB-SFG shows sulfate adsorbing at high anodic potentials, then why are these effects observed at low potentials, and what role does the electrolyte play in influencing them?

It would be advantageous to be able to directly observe the $–CH_x$ intermediate of ethanol oxidation in alkaline electrolytes. Although Lai et al. have reported observing the species in acidic electrolytes using Raman spectroscopy,[5] they did not observe the same species in alkaline electrolytes. They do, however, infer its existence in the same study from electrochemical analysis. If this molecular species could be observed directly,

then its adsorption and oxidation behavior could be better understood to design catalysts that avoid the persistence of such a poisoning intermediate.

Additionally, future catalysts are unlikely to be composed of platinum if they are to achieve widespread market penetration. Therefore, it is necessary and prudent to examine different electrode materials such as palladium, bimetallic catalysts such as Ru-Pt, and more complex catalyst types, such as the 4-N macrocycle explored in Chapter 6, using BB-SFG spectroscopy. A great deal of work has of course already been done on bimetallic[6-9] and even trimetallic[10-12] catalysts, but these studies do not have the surface-specific advantages demonstrated by the use of BB-SFG in the prior chapters.

Further work should be performed on the OEP system, including changes to the electrolyte as well as the metal center. Additionally, longer-term studies could be performed to see how the OEP does or does not destabilize after some time spent in acidic electrolytes. Being able to probe aspects of the OEP structure in-situ and with applied potential control may prove to be a useful tool for understanding the use of such macrocycles to catalytically enhance the ORR.

7.3 References

1. S.-H. Shim, D. B. Strasfeld, E. C. Fulmer and M. T. Zanni, Adv. Chem. Phys., 2009, 141, 1.
2. S.-H. Shim and M. T. Zanni, Phys. Chem. Chem. Phys., 2009, 11, 748.
3. W. Xiong and M. T. Zanni, Opt. Lett, 2008, 33, 1371.
4. G. Garcia, P. Rodriguez, V. Rosca and M. T. M. Koper, Langmuir, 2009, 25, 13661.
5. S. C. S. Lai, S. E. F. Kleyn, V. Rosca and M. T. M. Koper, J. Phys. Chem. C, 2008, 112, 19080.
6. H. S. Liu, C. J. Song, L. Zhang, J. J. Zhang, H. J. Wang and D. P. Wilkinson, Journal of Power Sources, 2006, 155, 95.
7. Z. L. Liu, X. Y. Ling, X. D. Su and J. Y. Lee, Journal of Physical Chemistry B, 2004, 108, 8234.
8. J. W. Long, R. M. Stroud, K. E. Swider-Lyons and D. R. Rolison, Journal of Physical Chemistry B, 2000, 104, 9772.
9. W. Chrzanowski and A. Wieckowski, Langmuir, 1998, 14, 1967.
10. B. Fang, J. Luo, P. N. Njoki, R. Loukrakpam, D. Mott, B. Wanjala, X. Hu and C. J. Zhong, Electrochemistry Communications, 2009, 11, 1139.
11. F. Gokaliler, B. A. Gocmen and A. E. Aksoylu, International Journal of Hydrogen Energy, 2008, 33, 4358.
12. B. Moreno, J. R. Jurado and E. Chinarro, Catal. Commun., 2009, 11, 123.